larger vortices is found along with the 2P+S structure. In the lower branch, 7 individual weaker (less circulation) and smaller (in core size) vortices are shed with variation from cycle to cycle. In desynchronization, similarly to strong suppression, two symmetric vortices or small eddies are observed eliminating the vortex street and minimizing lift.

(vii) Comparing wake vortex structures at the same U^* and Re but at two different oscillation frequency ratios (f_{osc}/f_s), has shown that the vortex structure around the cylinder is also a function of the oscillation frequency ratio (f_{osc}/f_s).

CHAPTER 4

FIM ENHANCEMENT WITH PTC: GALLOPING

4.1. LITERATURE REVIEW

As discussed in Chapter 3, VIV is a nonlinear resonance phenomenon, where resonance occurs over a wide range of reduced velocity where vortex shedding frequency and body oscillation frequency match due to lock-in. The vibration amplitude is self-limited. In contrast, galloping is an instability phenomenon, where the exciting force from the vortices is not the driving mechanism. Hence, the vibration amplitude is a self-excited vibration and theoretically keeps increasing until system failure. Galloping and VIV look different but they have common features too. According to Parkinson (1989), we have:

(a) "Both occur as transverse vibrations of single long bodies.

(b) Both can occur for any noncircular bluff section with an appreciable afterbody (defined as the part of the section downstream of the separation points).

(c) Both occur in steady incident flow normal to the body span.

(d) Both occur at a frequency close to a natural frequency of the elastic body.

(e) Both are of nearly harmonic waveform in air flow, and typically show little random

amplitude modulation.

(f) Both behave as nonlinear oscillators.

(g) Both result from interaction of the wake with the section afterbody."

The instability phenomenon of galloping can be understood by fluid damping. For a vibrating structure, the main role of damping is energy dissipation and the damping in the structure can be classified as material damping, structural damping, and fluid damping (Sumer & Fredsøe 1997). All three forms of damping limit the vibrations of FIM but material damping, which is created by the internal energy dissipation of materials, is negligible compared to the other two. In practice, every structure has structural damping, which is mainly caused by friction, impacting and rubbing between the parts of a structure. Fluid damping is caused by fluid-structure interaction and the outcome of energy dissipation. When a structure vibrates in an otherwise calm fluid, the relative fluid motion induces on the body an inertia force (added mass) and an additional resistance force - the drag force $0.5\rho DC_D|\dot{y}|\dot{y}$ - from the Morison equation. This additional resistance force generates fluid damping and can affect the total system damping, that is the sum of structural and fluid damping. It is theoretically almost impossible to separate the structural damping from the rest of the damping (Sumer & Fredsøe 1997). Structural damping can be solely found only at idealized situation such as oscillation in vacuum condition. In this case, the total damping is equal to the structural damping. Opposing to the general ideas of damping, or energy dissipation, fluid damping can be the main factor for the system instability and the starting point of galloping can be described by a mass-dashpot-spring model.

For a circular cylinder mounted on linear spring, the equation of motion is

$$m\ddot{y} + 2m\zeta\omega_n \dot{y} + Ky = F_{total}(t) = \frac{1}{2} C_{total} \rho D L U^2 \tag{4.1}$$

This equation is used widely for one directional motion where C_{total} is the transverse force coefficient. However, the big difference between the current study and a smooth cylinder is the presence of sandpaper strips. Galloping has not been observed for a single smooth circular cylinder due to symmetric geometry. For a rough cylinder, the sand paper strips give asymmetry to flow separation and cause an angle of attack. Therefore, the C_{total} term should be split into two terms – Drag and Lift.

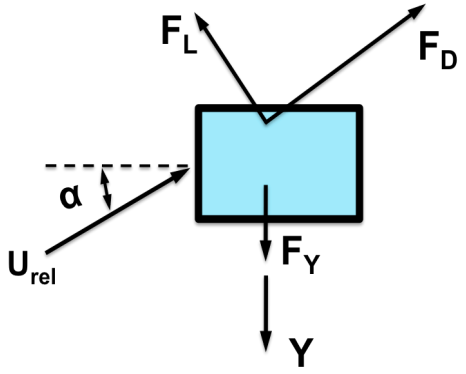

Fig. 4.1. Motion of rectangular cylinder

Because of sufficient height of roughness, the circular cylinder can not be considered smooth any longer and it becomes non-symmetric with respect to the incoming flow – a necessary condition for galloping (Chang 2010). Let's consider the motion of a rectangular cylinder moving downward as in Figure 4.1. F_{total} is the vector resultant of lift and drag in the vertical plane, positive downward,

$$F_{total} = -F_L \cos\alpha - F_D \sin\alpha = \frac{1}{2} C_{total} \rho D U^2 \tag{4.2}$$

where the vertical force coefficient is

$$C_{total} = -\frac{U_{rel}^2}{U^2}(C_L \cos\alpha + C_D \sin\alpha) \tag{4.3}$$

C_{total}, like C_L and C_D, is a function of shape, angle of attack, and Reynolds number.

For small angles of attack α, U_{rel}, and C_{total} can be expanded in power series:

$$C_{total}(\alpha) = C_{total}\big|_{\alpha=0} + \frac{\partial C_{total}}{\partial \alpha}\bigg|_{\alpha=0} \alpha + O(\alpha^2) = -C_L\big|_{\alpha=0} - \left[\frac{\partial C_L}{\partial \alpha} + C_D\right]_{\alpha=0} \alpha + O(\alpha^2) \tag{4.4}$$

where $O(\alpha^2)$ means terms proportional to α^2 and higher powers of α have been neglected.

For small angle of attack, the equation of motion for the spring-supported, damped model responding to the force is

$$m\ddot{y} + 2m\zeta\omega_n \dot{y} + Ky = F_{total}(t) = -\frac{1}{2}\rho D U^2 C_L\big|_{\alpha=0} + \frac{1}{2}\rho D U^2 \frac{\partial C_{total}}{\partial \alpha}\bigg|_{\alpha=0} \left(\frac{\dot{y}}{U}\right) + O(\alpha^2) \tag{4.5}$$

As seen in equation (4.5), transverse force has a velocity correlated force term and when the force is in phase with body velocity, large motion like galloping occurs. In other words, motion-correlated forces can have less effect on structural motion at galloping.

Equation (4.5) can be rewritten as

$$m\ddot{y} + 2m\omega_n\left(\zeta - \frac{\rho U D}{4m\omega_n}\frac{\partial C_{total}}{\partial \alpha}\bigg|_{\alpha=0}\right)\dot{y} + Ky = -\frac{1}{2}\rho D U^2 C_L\big|_{\alpha=0} \tag{4.6}$$

From the sign of damping term, stability of the system can be determined.

For galloping, negative hydrodynamic damping can be induced to the system.

$$\frac{\partial C_{total}}{\partial \alpha}\bigg|_{\alpha=0} > 0 \tag{4.7}$$

For suppression, exactly the opposite condition, positive hydrodynamic damping should be induced to the system.

$$\left.\frac{\partial C_{total}}{\partial \alpha}\right|_{\alpha=0} < 0 \tag{4.8}$$

Flutter can occur for an aerodynamically shaped body such as an airfoil. It is worth noting that even though flutter has a similar mechanism to galloping, it has distinctive features from galloping. Thus, linear aerodynamic theory should be used for flutter contrasted to the galloping instability. The linear aerodynamic theory is based on linear potential flow theory where the body motion is a small perturbation compared to flow velocity. Blevins (1990) stated the difference of flutter and galloping. While galloping is a one-dimensional instability, flutter is usually a two-dimensional instability (torsion and displacement modes). In addition, galloping has relatively small aerodynamic forces and shifts in natural frequency are very small while flutter has large aerodynamic forces with large shifts in the natural frequency.

Further study on mathematical modeling of galloping can be seen by (Corless & Parkinson 1988, and Parkinson 1989).

4.2. RESULTS, OBSERVATIONS, AND DISCUSSION

By studying the amplitude and frequency response of the PTC-cylinder, while changing the location of the roughness strips with respect to the forward stagnation point in small increments, several zones in Chapters 4-5 are identified. A zone is defined as a range of position of the angle (α_{PTC}) of the leading edge of the roughness strip, where similar variation of the PTC-cylinder response from the response of the smooth cylinder is observed. Experiments are repeated for both sandpaper in small increments to establish

the width of each zone. The results are presented collectively in the *PTC-to-FIM Maps* in Fig. 6.1 in Chapter 6.

4.2.1. Hard galloping

The hard galloping phenomenon is only sparingly dealt with in the literature. Hence, the information currently available on this phenomenon is very scarce. In the present experimental study, the existence and occurrence of this hard galloping is demonstrated with numerous tests. Both for smoother (P180) and rougher (P60) strips, this phenomenon is observed when the cylinder is given a threshold initial displacement of approximately one diameter (*1•D*). This threshold amplitude is given to the cylinder by manually pushing the cylinder. For an initial displacement of less than *1•D*, galloping was not initiated. Two hard galloping zones (HG1 and HG2) are observed on either side on the soft galloping (SG) zone (discussed in Section 4.2.2) for both P180 and P60 strips. Occurrence of both HG1 and HG2 is confined to a narrow range of circumferential angle with the range of HG2 being much smaller than the range of HG1. Occurrence of hard galloping has been confirmed over repeated trials of experimentation. Response zones and other oscillatory features are described in the following subsections.

4.2.1.1. Amplitude and frequency response

A. Results for P180 in HG1($2°\leq\alpha_{PTC}\leq14°$) and HG2($56°\leq\alpha_{PTC}\leq58°$)

Fig. 4.2 shows the HG1 ($2°\leq\alpha_{PTC}\leq14°$) and HG2 ($56°\leq\alpha_{PTC}\leq58°$) response for the roughness strip configuration P180 where occurrence of HG2 is limited to a very short circumference range of the cylinder. When the leading edge of the P180 strip is at $\alpha_{PTC}=2°$, the cylinder goes to hard galloping (HG1) at a reduced velocity of $U^*\cong14.8$ attaining an A^* value of about 2.50. When strip placement is further advanced, occurrence of HG1 is shifted to a lower reduced velocity.

For a strip placement angle of 56°, HG2 initiates at $U^*\cong13.0$ and reaches $A^*\cong2.1$ at $U^*\cong15.0$ whereas for strip placement angle 58°, occurrence of HG2 is delayed, and reaches $A^*\cong1.6$ at $U^*\cong15.0$. In both these cases, oscillatory amplitudes are significantly suppressed till HG2 is initiated. The reason for having lower amplitude in VIV and galloping as well as more gradual increase in galloping in HG2 compared to HG1 is that the roughness strip in HG2 covers a small segment of the strong suppression (SS) zone which is introduced in Section 5.2.2. The P180:56°-72° configuration – compared to P180:58°-74° - results in higher amplitude of oscillation in VIV and separation between VIV and galloping by a short range of reduced velocity where amplitude is suppressed. In P180:58°-74°, when roughness strip location is moved downstream in HG2 by two degrees, VIV and galloping are completely separated by a reduced velocity range $12.0\leq U^*\leq13.5$, where the cylinder oscillation is nearly fully suppressed.

For HG1 cases, Fig. 4.3 shows that f^* closely follows the smooth cylinder trend and magnitude till $U^*\cong5.5$ which marks the end of the initial branch. At that point, roughness induces higher f^* than that of the smooth cylinder up to $U^*\cong11.0$. For $U^*>11.0$, f^* decreases slowly. For $13.5<U^*<14.5$, a corresponding f^* is not observed due to low

amplitude of the PTC cylinder. At the onset of hard galloping at $U^*\cong14.4$, a predominant f^* appears in the corresponding spectrum (Fig. 4.6(g)) approximately equal to 1.0, which is consistent with typical galloping characteristics. For HG2, f^* is notably higher than that of the smooth cylinder in the initial and upper branches and declines thereafter. For P180:58°-74°, oscillation frequency undergoes a precipitous drop at $U^*\cong13.7$. For both HG1 and HG2, when galloping is fully developed, f^* approaches 1.0. This feature is similar to that of soft galloping discussed in Section 4.2.2. (Parkinson 1989).

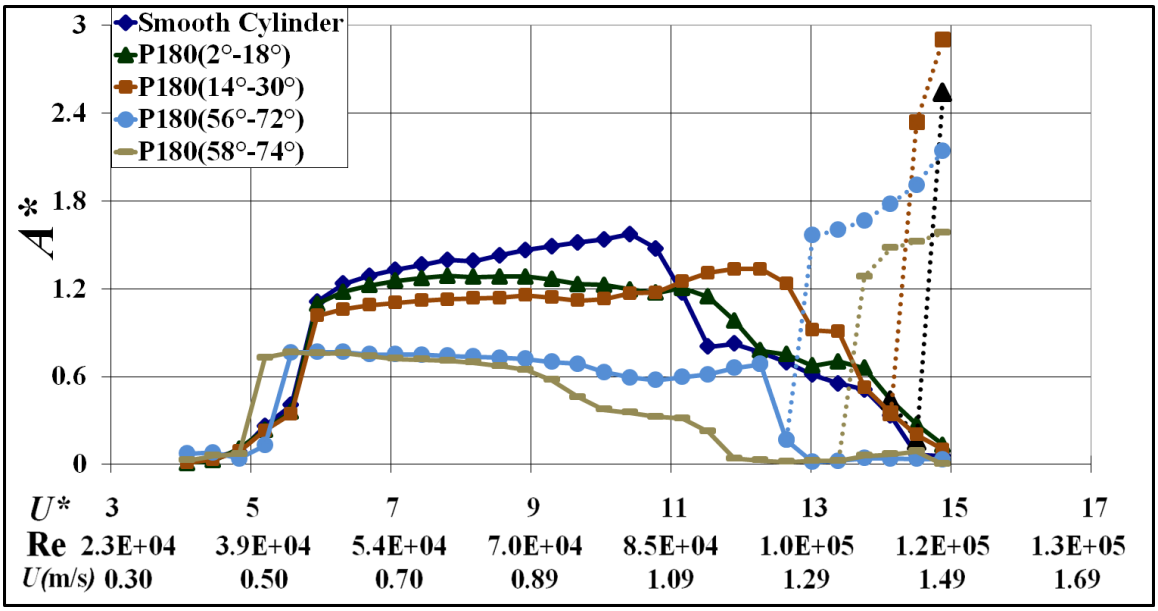

Fig. 4.2. Amplitude response plots for hard galloping (HG1&HG2) with P180; Dotted line denotes cylinder response with hard excitation

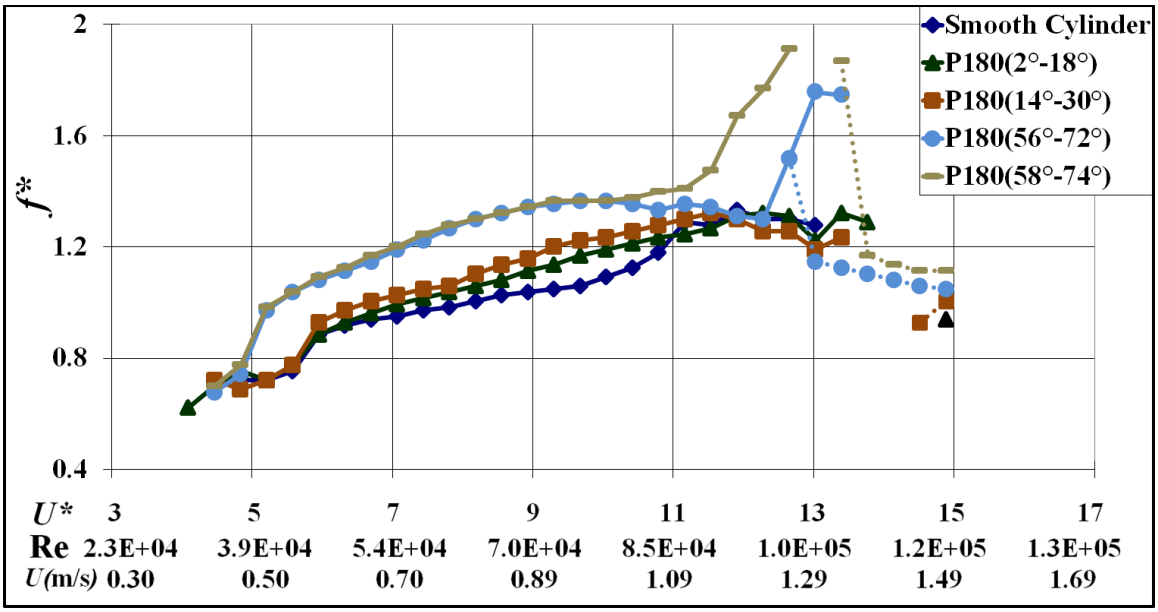

Fig. 4.3. Frequency response plots for hard galloping (HG1&HG2) with P180; Dotted line denotes cylinder response with hard excitation

B. Results for P60 in zones HG1($2°\leq\alpha_{PTC}\leq 8°$) and HG2($60°\leq\alpha_{PTC}<62°$)

Fig. 4.4 shows hard galloping responses ranging from $2°\leq\alpha_{PTC}\leq 8°$(HG1) and $60°\leq\alpha_{PTC}<62°$ (HG2) for P60 strips. With the strip upstream edge at 2°, the cylinder is excited to hard galloping at $U^*\cong 14.5$. When the strip is farther downstream at 8°, similarly to the P180 case in HG1, hard galloping occurs slightly earlier, at $U^*\cong 14.1$. For HG1 for both roughness strips, a sharp decline of oscillation frequency is observed indicating the occurrence of hard galloping (Fig. 4.5).

Similarly to P180, HG2 response zone occurs over a very short range starting at 60° as mentioned earlier. As seen in Fig. 4.4, P60:60°-76° configuration has severely reduced synchronization range with $A^*\cong 0.7$ in the VIV region. Similarly to the case of P180 in HG2, VIV and hard galloping are separated by a reduced velocity range $7.4\leq U^*\leq 10.3$, where the cylinder oscillation is nearly fully suppressed. The PTC-cylinder experiences hard excitation as early as $U^*\cong 10.4$ with upstream tip of the strip at 60° when threshold

amplitude is applied. Without threshold amplitude the cylinder naturally goes to excitation at U^*≅13.3. The hard galloping phenomenon is proof of multiple equilibria of the rough cylinder at the same flow velocity and these multiple equilibria merge at U^*≅13.3. Thus reduced velocities U^*≅10.4 and 13.3 are considered as bifurcation points of hard galloping with much reduced amplitude compared to other hard galloping cases in this study. For P60:60°-76°, low galloping amplitude and low VIV amplitude with reduced synchronization range compared to any other HG in this study are observed. This is due to the fact that the strips cover a segment of the strong suppression (SS) zone (see Section 5.2.2). This conclusion is supported by experiments presented in Section 6.2 on zone robustness by applying reduced width strips. Note that, the maximum amplitude (A^*) of galloping is only about 0.75. By reducing the strip width by 50% and using the same upstream strip location, that is for PTC P60:60°-68°, it is found that the cylinder responds in hard galloping with A^*≅2.2. This is shown with in Section 6.2, Fig. 6.7. For all hard galloping cases with P180 and P60, the closer is the roughness strip to the forward stagnation point (far away from strong suppression zone) the higher is the amplitude in the VIV region.

As shown in Fig. 4.5, for all HG1 and HG2 cases, the frequency ratio drops to about 1.0 at the onset of hard galloping. But oscillation frequency in the HG2 (P60:60°-76°) zone continuously increases until U^*≅15.0. The increase of frequency ratio at high reduced velocities is also observed in most suppression cases in this study. This is also due to the fact of covering segment of the strong suppression zone. This is verified experimentally in Section 6.2.

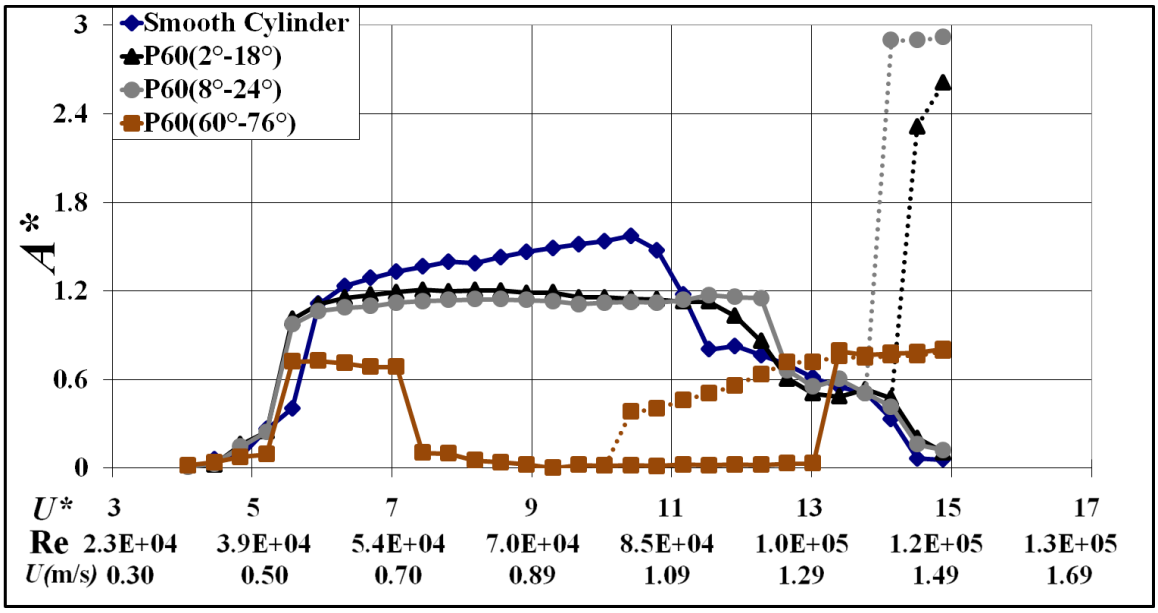

Fig. 4.4. Amplitude response plots for hard galloping (HG1&HG2) with P60; Dotted line denotes cylinder response with hard excitation

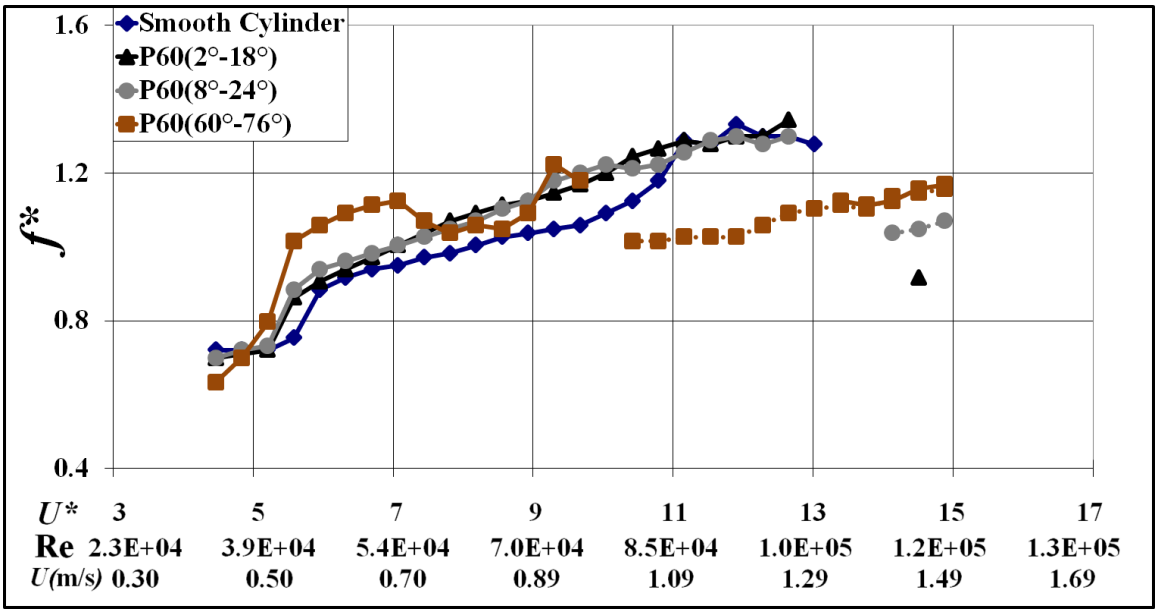

Fig. 4.5. Frequency response plots for hard galloping (HG1&HG2) with P60; Dotted line denotes cylinder response with hard excitation

4.2.1.2. Displacement and power spectrum

4.2.1.2.1. Results in HG1: P60:2°-18°, P180:2°-18°

In HG1, hard galloping response is almost identical through out the zone. So, only two examples are presented for P60:2°-18°, P180:2°-18°. As in the smooth cylinder case at U^*=4.84 which is prior to the VIV synchronization, the PTC-cylinder for P60:2°-18° exhibits quasi-periodic oscillations (Fig. 4.6(a)). The corresponding frequency spectrum shows a major peak at the body oscillation (f_{osc}) and a minor peak at the Strouhal frequency. Steady oscillations are observed at U^*=5.60 (Fig. 4.6(b)) with additional frequency spikes at the 2nd and 3rd harmonics. Steady oscillations are observed in the upper branch (Figs. 4.6(c)-(d)). The frequency spectrum at U^*=8.56 (Fig. 4.6(c)) shows two additional spikes (2nd and 3rd harmonics) whereas, at U^*=10.42, these spikes are not so clear (Fig. 4.6(d)). Figs. 4.6(e)-(f) show the cylinder response with substantially reduced amplitude with more or less a uniformly distributed frequency spectrum in the absence of the threshold amplitude that initiates hard galloping. Once the threshold amplitude is applied, the cylinder goes to hard galloping at U^*=14.51 with steady amplitudes (Fig. 4.6(g)). The spectrum contains the 2nd, 3rd, and 4th harmonics besides the oscillation frequency as seen in Fig. 4.6(g). Similar hard galloping characteristics could be seen for the P180 configuration at U^*=14.89 (Figs. 4.6(h)-(i)). Presence of higher harmonics (1st, 2nd, 3rd, 4th, 5th and 6th) is clearer in this case. The hard galloping characteristics of displacement time histories and spectra for other strip configurations (Figs. 4.2 and 4.4) are nearly the same as those of the typical cases discussed here.

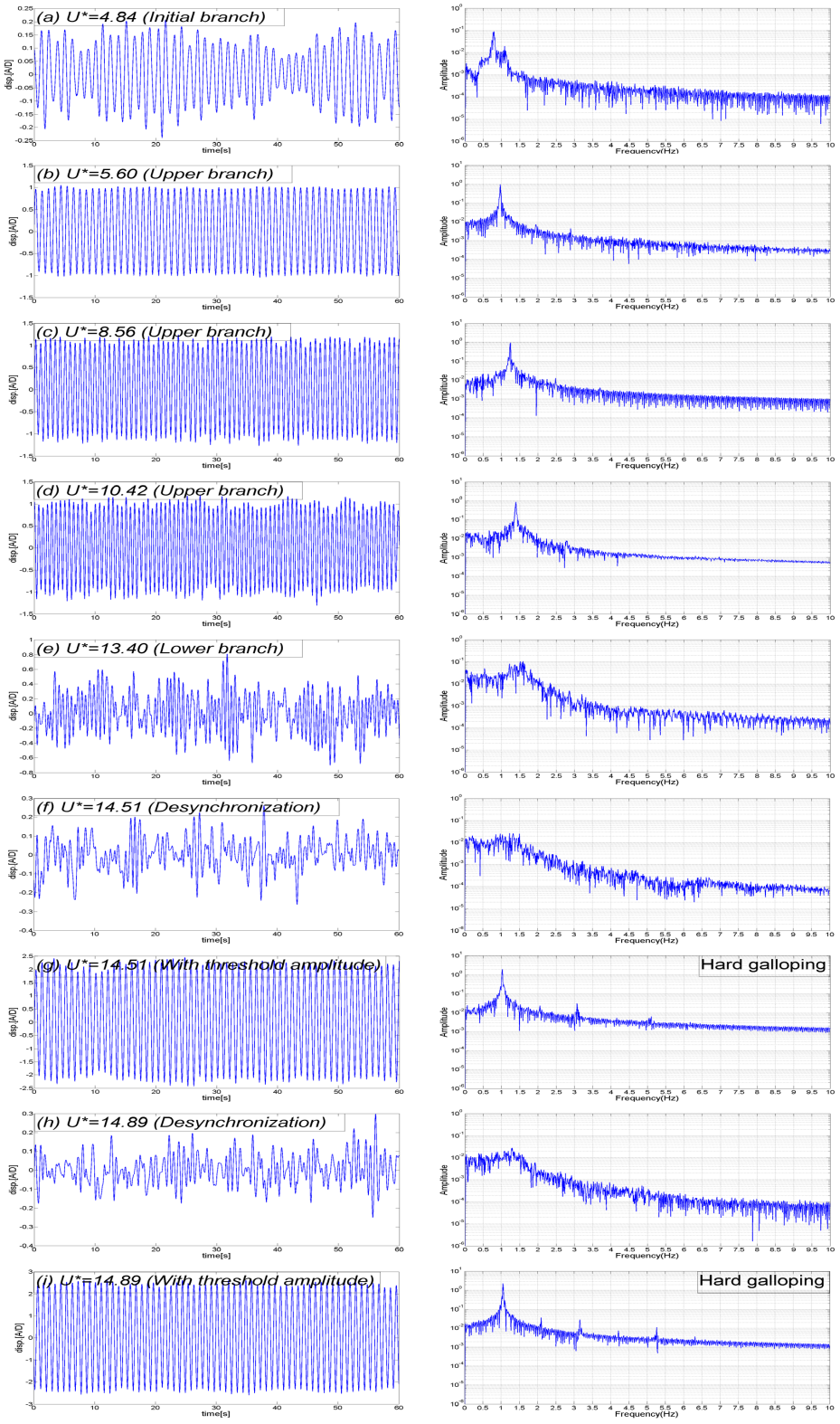

Fig. 4.6. HG1 displacement time histories and spectra: (a)-(g) P60:2°-18°; (h)-(i) P180:2°-18°

4.2.1.2.2. Results in HG2: P180:58°-74°, P60:60°-76°

Response across HG2 is similar so only two examples are presented in this section: P180:58°-74°, P60:60°-76°. The oscillatory features of all cases in HG2 are similar to the cases in HG1 at near-identical reduced velocity values. Typically, Figs. 4.7(a)-(b) show HG2 characteristics for the roughness configuration P180:58°-74° at U^*=14.89. For hard galloping before threshold amplitude is applied, two stable states are observed. One state is that the cylinder is almost stationary. Another state is that the cylinder maintains small amplitude of oscillation. These phenomena are exactly the same as in the cases of hard excitation in VIV (Landl 1975). For the present case, a stationary stable condition usually exists for HG2 (Figs. 4.7(a) and 4.7(c)) and a small amplitude stable state exists for HG1 (Figs. 4.7 (f) and 4.6(h)). Once hard galloping is excited, similar to HG1 cases discussed earlier, multiple frequencies appear in the spectrum consisting of higher harmonics besides the dominant frequency of oscillation (Fig. 4.7(b)). Figs. 4.7(c)-(d) show similar hard galloping characteristics for the P60:60°-76° at U^*=10.79.

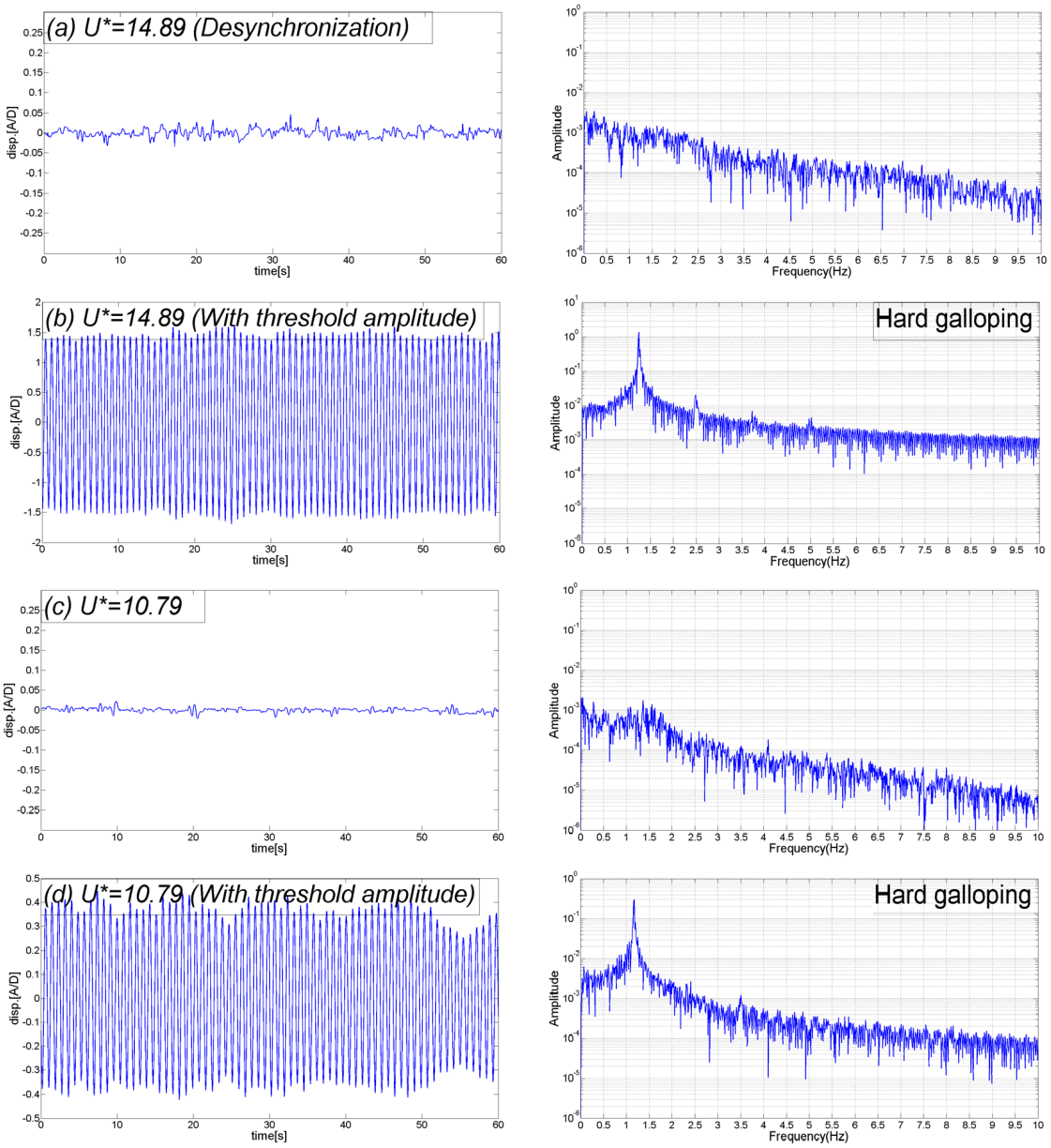

Fig. 4.7. HG2 displacement time histories and spectra: (a)-(b) P180:58°-74°; (c)-(d) P180:60°-76°

4.2.2. Soft galloping

Soft galloping is self-initiated galloping as opposed to the hard galloping phenomenon where a threshold amplitude is required to initiate it. The results for

amplitude and frequency response in the soft galloping zone are discussed in Section 4.2.2.1. In Section 4.2.2.2, a few displacement time histories and the corresponding power spectra of the soft galloping zone are presented.

4.2.2.1. Amplitude and frequency response

A. Results for P180 in SG ($16° \leq \alpha_{PTC} \leq 54°$)

Soft galloping of cylinder with roughness strip P180 is shown in Fig. 4.8. The zone range is 16° to 54°. The following observations can be made: Fig. 4.8 shows three major regions for the PTC cylinder response: VIV, transition from VIV to galloping, and galloping.

In the VIV region only the initial and upper branches exist since transition to galloping occurs right before the lower branch. The onset of oscillations (initial VIV branch) occurs earlier than in the case of the smooth cylinder. Also, all PTC cylinders jump to the upper branch earlier when compared to the smooth cylinder case. Hover et al. (2001) applied tripping wire on an oscillating circular cylinder and they also found that amplitude and frequency lock-in of the cylinder with tripping wire shifts to earlier reduced velocity. The closer the strip is to the front stagnation point (far away from the SS zone), the lesser is the degree of suppression in the initial and upper branches. Amplitudes in the initial and upper branches are partially suppressed compared to smooth cylinder till transition to galloping where amplitude increases abruptly.

The higher the strip placement angle α_{PTC} (i.e., upstream edge of the strip is farther away from the front stagnation point) is, the earlier (lower reduced velocities) the onset

of galloping occurs up to 30°. For the cases with strip angle location starting at less than α_{PTC}<40°, maximum amplitude values with A^*>2.7 are observed whereas for strip angle $\alpha_{PTC}\geq$40°, peak amplitude drops to lower values at the same U^*, as Fig. 4.8 shows. In addition, the higher the strip placement angle is past $\alpha_{PTC}\geq$40° the less is the amplitude in VIV and galloping at the same U^*. This is due to the fact that the roughness strip is closer to or covers part of the strong suppression zone. However, the possible galloping trends beyond $U^*\cong$15.0 are not studied in this paper since that range exceeds the capabilities of the LTFSW channel.

In the initial and upper branches up to $U^*\cong$11.0, oscillation frequency is higher than that of the smooth cylinder and thereafter frequency reduces indicating transition from VIV to galloping (Fig. 4.9). This frequency decline occurs prior to the steep jump of galloping amplitude. The starting point of transition from VIV to galloping for the PTC cylinder is the same as the starting point of the lower branch in the smooth cylinder. Thus, the lower branch of the smooth cylinder is replaced by the transition region from VIV to galloping in the PTC cylinder case. In addition, the farther the strip is from the front stagnation point, the lower is the amplitude of oscillation and the higher is the oscillation frequency, compared to the smooth cylinder, in the initial and upper branches of PTC cylinder in SG. As mentioned earlier, frequency declines for U^*>12.0 during galloping irrespective of the roughness value. One major effect of roughness is the extension of the upper branch with a reduction in the oscillation amplitude (compared to the smooth cylinder). But, as stated earlier, roughness promotes galloping at higher reduced velocities.

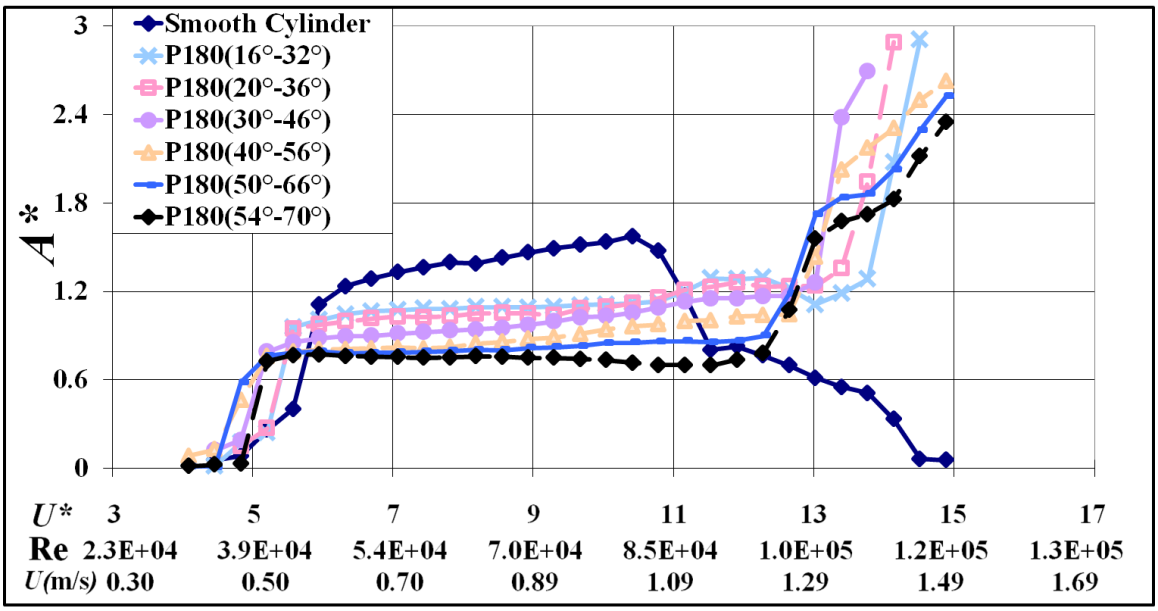

Fig. 4.8. Amplitude response during soft galloping with P180 roughness strip

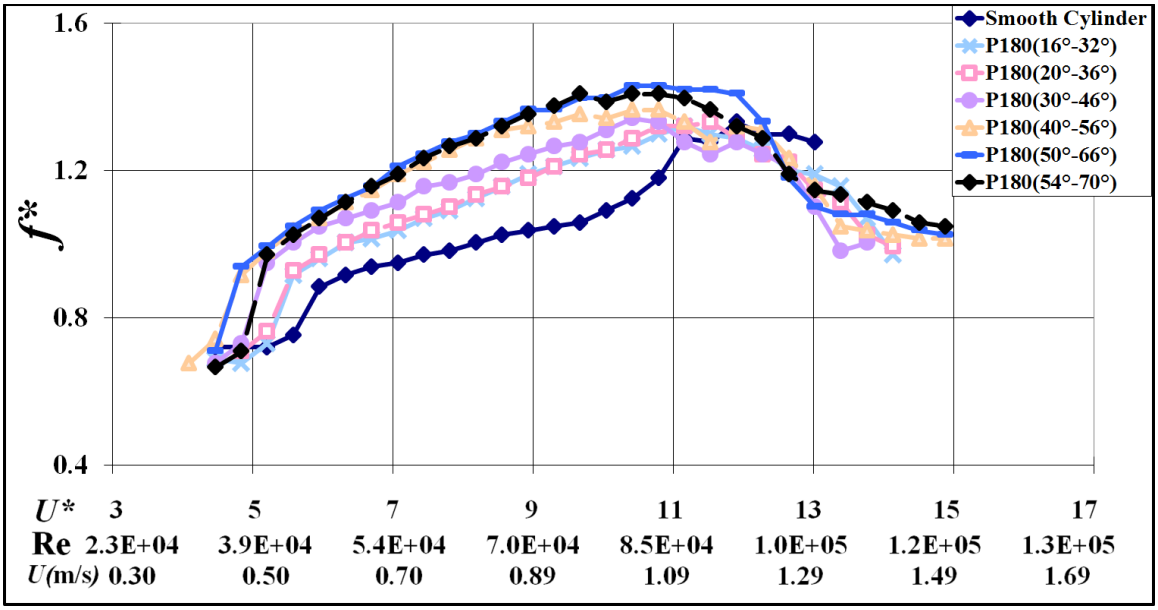

Fig. 4.9. Frequency response during soft galloping with P180 roughness strip

B. Results for P60 in SG ($10° \leq \alpha_{PTC} \leq 58°$)

Soft galloping response of the cylinder is observed over a broad range of strip placement angle of upstream edge (α_{PTC}) from 10° to 58° for P60 strip configurations. Fig. 4.10 shows the soft galloping response trends of the rough cylinder. For strip placement angle α_{PTC} =10°, galloping is initiated at U^*≅14.1 with a very steep increase in amplitude. For larger strip placement angles α_{PTC}<40°, the larger the angle is the earlier the initiation of galloping (at lower reduced velocities) occurs.

However, for a still larger strip angle with placement starting at α_{PTC}=40°, the larger the roughness location is angle (closer to the SS), the later the initiation of galloping occurs, and the less is the amplitude in the VIV and galloping regions. Even, surprisingly, when the strip placement is further advanced to α_{PTC}=58°, galloping is substantially delayed to occur at U^*≅15.6, also with a significantly lower maximum amplitude (A^*≅0.75). This is caused by the fact that the strip is partially lying in the strong suppression zone. As in the hard galloping cases, in all these soft galloping cases, amplitude is partially suppressed in the VIV region. For all soft galloping cases in P60, same as with P180, the closer the roughness strip is placed to the forward stagnation point (far away from the SS zone) the higher is the VIV amplitude.

For all the soft galloping cases, oscillation frequency starts to decline before the commencement of abrupt rise of galloping amplitude as Fig. 4.11 shows. For example, for the P60:30°-46° case, amplitude sharply increases at U^*≅13.0, but the frequency starts to decline at U^*≅11.0. Further, in all soft galloping cases considered here, the oscillation frequency of the PTC cylinder is higher than that of the smooth cylinder before the transition from VIV to galloping (up to U^*≅11.0).

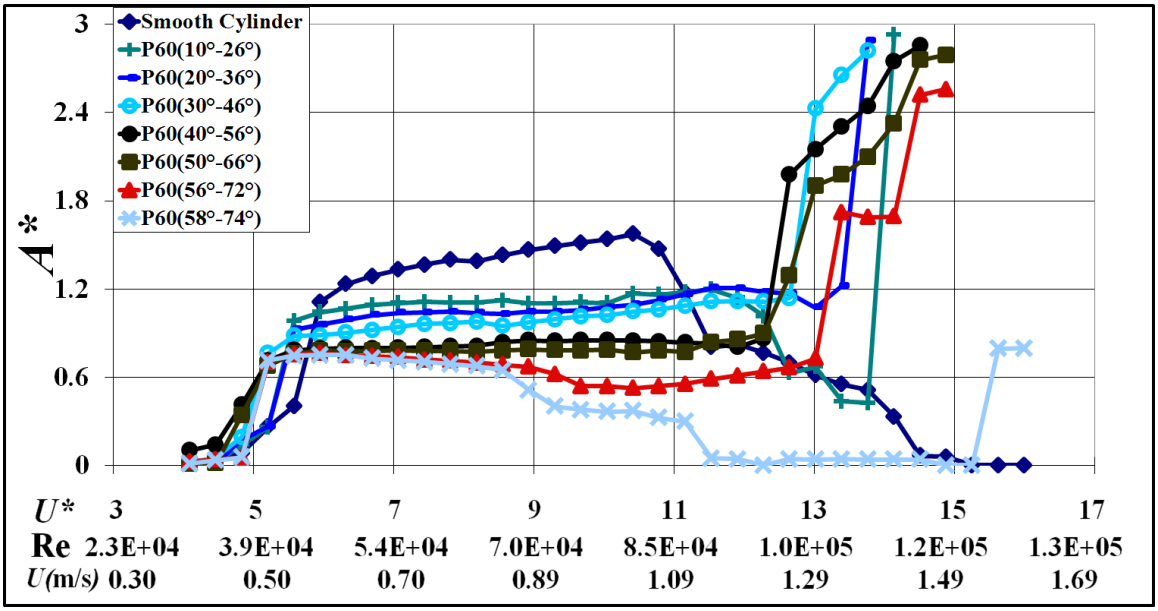

Fig. 4.10. Amplitude response during soft galloping with P60 roughness strip

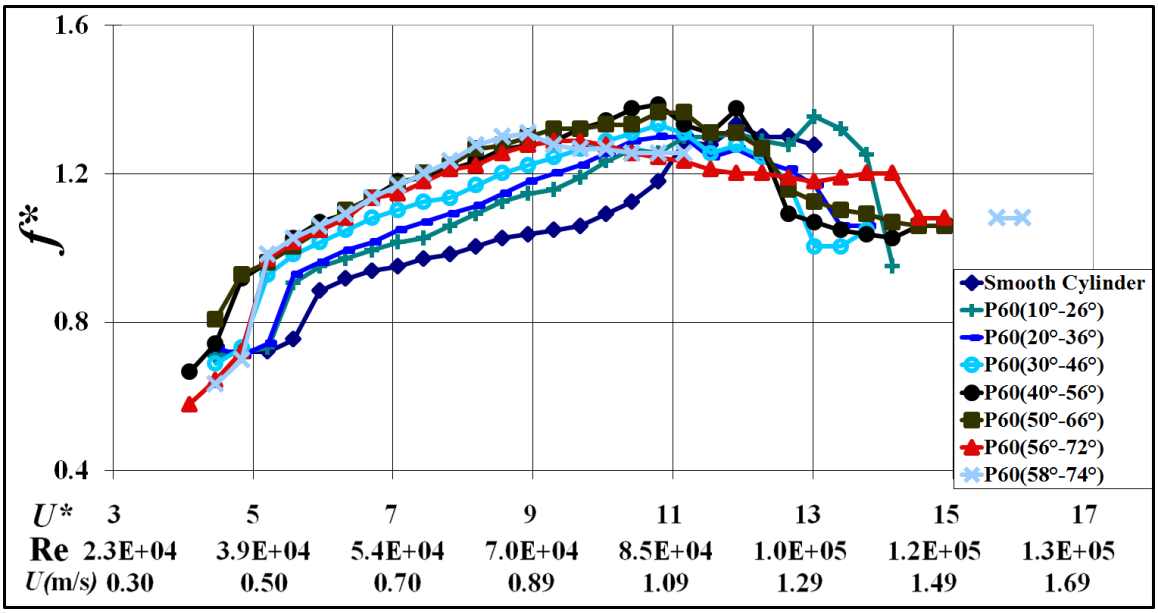

Fig. 4.11. Frequency response during soft galloping with P60 roughness strip

4.2.2.2. Displacement time histories and spectra SG (P180:20°-36°, P60:20°-36°)

Two examples are shown in the SG zone: P180:20°-36°, P60:20°-36°. For P180:20°-36°, at the onset of oscillations (U^*=4.84), the general oscillatory trends for soft galloping (Fig. 4.12(a)) are similar to those for hard galloping (Fig. 4.6(a)). At U^*=5.60 (Fig. 4.12(b)), oscillations in the upper branch are more steady (smaller modulations) than oscillations in the initial branch (Fig. 4.12(a)). As U^* increases more in the upper branch, oscillations remain steady but with bigger modulations (similar to HG1 case, Fig. 4.6(c)) as shown in Figs. 4.12(c)-(d). Additional spikes are observed (indicating 2nd and 3rd harmonics) particularly at U^*=10.42 (Fig. 4.12(d)), whereas, for the corresponding case of HG1 (Fig. 4.6(d)), the 3rd higher harmonic is not significant. Fig. 4.12(e) shows transition from VIV to galloping for P180:20°-36° (U^*=12.65) and response is less steady than in the upper branch and exhibits modulation. At galloping (Fig. 4.12(f)), the cylinder motion is very steady and multiple harmonics are observed in the spectrum. For P60:20°-36°, as shown in Fig. 4.12(g), amplitude modulation is severe at transition from VIV to galloping. But as U^* increased and reached galloping, this modulation disappears and steady motion appears (Fig. 4.12(h)).

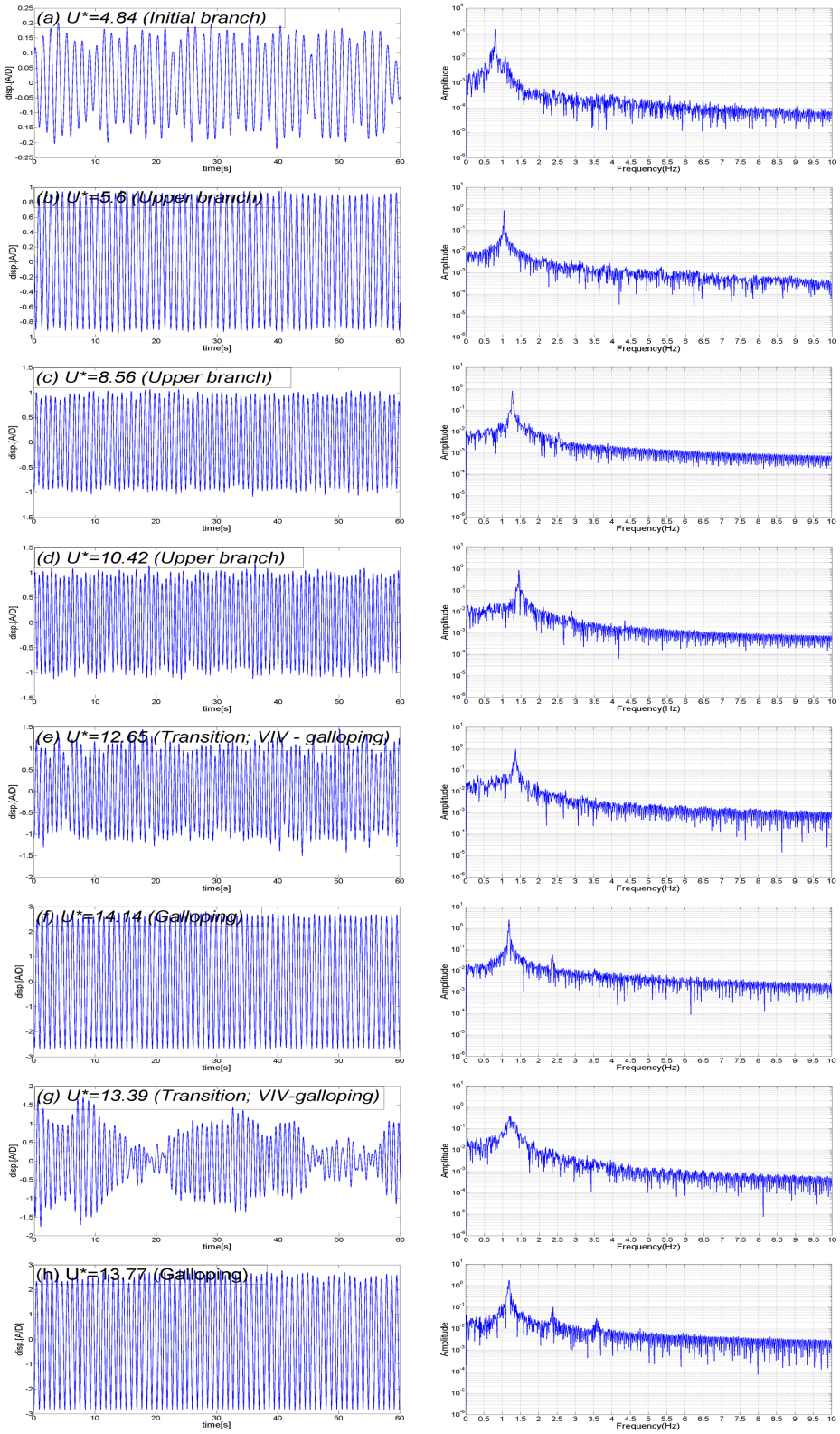

Fig. 4.12 Displacement time series and spectra for SG; (a)-(f) (P180:20°-36°) and (g)-(h) (P60:20°-36°)

At transition from VIV to galloping, as shown in Fig. 4.13, for P180: 16°-32°, galloping and suppression interact together at U^*=13.77. High amplitude of $A^* \cong 2$ region is followed by low amplitude $A^* \cong 0.3$ of region. This region can be considered as the intermediate zone described in Fig. 4.14 between galloping and VIV (Parkinson 1990). The reason for intermittent suppression may be the observation reported by Nakamura & Hirata (1994) that regular vortex shedding is suppressing galloping rather than increasing galloping. This interaction is only found in very limited roughness coverage and reduced velocity.

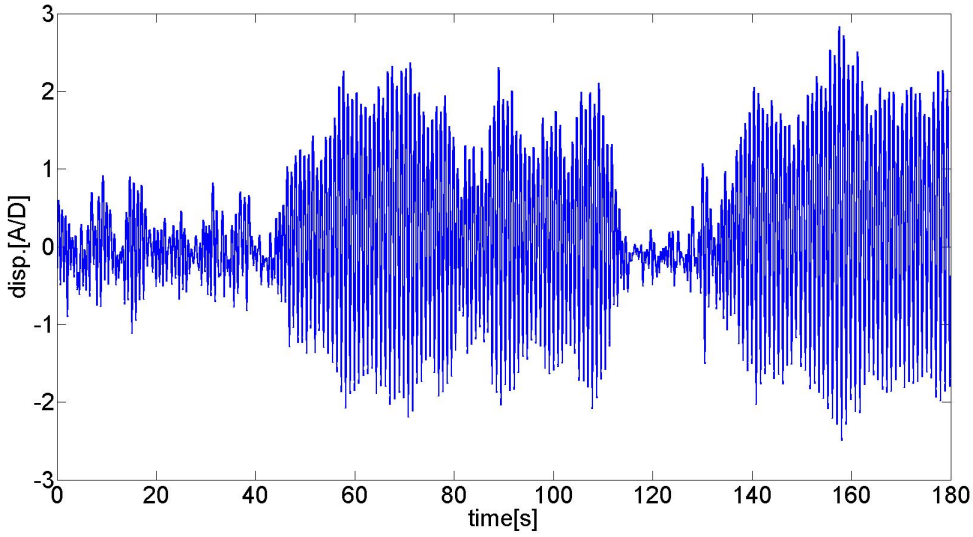

Fig. 4.13. Transition from VIV to galloping; P180:16°-32° U^*=13.77

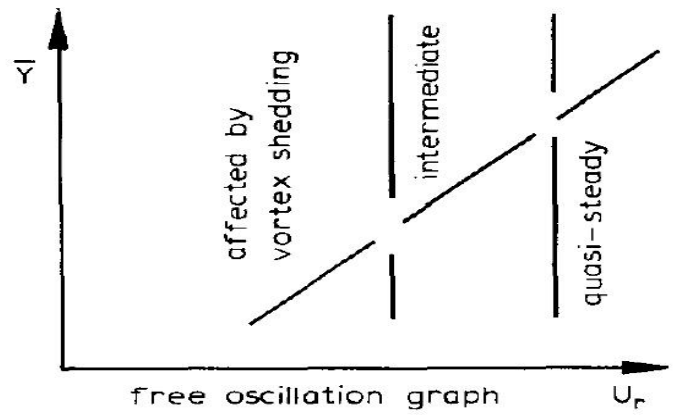

Fig. 4.14. Three different zones for square cylinder (Parkinson1990)

4.2.3. Calculation of lift coefficient and phase angle for SG zone

Using the same method as in Section 3.2.3 for a smooth cylinder, we calculate the lift coefficient and phase difference between the lift force and cylinder displacement in the SG zone. In soft galloping, the transverse force cannot be decomposed into vortex and potential forces due to an additional force driving the galloping motion. Figs. 4.15-4.17 show the results of C_{total}, F_{total}, and ϕ_{total} for P180. As shown in Fig. 4.15, the total transverse coefficient has the maximum value at the beginning of the upper branch and then the transverse coefficient drops sharply through the upper branch. In the transition from the VIV to the galloping region, the transverse coefficient is almost constant. At the onset of galloping, the transverse coefficient increases again. Even though, the value of the transverse coefficient in galloping is less than that at the onset of the upper branch, the transverse force of galloping is much higher than the VIV transverse force as seen in Fig. 4.16. After the onset of galloping, the transverse force increases sharply at U^*>13.0 and the magnitude of the force is about 2.5 times higher than that of VIV. As seen in Fig.

4.17, the phase difference between the transverse force and the cylinder displacement is close to zero in the initial branch. In the upper branch, ϕ_{total} starts to increase slowly and undergoes an abrupt jump. This jump is associated with the fact that f_{osc} passes through f_N. Since f_{osc} of the cylinder with PTC is much higher than that of the smooth cylinder, the jump occurs much earlier – lower U^* - than that of the smooth cylinder. Depending on the PTC location, some variation is observed. In the transition from VIV to galloping, ϕ_{total} starts to drop sharply. In the galloping branch, ϕ_{total} is close to zero and force and cylinder displacement are almost in-phase. It is worthy to note that in VIV the amplitude of the cylinder is mostly affected by C_{total} and ϕ_{total} as shown in equation (3.10) since VIV occurs only in a range of flow velocity. On the other hand, galloping occurs above a critical flow velocity. Besides C_{total} and ϕ_{total}, U^* is also a crucial factor in deciding the cylinder amplitude.

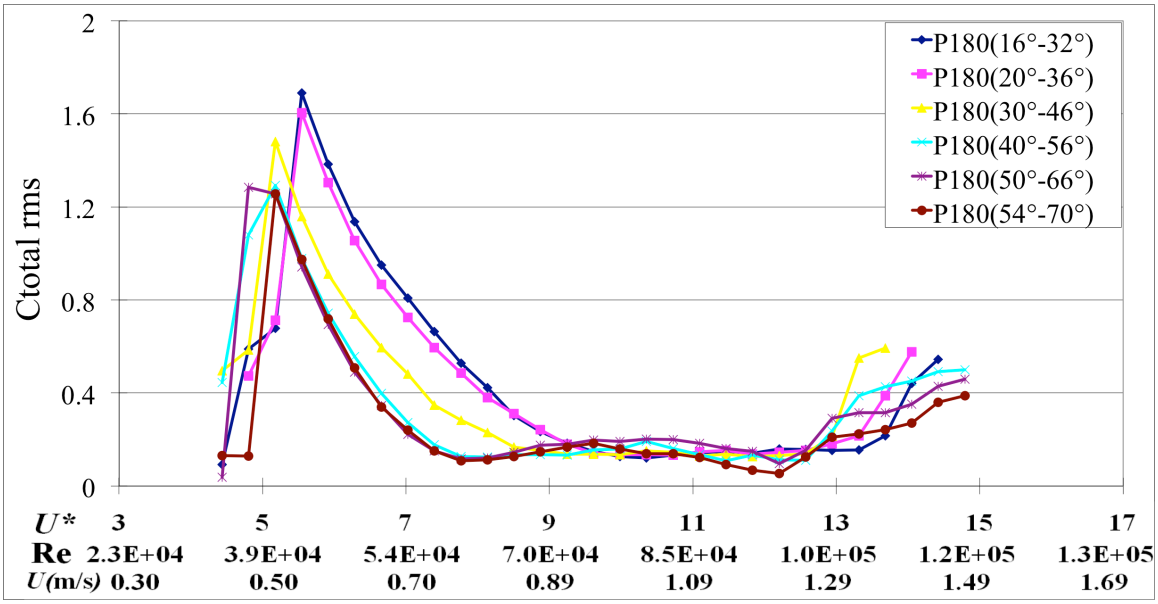

Fig. 4.15. Total transverse coefficient $C_{total\ rms}$ for SG zone of P180

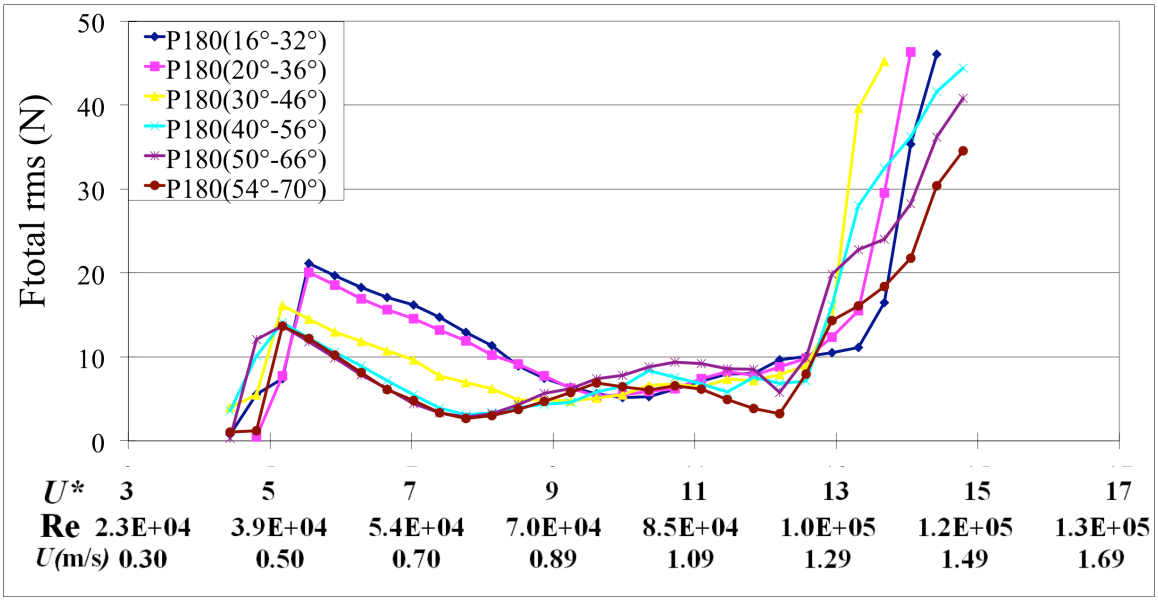

Fig. 4.16. Total transverse force $F_{total\ rms}$ for SG zone of P180

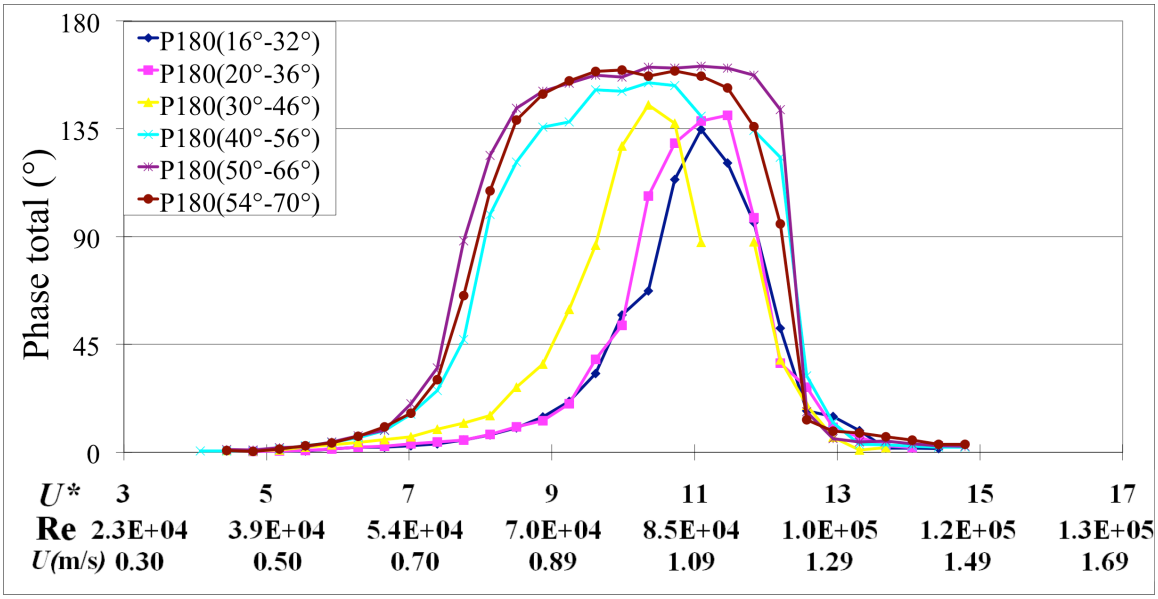

Fig. 4.17. Total phase lag ϕ_{total} for SG zone of P180

The results of P60 also show similar trends as those for the P180 results. As seen in Fig. 4.18, C_{total} has a maximum value at the beginning of the upper branch and sharply decreases in the upper branch region. In transition from VIV to galloping, C_{total} has a low

value and is nearly constant. In galloping, C_{total} increases again. For ϕ_{total}, more variation between PTC locations is observed for P60 than for P180.

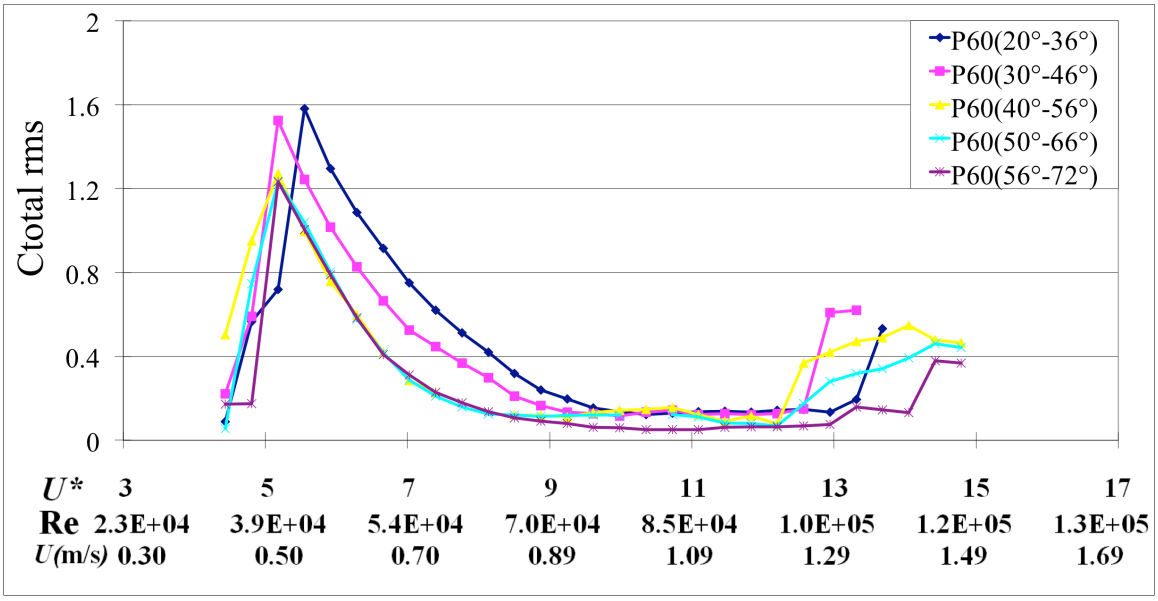

Fig. 4.18. Total transverse coefficient $C_{total\ rms}$ for SG zone of P60

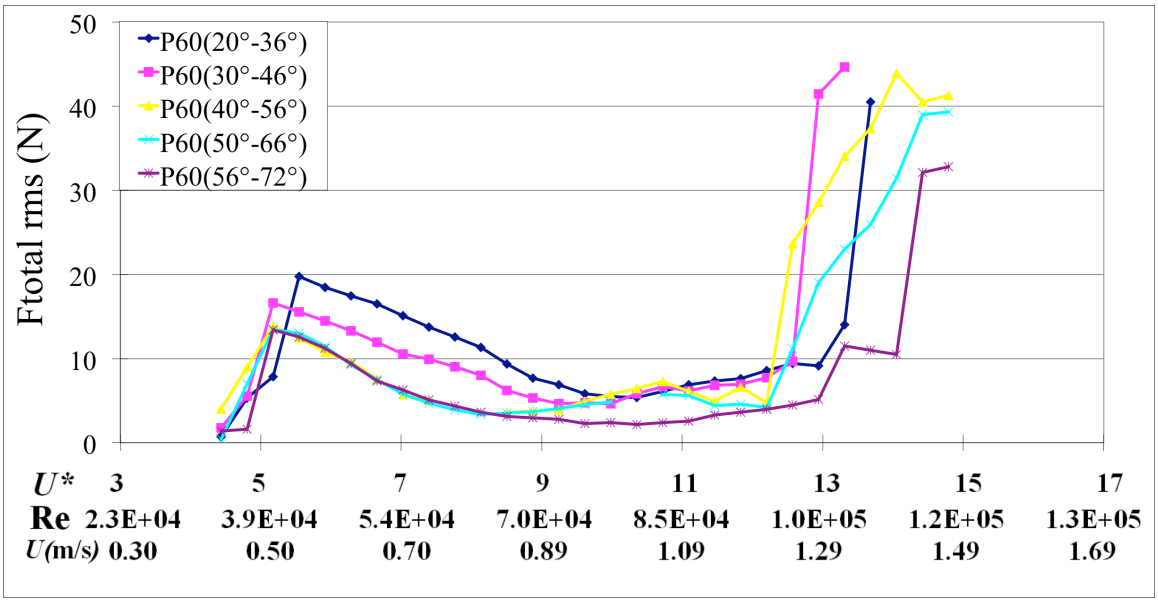

Fig. 4.19. Total transverse force $F_{total\ rms}$ for SG zone of P60

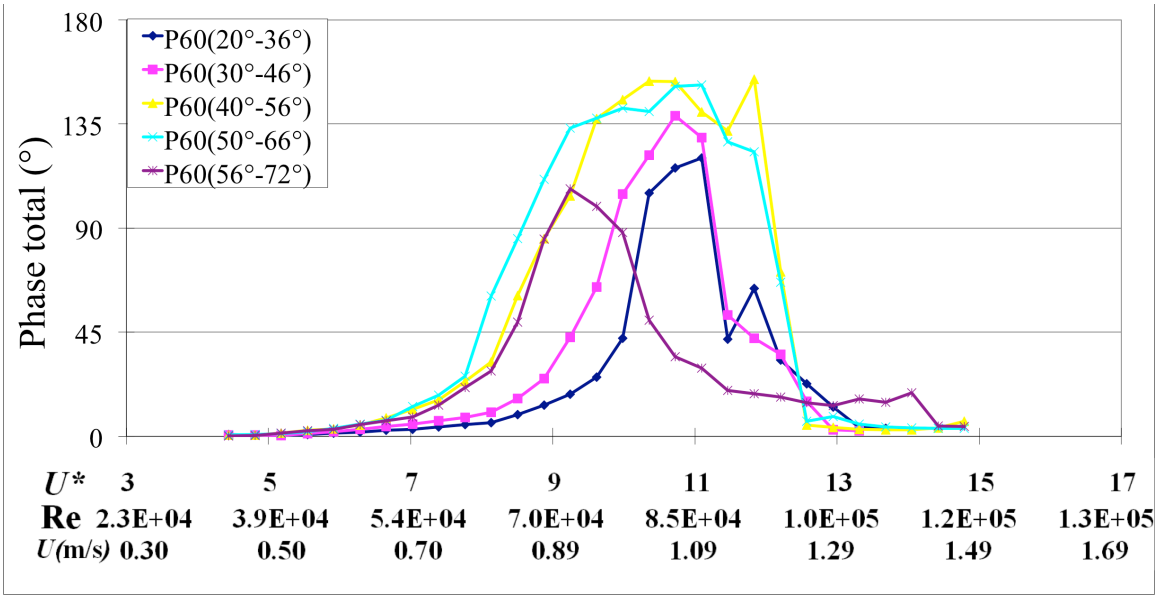

Fig. 4.20. Total phase lag ϕ_{total} for SG zone of P60

4.2.4. Wake vortex structure

4.2.4.1. Hard galloping zones (HG1, HG2)

For a typical rough cylinder case (P60:2°-18°) the flow structures are studied in the VIV and galloping ranges. In the VIV initial branch of the PTC cylinder, the vortex wake structure of the PTC cylinder is the same as for the smooth cylinder so it is not presented here. In the VIV upper branch of PTC cylinder, the basic wake vortex structures are similar to those observed for the smooth cylinder upper branch with the exception that the vortices are in general smaller in core size than in the smooth cylinder case. For example, in the PTC cylinder case, the 2P+S mode of shedding was observed but with maximum vortex size to cylinder diameter ratio of about 0.9, whereas in the case of the smooth cylinder this ratio is about 1.2. That is, maximum vortex size to diameter ratio in the

rough cylinder case is about 25% smaller than that of the smooth cylinder at identical reduced velocity in the VIV upper branch. Since vortex size indicates the circulation content of a vortex, the amount of vorticity generation in the case of rough cylinder is less than that of the smooth cylinder, which is reflected in the smaller amplitude of vibration in the upper branch of the PTC cylinder (Fig. 4.2). Since the mode of shedding observed in the upper branch of HG1, HG2, and SG is qualitatively the same as that of the smooth cylinder, the result is not presented again to avoid repetition.

About 10 vortices are shed per cycle during hard galloping. Wake vortex structures for a typical hard galloping (HG1: P60:2°-18°) cycle are shown in Fig. 4.21. These wake vortex structures correspond to a reduced velocity of U^*=14.51. At BDC (Fig. 4.21(a)), two new vortices V3 and V4 borne in the top and bottom shear layers, respectively. Vortices (V1 and V2) borne in the previous cycle are already shed in Fig. 4.21(a). As the cylinder progresses upwards, at t/T=0.138, both V3 and V4 are shed while two new vortices V5 and V6 originate as shown in Fig. 4.21(b). V5 is shed at t/T=0.275 (not shown) by Gerrard's mechanism and V6 is shed at t/T=0.241 (not shown) by the passive pushing of V7. Vortex V7 grows strong along with upward cylinder motion and gets shed along with a weaker (less circulation) vortex V8 (borne at t/T=0.344; Fig. 4.21(d)) at t/T=0.448 soon after Fig. 4.21(d). At TDC in Fig. 4.21(e), again two new vortices V9 and V10 originate in the top and bottom shear layers. V9 is a very weak (less circulation) vortex and sheds at t/T=0.551 in Fig. 4.21(f) soon after its genesis, whereas V10 is shed at t/T=0.586 in Fig. 4.21(g). The near-wake witnesses formation of V11 in the top shear layer at t/T=0.551, and V12 and V13 simultaneously at t/T=0.69 in Fig. 4.21(h). V11 is shed at t/T=0.690 and V13 is shed at t/T=0.897 (not shown). Hence, as mentioned earlier,

a total of 10 vortices (V3, V4, V5, V6, V7, V8, V9, V10, V11, and V13) are shed per cycle of oscillation.

Wake structures for a typical case of HG2 have also been analyzed for the configuration P180:58°-74° at U^*=14.88. It is found that, the wake structures are similar to those of hard galloping in zone HG1, and soft galloping which is introduced in Section 4.2.3.2 with 10 vortices shed per cycle of oscillation (hence, not presented here) but with wakes constituted with smaller (in core size) vortices (carrying lesser vorticity). Correspondingly, for this HG2 configuration (P180:58°-74°), the maximum amplitude achieved is about $A^* \cong 1.58$ (Fig. 4.2) which is less than that of SG and HG1.

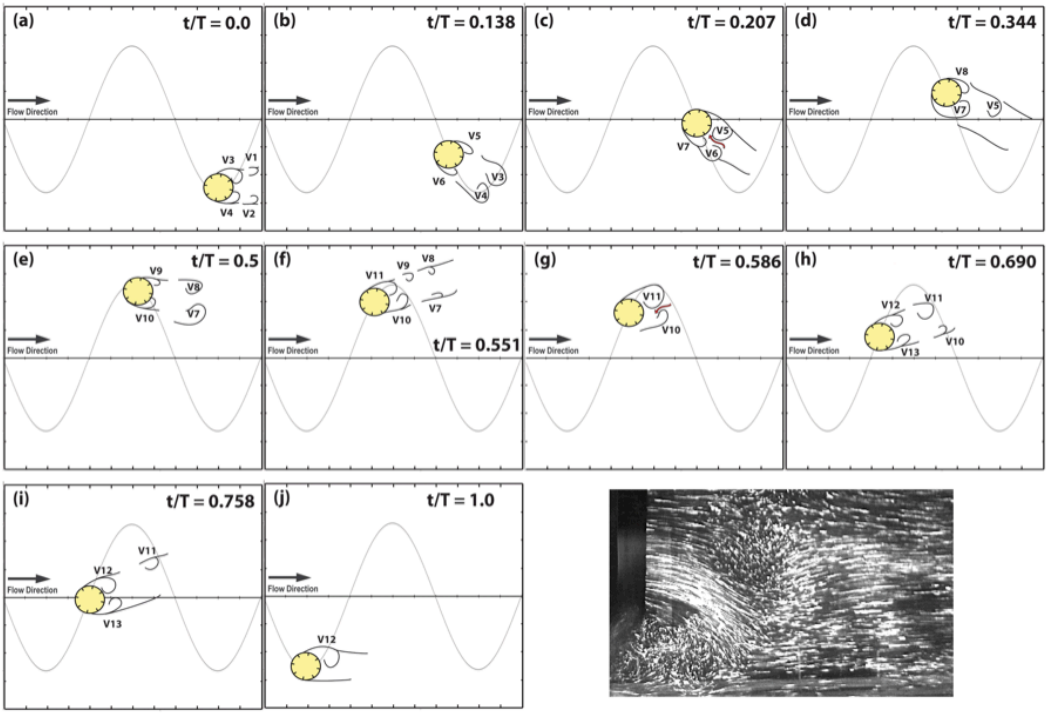

Fig. 4.21. Wake vortex structures around rough cylinder during a typical HG1 cycle: P60:2°-18°: U^*=14.51, Re=1.16×10^5, A^*=2.31; visualization picture shows instant (a) at t/T=0

4.2.4.2. Soft galloping zone (SG)

Typical vortex structures for the soft galloping branch (P180:20°-36°) are presented in Fig. 4.22. In this case, the maximum amplitude value is $A^*\cong 2.89$ (Fig. 4.8) and the corresponding $U^*\cong 14.14$. Starting from BDC, as the cylinder traverses up, a new vortex V2 forms in the bottom shear layer which sheds together with V1 at t/T=0.12 (Fig. 4.22(b)). Also at t/T=0.12, two new vortices, V3 and V4 are simultaneously borne in the top and bottom shear layers, respectively. V3 and V4 shed at t/T=0.32 (Fig. 4.22(d)); V3 is shed following the classical mechanism suggested by Gerrrad (1966) whereas V4 is shed due to the passive pushing of V4 (passive shedding mechanism). Acute wake swing is observed during the course of cylinder travel. During the cylinder upward traverse, vortex V5 is borne at t/T=0.24 (Fig. 4.22(c)) and V6 at t/T=0.40. V5 exhibits considerable build up of circulation and grows to significant size whereas V6 is a short-lived, weak (less circulation) vortex. V5 and V6 shed at t/T=0.52 where another two new vortices V7 and V8 originate (Fig. 4.22(f)). V7 sheds at t/T=0.72 (Fig. 4.22(i)) and V8 at t/T=0.64 (Fig. 4.22(g)) during the return journey of the cylinder, i.e., from TDC to BDC. V7 and V8 shed by passive pushing by their respective co-generated (generated by the same shear layer) vortices. V9 (borne at t/T=0.64) grows to a substantially strong vortex (like V5) at shedding when the cylinder is close to BDC again (at t/T=0.92 not shown). Top shear layer contributes one more vortex in this cycle, namely V10 (formed at t/T=0.72; Fig. 4.22(i)) which is ultimately shed at t/T=0.84 (Fig. 4.22(k)). The major vortices (stronger) observed in this cycle are V3, V5 and V9. A total of 10 vortices (V1,

V2, V3, V4, V5, V6, V7, V8, V9, and V10) are shed per cycle of galloping oscillation, which is considerably higher than that in the VIV upper branch, where 2P+S is the mode of shedding which is equivalent to 5 vortices per cycle.

Flow fields in a few more oscillatory cycles of soft galloping are examined and are similar to hard galloping presented in Fig. 45. Minor deviations are observed in few cycles and are not presented here. Simultaneous vortex birth (e.g., V7 and V8 in Fig. 4.22(f); V9 and V10 in Fig. 4.21(e)) and vortex shedding (e.g., V5 and V6 in Fig. 4.22(f); V3 and V4 in Fig. 4.21(b)) by the top and bottom shear layers with significant wake swing is a unique characteristic of the galloping wake structure. In the case of smooth cylinder, simultaneous vortex birth is observed (Fig. 3.21(f)) only occasionally.

At many instances during the oscillatory cycle, the wake vortex structures are closely similar to those observed in the hard galloping cycle in Fig. 4.21. For example, the vortex pattern at t/T=0.138 in Fig. 4.21(b) is similar to that at t/T=0.12 in Fig. 4.22(b). The hard galloping wake pattern at t/T=0.16 (not shown) is also nearly the same as that of soft galloping at t/T=0.12 in Fig. 4.22(b). Therefore, the hard galloping flow structure at t/T=0.14 in Fig. 4.21(b) should be identical to the soft galloping flow structure at t/T=0.12 in Fig. 4.22(b). Similarly, the soft galloping wake structure at t/T=0.24 in Fig. 4.22(c) resembles the hard galloping wake structure at a closely identical time instant, t/T=0.207 in Fig. 4.21(c). Same is the case with hard galloping flow structure at t/T=0.758 in Fig. 4.21(i) which is similar to soft galloping at t/T=0.76 in Fig. 4.22(j). From the results, it follows that, once the cylinder is excited to galloping oscillations, the wake patterns are closely similar whether it executes soft galloping or hard galloping.

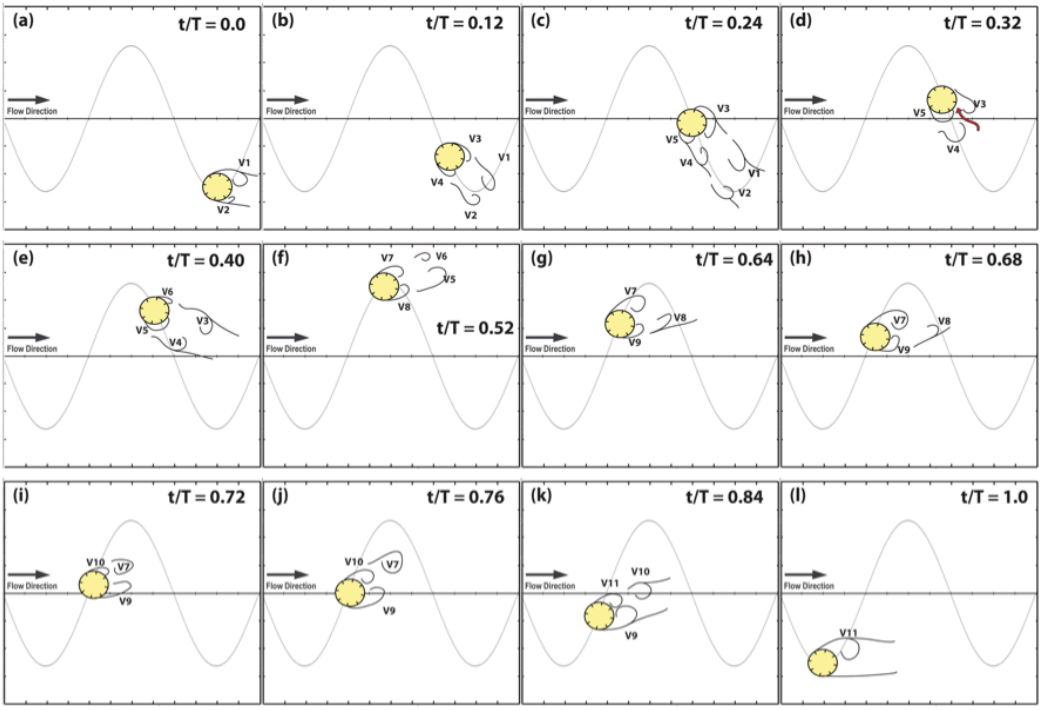

Fig. 4.22. Wake vortex structures around rough cylinder during a typical SG cycle: P180:20°-36°: U^*=14.14, Re=1.09×10^5, A^*=2.89

4.2.4.3. Comparison of VIV to galloping wake vortex structures

Body acceleration could be a major factor in genesis of new vortices (Honji & Taneda 1969; Williamson & Roshko 1988). This is confirmed in the present study as shown in Fig. 3.21(b). On the other hand, results show that new vortices need not be generated at the maximum acceleration position (BDC/TDC) of the cylinder travel. Instead, vorticity roll up may occur at cylinder positions other than BDC/TDC e.g., Fig. 3.21(d) for V4 and Fig. 3.21(i) for V5 and V6.

As mentioned in Section 3.2.4.1, wake vortex structures could differ depending on the oscillation frequency ratio besides Reynolds number and reduced velocity. Accordingly, apart from conventional wake vortex structures in VIV, such as 2P+S observed in the

upper branch in the present study (Fig. 3.21), other flow structures with no vortex pairing also exist giving rise to similar cylinder excitation levels.

In galloping, as shown in Sections 4.2.4.1 and 4.2.4.2 and Figs. 4.21 and 4.22, the flow structures are significantly different from those in VIV reported in the literature (Williamson & Roshko 1988). Galloping exhibits considerably higher number of vortices shed per cycle of oscillation and acute wake swings. Simultaneous generation and shedding of vortices by the top and bottom shear layers with significant wake swing is a unique characteristic of the galloping wake structure. Additional relative motion-induced vortices, contributing to higher number of vortices, are generated during galloping due to the application of surface roughness. This agrees with the observation by Bokaian & Geoola (1984) that during galloping, vortex shedding frequency increases. A stand alone, smooth circular cylinder does not gallop since the derivative of lift coefficient with respect to the flow incidence angle is zero (Alonso et al. 2009). But, with the introduction of straight roughness strips, the geometry is changed to an effective non-circular section. Almost all non-circular bluff sections are prone to galloping being influenced by the angle of attack (Blevins 1990; Parkinson 1971) particularly at reduced velocities less than 100 (Nakamura et al. 1991). The galloping wake structures observed in the present study are attributed to the effect of flow incidence angle generating relative motion induced forces leading to galloping (Parkinson & Sullivan 1979). These forces are due to the asymmetric, unsteady reattachment of the shear layers (Higuchi et al. 1989) promoted by surface roughness. Based on simple mechanics, it is clear that, these wake vortex structures give rise to surface pressure distributions favorable for the occurrence of

galloping. However, surface pressure measurements were not carried out in the present study.

4.3. MAIN FINDINGS

The PTC-cylinder has two HG zones, for both roughness P180 and P60. These two zones, HG1 and HG2, have some common features and some features that distinguish them. From the results presented in Section 4.2.1 we can draw the following conclusions:

(i) Both zones require a threshold amplitude of about $1 \bullet D$ to initiate galloping at high reduced velocities.

(ii) In the HG1 zone, the amplitude response graph exhibits a broader VIV upper branch and higher amplitude at galloping than the corresponding values in the HG2 zone.

(iii) Prior to the onset of hard galloping at high reduced velocities, in HG1 there is small amplitude motion while in HG2 the cylinder remains nearly stationary.

(iv) The closer is the roughness strip to the forward stagnation point (far away from strong suppression zone) the higher is the amplitude in the VIV region.

(v) In both hard galloping zones the PTC cylinder response in the initial and upper branches ($U^*<11$) with either P180 or P60, has higher frequency ratio than that of the smooth cylinder.

(vi) After initiation of hard galloping in both HG1 and HG2, the frequency ratio is close to unity and higher harmonics are observed in the power spectra.

(vii) Prior to the onset of hard galloping, the frequency ratio f^* in all HG2 cases is generally higher than that of HG1.

(viii) The lower VIV branch occurs in the range of reduced velocity $11.5 \leq U^* \leq 14.5$ for the smooth cylinder. In almost all case considered here, the lower VIV branch of the PTC cylinder is followed by galloping rather than desynchronization.

From the results presented in Section 4.2.2 we can draw the following conclusions for soft galloping of P180 and P60:

(i) The response of the cylinder with PTC in SG has three major regions in terms of reduced velocity; VIV, transition from VIV to galloping, and galloping.

(ii) For all soft galloping cases, except for P60:58°-74°, $A^* \geq 2.4$ is achieved as early as $U^* \cong 13.0$ but no later than $U^* \cong 15$.

(iii) For strip placement angles <40°, the larger the angle is the earlier (at lower reduced velocities) the initiation and full development of galloping occurs.

(iv) For strip placement angles ≥40°, the larger the roughness location angle (closer to the strong suppression zone) is the later the initiation of galloping occurs, and the less the amplitude in VIV and galloping region is.

(v) The closer to the front stagnation point PTC is located, the higher is the response amplitude in the VIV upper branch.

(vi) When galloping is initiated, frequency ratio f^* approaches unity.

(vii) In transition from VIV to galloping, amplitude modulation is observed. This is due to the transition process where the VIV driving force (oscillatory lift due to vortex shedding) changes gradually to the galloping driving force (instability

inducing oscillatory lift due to shear layer motion). At galloping, the amplitude modulation disappears and steady motion is observed.

From the results presented in Section 4.2.4, we can draw following conclusions for wake vortex structures of HG1, HG2, and SG:

(i) For HG1, HG2, and SG, higher number of vortices (10) is shed and acute wake swing is observed in galloping. Different from VIV, simultaneous generation and shedding of vortices by the top and bottom shear layers is observed. This is consistent wit h the fact that the mechanism of oscillatory lift in galloping is different from that of VIV, which is it is not based on vortex shedding.

CHAPTER 5

FIM SUPPRESSION WITH PTC

5.1. LITERATURE REVIEW

From the engineering safety point of view, VIV results in large oscillations and may damage or destroy structures such as offshore structures, bridges, stacks, and heat exchanger tube array to name a few. Hence, suppressing VIV is important to prolong life-span and reduce fatigue damage of structures. Suppression research in active and passive control methods has been carried out for several decades. In the present work, only passive control is discussed only as active control is of marginal relevance here.

An active means is a way that influences control structural properties directly. Prandlt found that the flow field around a circular cylinder was modified, and a drag force was reduced by suction and blowing of water through to the cylinder surface. Since then, Baz & Ro (1991) used an active control damper to reduce added mass in a wide range of reduced velocity in contrast to passive damper, which could be used only in a short range of reduced velocity. Kubo et al. (1993) investigated VIV suppression using a separated flow control by accelerating a boundary layer on the surface.

The active control method, however, can be limited by severe environment such as deep flowing water. Meanwhile when a device runs under known inputs, a passive method is a better means in a sense since it is simple and easy to fabricate and handle. A passive means is another way to suppress VIV by changing geometry or adding on devices. Passive control has been the predominant means by (a) increasing damping, (b) avoiding resonance, (c) stream-lining the body geometry, (d) introducing add-on devices, (e) modifying body-surface, (f) controlling boundary layer, and (g) using interfering body (Blevins 1990, Kumar et al. 2008).

Most of passive means use geometry modification or introduce three-dimensional disturbance into the flow. Owen et al. (2001) used a plain cylinder with bump and the bumpy cylinder reduced drag and vortex shedding compared to a plain cylinder. Tombazis & Bearman (1997) researched three-dimensional geometric disturbance effect on bluff body wakes using a spanwise wavy trailing edge. They found that stimulating the formation of vortex dislocations more reduces drag more. Wong and Kokkalis (1982) investigated three aerodynamic devices (a perforated shroud, helical strakes, and longitudinal slats) in a wind tunnel. All three devices were effective in VIV suppression when a structural damping coefficient ($k = 2M\delta_{sys} / \rho D^2$ where M (mass per unit length), δ_{sys} (logarithmic decrement of oscillating system in still air), ρ (fluid density), D (cylinder diameter)) was greater than 3 and the slat-all round device had the best performance overall in VIV suppression. Lubbad et al. (2011) researched round-sectioned helical strakes, which was easier to be mounted on a riser than typical helical strakes. In their research, the rounded-sectioned helical single rope was not efficient in VIV suppression since one rope was not sufficient to make the flow three-dimensional. The

result was two-dimensional vortices produced in some parts of the cylinder. These two-dimensional shed vortices were able to sustain VIV. Furthermore, helical strakes suppress the excitation to negligible levels but with a high drag penalty. On the other hand fairings, another well known passive suppression device, subdue VIV by about 80% without incurring higher drag. Fairings though, have high initial installation cost, add weight to the structure, and are difficult to handle. Additionally, fairings lose their streamline geometry due to marine build up diminishing their effectiveness. Comprehensive reviews of all passive control devices point to the need to build a device which suppresses the flow-induced motions significantly without increasing drag and is easy to handle, inexpensive, and light. A broad range of passive control means to suppress VIV was reviewed by Zdravkovich (1981), Every et al. (1982), and Kumar et al. (2008). As seen in Fig. 5.1, Zdravkovich studied various passive means changing geometry and classified the most popular passive means into three categories. These three passive means categories are widely used in industries and are introduced briefly in following paragraph.

(a) Surface protrusion, which affects the separation lines and/or the separated shear layers. These examples are helical strakes, wires, fins, studs or spheres.

(b) Shrouds which affect the entrainment layers. Suppression devices using shrouds are perforated, gauze, axial-rod, axial-slat.

(c) Nearwake stabilisers which prevent interaction of entrainment layers. Splitter plates, guiding vanes, base-bleed, slits cut across the cylinder are typical devices of this category.

Most suppression devices in the first two categories are flow direction independent

and they can be used regardless of flow direction. Some devices in the first and all in the third category are flow direction dependent so that they can be used only for one directional flow.

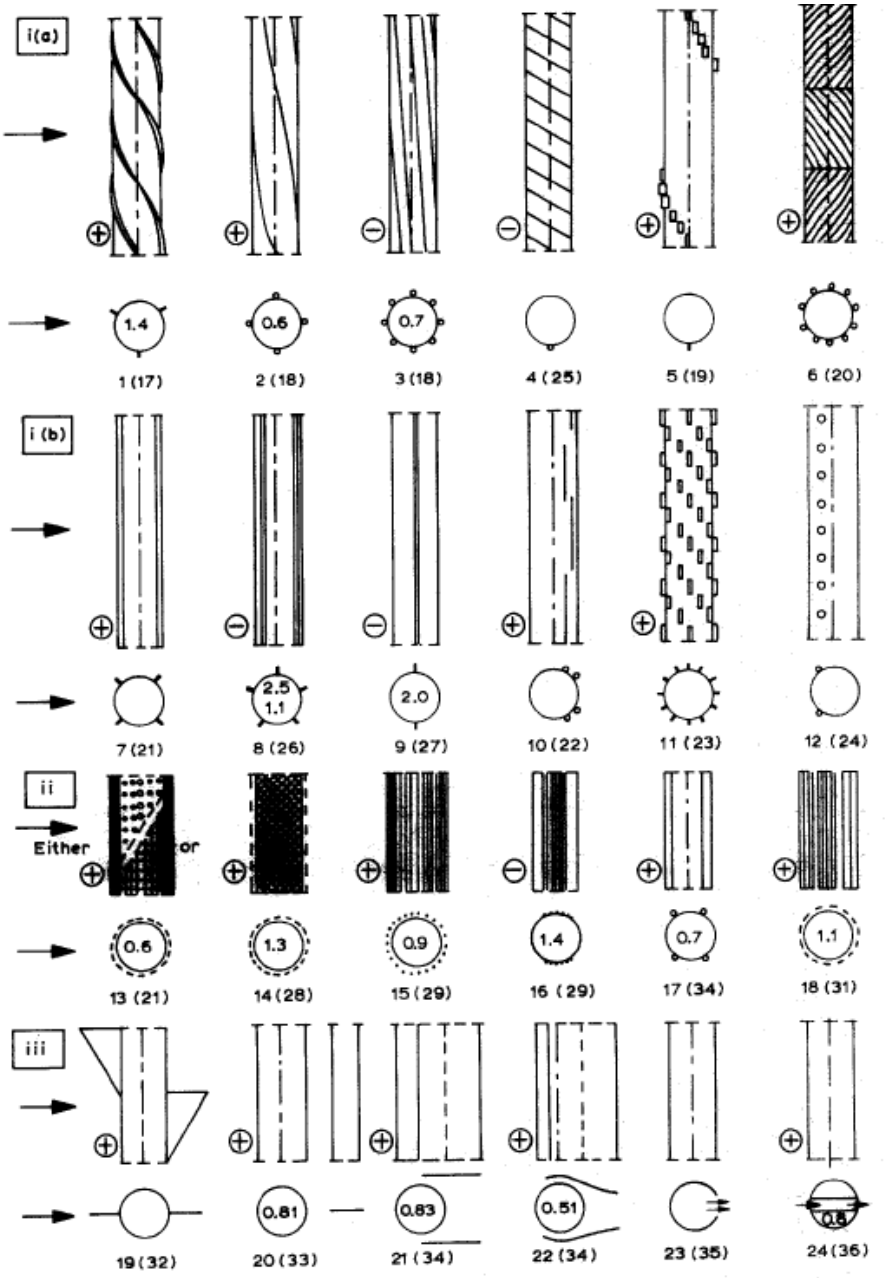

Fig. 5.1. Aerodynamics and hydrodynamics means for interfering vortex shedding (i) surface protrusion (a) omni-directional (b) uni-directional (ii) shrouds (iii) nearwake

stabilizer from Zdravkovich (1981)

5.2. RESULTS, OBSERVATIONS, AND DISCUSSION

5.2.1. Weak suppression

The results for amplitude and frequency response in the two weak suppression zones identified are discussed in Section 5.2.1.1. In Section 5.2.1.2, a few displacement time histories and the corresponding power spectra of each WS zone are presented.

5.2.1.1. Amplitude and frequency response

A. Results for P180 in WS1 ($0°\leq\alpha<2°$) and WS2 ($106°\leq\alpha\leq180°$)

For P180 roughness strip, two zones of weak suppression (namely WS1 and WS2) have been identified. They are shown in Figs. 6.1(a) and (b) and designated as $0°\leq\alpha_{PTC}<2°$ (WS1) and $106°\leq\alpha_{PTC}\leq180°$ (WS2), where angle α range indicates zone width. The angle α is defined by the location of the leading edge of the roughness strip, where 0° corresponds to the ideal flow upstream stagnation point. Weak suppression is defined as the case where the maximum amplitude of oscillation is no less than 75% of the smooth cylinder amplitude.

The response amplitude and frequency are shown in Figs. 5.2 and 5.3. As shown in Fig. 5.2, for the case P180:0°-8° (WS1), subsequent to the upper branch ($6.0\leq U^*\leq10.7$), a lower branch appears extending from $U^*\cong10.7$ to 13.7 followed by desynchronization.

The amplitude and branches are not significantly different except in the reduced velocity range $9.5 \leq U^* \leq 11.5$ from those of the smooth cylinder. For WS2, the amplitude and branches closely follow those of the smooth cylinder except in the reduced velocity range $9.0 \leq U^* \leq 11.5$. Particularly, the initial branch and upper branch of WS1 and WS2 are identical to the initial and upper branch of the smooth cylinder. Onset of the initial branch is at $U^* \cong 4.5$ and of the upper branch at 5.8 for both smooth and PTC cylinders. P180:0°-8° and all P180:106°-180° PTC configurations (variable radial location) show less amplitude and shorter synchronization regions than those of the smooth cylinder except for the case P180:140°-156° where amplitudes higher than the corresponding smooth cylinder amplitudes are measured in the range $7.0 \leq U^* \leq 9.0$. That is, there is a local amplification of response for the case P180:140°-156° within a short range of U^*.

As shown in Fig. 5.3, frequency ratio ($f^* = f_{osc}/f_{n,w}$) of all WS responses follow that of the smooth cylinder and gradually increase up to around 1.3. In the upper branch ($6.0 \leq U^* \leq 10.7$), WS1 response has higher f^* and WS2 has lower f^* than that of the smooth cylinder. In this range, higher strip angle in general results in higher frequency ratio between WS2 responses. When strip is placed close to the base region of the circular cylinder, frequency response is very close to that of smooth cylinder.

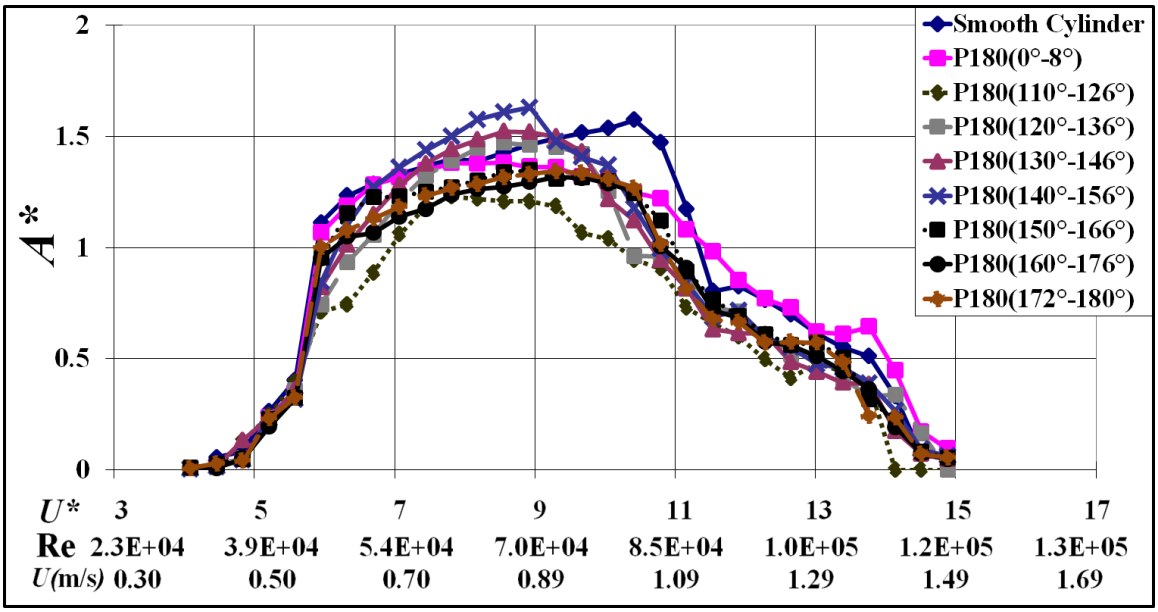

Fig. 5.2. Amplitude response features for different configurations of P180

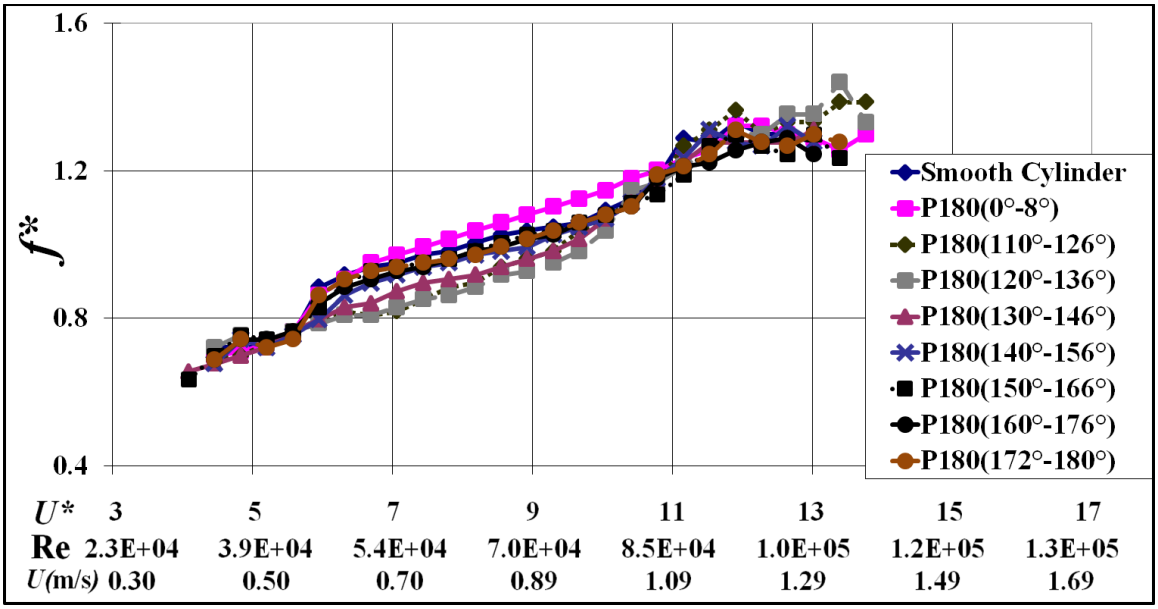

Fig. 5.3. Frequency response features for different configurations of P180

B. Results for P60 in WS1 ($0° \leq \alpha_{PTC} < 2°$) and WS2 ($106° \leq \alpha_{PTC} \leq 180°$)

For strip P60, two weak suppression zones are identified WS1 ($0°\leq\alpha_{PTC}<2°$) and WS2 ($106°\leq\alpha_{PTC}\leq180°$) as in the case of P180. For both P60 and P180, amplitudes closely follow the smooth cylinder values, except for the range $9.0\leq U^*\leq11.25$, as observed in Fig. 5.4. In WS2, same as P180 the farther to the back of the cylinder the roughness strip is placed, the more ineffective PTC becomes resulting in increased amplitude and range of synchronization.

Furthermore, the oscillation frequency increases with reduced velocity for all the WS1 and WS2 cases up to $U^*\cong12.0$ (Fig. 5.5). Thereafter, the frequency of oscillation decreases but for the case P60:110°-126°, where f^* abruptly increases for $U^*>12.2$. However, further trend of f_{osc} could not be captured for this case due to desynchronization. For high U^* values ($U^*>12.0$), the abrupt increase noticed for P60:110°-126° could not be observed for P180:110°-126°.

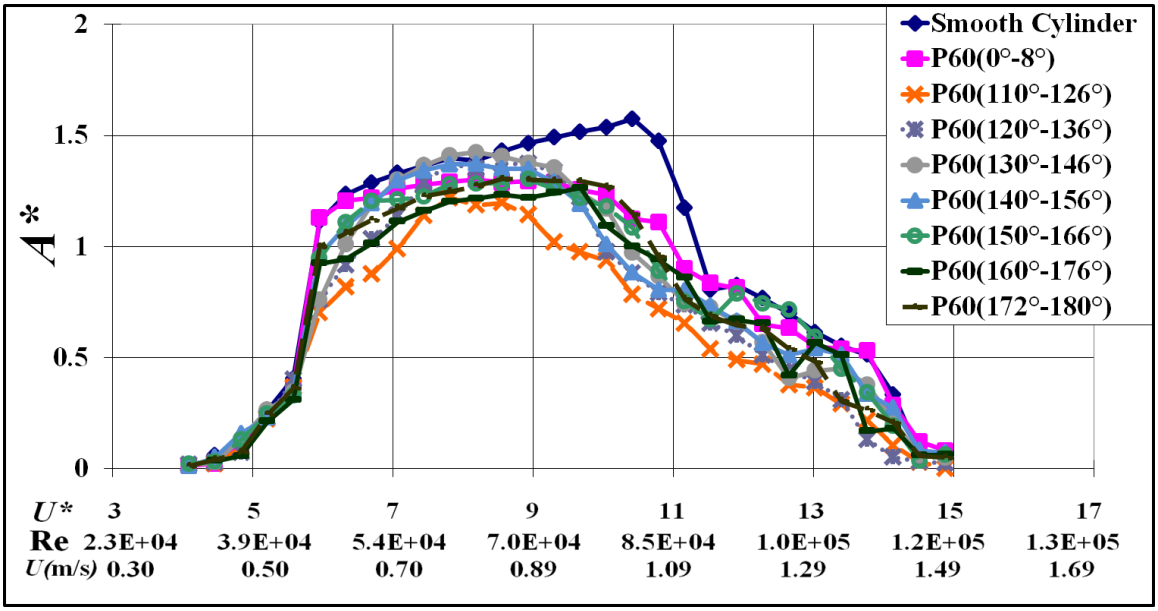

Fig. 5.4. Amplitude response features for different configurations of P60

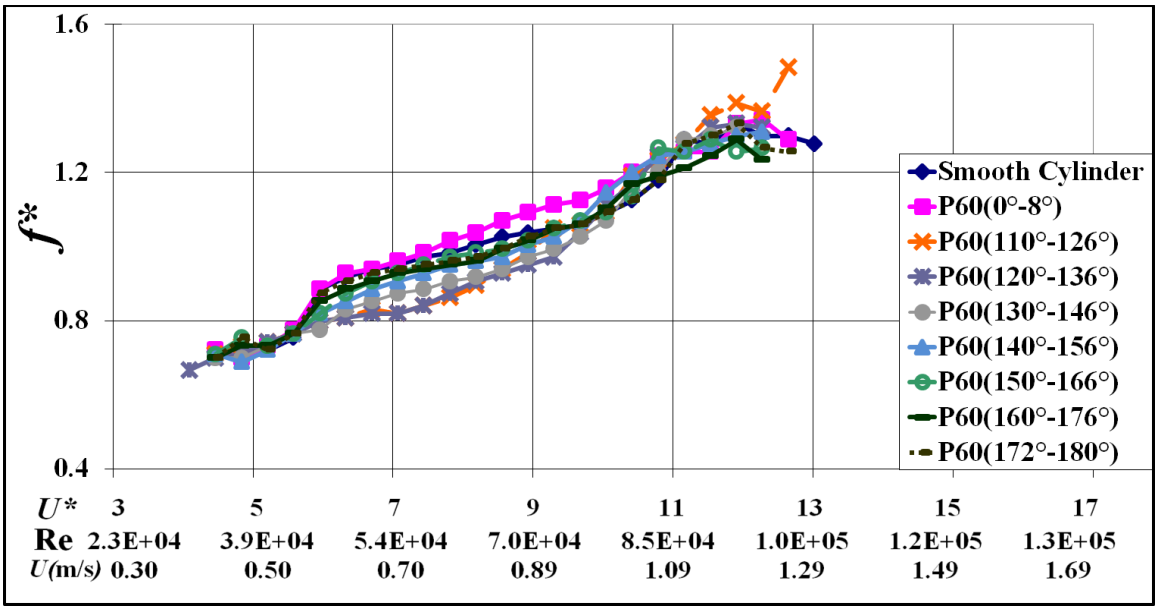

Fig. 5.5. Frequency response features for different configurations of P60

5.2.1.2. Displacement and power spectrum

(i) Results in WS1: (P180:0°-8°, P60:0°-8°)

The displacement time histories of the response at different reduced velocities of a typical case P180:0°-8° are shown in Figs. 5.6(a)-(i). During the onset of oscillations corresponding to the initial branch (U^*=4.84), response is quasi-periodic similar to that of the smooth cylinder (Fig. 3.9(a)) but with greater separation between groups of oscillations. These group separations indicate the existence of vortex shedding in the near-wake of the cylinder with the shedding frequency being not completely 'locked-on' to the body motion frequency. The corresponding spectrum (Fig. 5.6(a)) shows the existence of a predominant spike corresponding to the oscillation frequency (f_{osc}≅0.78). As the reduced velocity increases to U^*=5.60 in initial branch, oscillations become more regular and steady (Fig. 5.6(b)) indicating complete 'lock-on'. The corresponding

spectrum shows a significant spike at f_{osc}≅0.86. Then, at U^*=8.56 in the upper branch of the response, significant oscillations are recorded as shown in Fig. 5.6(c). Spectrum shows a major spike, which corresponds to the oscillation frequency, and two minor spikes at the second and third harmonics. At a still higher reduced velocity (U^*=10.42 almost at the end of upper branch; Fig. 5.6(d)), amplitude modulation is observed indicating that motion is not 100% steady. The corresponding spectrum shows only the second harmonic besides the major spike due to the oscillation frequency. A weak lower branch follows the upper branch in the range $10.7 \leq U^* \leq 13.7$. Typical lower branch characteristics of WS1 are shown in Figs. 5.6(e)-(f). Oscillations are not steady, similar to the smooth cylinder case (Fig. 3.9(e)). At U^*=11.91 (Fig. 5.6(e)), spectrum shows that displacement exhibits definite periodicity at the oscillation frequency with absence of any higher harmonics. At a still higher reduced velocity (U^*=13.4) but within the lower branch, the spectrum is more uniformly distributed (Fig. 5.6(f)) and the corresponding amplitude wave forms show non-steady oscillations bearing the characteristics of desynchronization. In desynchronization weak and unsteady oscillations are recorded (U^*=14.14 Fig. 5.6(g); U^*=14.89, Fig. 5.6(h)). The corresponding displacement spectra show more or less distributed patterns. In order to investigate the possibility of hard galloping (at U^*=14.89), the cylinder (otherwise nearly stationary) was manually displaced and then released; no galloping was observed. The cylinder was then forced manually into oscillations as shown in Fig. 5.6(i). It was found that oscillations died out after a few cycles (Fig. 5.6(i)). This exercise was repeated twice for verification.

In general, the response features with the P60 strip are similar to those with P180. Figs. 5.6(j)-(k) show the displacement time histories and spectra for P60:0°-8° only at

U^*=8.56 and 11.91. Similar to P180, the rougher cylinder P60 has regular steady oscillations at U^*=8.56 in the upper branch and irregular and unsteady in the lower branch at U^*=11.91. The corresponding spectra are also similar to P180 at the same U^*.

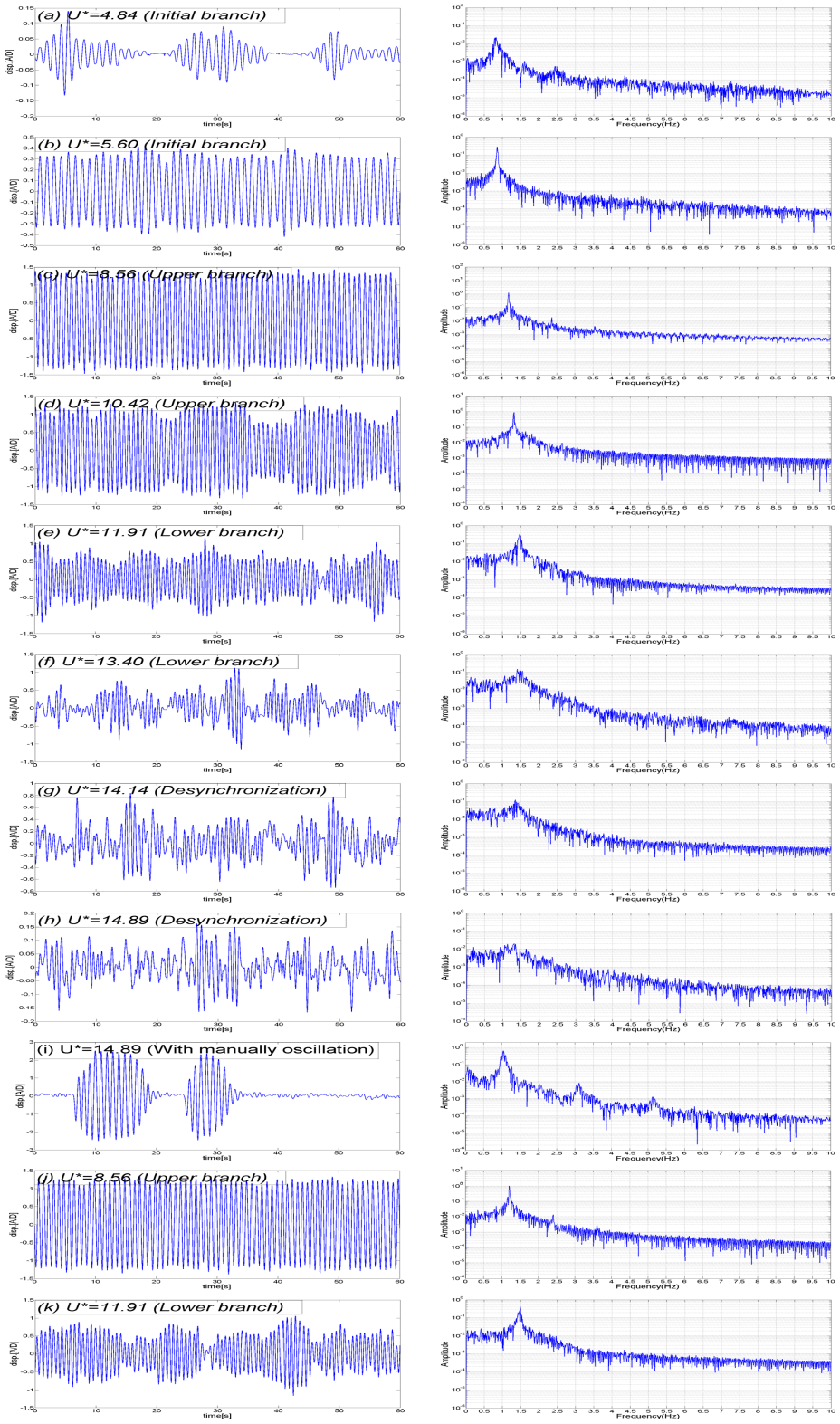

Fig. 5.6. Displacement time series and power spectra for WS1:0°-8° (a)-(i) for P180 and (j)-(k) for P60

(ii) Results in WS2: (P180:140°-156°)

A second weak suppression zone (WS2) is identified ($106° \leq \alpha_{PTC} \leq 180°$). The displacement time histories in WS2 are similar to those in WS1. The following case is selected as examples: P180:140°-156° and results are shown in Figs. 5.7(a)-(b). Starting from the onset of VIV at U^*=4.84 (Fig. 5.4), the WS2 response exhibits similar time histories and spectra of displacement (Figs. 5.7(a)-(b)) when compared to WS1 response (Figs. 5.6(c) and 5.6(f)). For P60:140°-156°, the oscillatory characteristics are similar to those of P180:140°-156° at the respective reduced velocities, so, they are not presented in this paper for brevity.

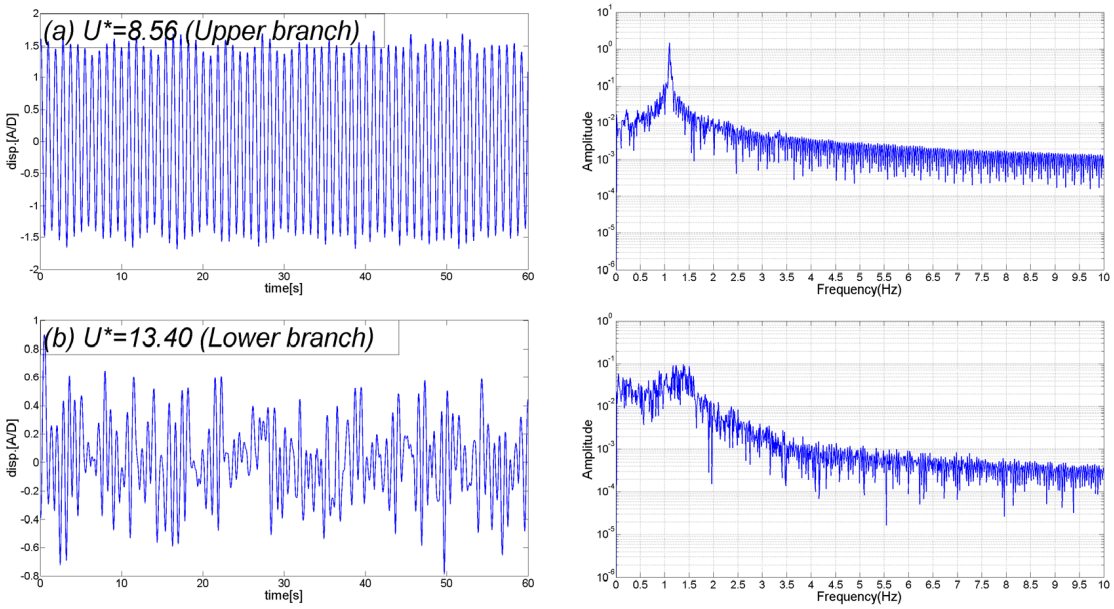

Fig. 5.7 Displacement time series and power spectra for WS2: P180:140°-156°

5.2.2. Strong suppression

The results for amplitude and frequency response in the strong suppression zone are discussed in Section 5.2.2.1. In Section 5.2.2.2, a few displacement time histories and the corresponding power spectra of the SS zone are presented.

5.2.2.1. Amplitude and frequency response

A. Results for P180 in SS ($60° \leq \alpha_{PTC} \leq 104°$)

In this paper, as mentioned in Chapter 4 cases where the maximum amplitude is suppressed by 25% or more - compared to the smooth cylinder response - are classified as strong suppression cases. Fig. 5.8 shows the amplitude in strong suppression cases for the smoother strip (P180). The following observations can be made: (i) For P180:60°-76°, onset of synchronization starts earlier than in the smooth cylinder case. A high amplitude ($5.5<U^*<9.2$) region and a lower amplitude ($9.2<U^*<11.5$) region corresponding to the upper and lower branch, respectively, are present. Then, desynchronization ($11.5<U^*$) follows. (ii) When the strip upstream edge is located at 70°, for P180:70°-86°, predominant oscillations are limited to a very narrow range of reduced velocity, $5.5<U^*<6.5$. For $U^*>6.5$, oscillations are significantly suppressed particularly for $U^*>12.5$. This range of the roughness strip covers the separation point in laminar flow with its oscillation due to vortex shedding. Igarashi (1983) researched tripping wire on various circumference locations on a circular cylinder and found three flow patterns – laminar boundary reattachment, turbulent boundary reattachment, and separation on wire. The starting point of the SS zone is similar to immediate turbulent boundary reattachment point. Hence, the separation point moves downstream and vortex shedding frequency

would be increased with less pressure drag. (iii) For yet larger strip placement angles ($\alpha_{PTC}\geq 80°$), the upper branch is extended up to $U^*\cong 11.4$ with notable amplitudes and is followed by the lower branch. The strip placement angle α_{PTC} =80° has a more gradual onset and the lower branch extends past $U^*\cong 15$.

A typical frequency response of strong suppression is shown in Fig. 5.9. The following observations can be made: (i) Two configurations (P180:60°-76° and P180:70°-86°) with shorter upper branch range have higher oscillation frequency ratio than that of the smooth cylinder. Configurations with larger strip placement angle $80°\leq\alpha_{PTC}\leq 100°$ have wider upper branch and lower frequency ratio than that of the smooth cylinder in the upper branch region. For P180:60°-76°, the frequency increases with U^* but with a small peak at $U^*\cong 12.5$. (ii) The strongest suppression takes place for the case P180:70°-86° for $U^*>7.5$ (Fig. 5.8). For this strong suppression case, beyond $U^*=7.5$, there is no predominant frequency observed and so, frequency distribution is plotted only up to $U^*=7.5$ (Fig. 5.9). The narrow high amplitude region in Fig. 5.8 is close to the natural frequency of the system in still water. As shown in Fig. 5.9, the frequency ratio is close to unity for $5.9<U^*<7.4$. (iii) Frequency response for the cases with $80°\leq\alpha_{PTC}\leq 100°$ is unique in the sense that the amplitude response is associated with very high f^* at $U^*\cong 14.0$ (Fig. 5.9).

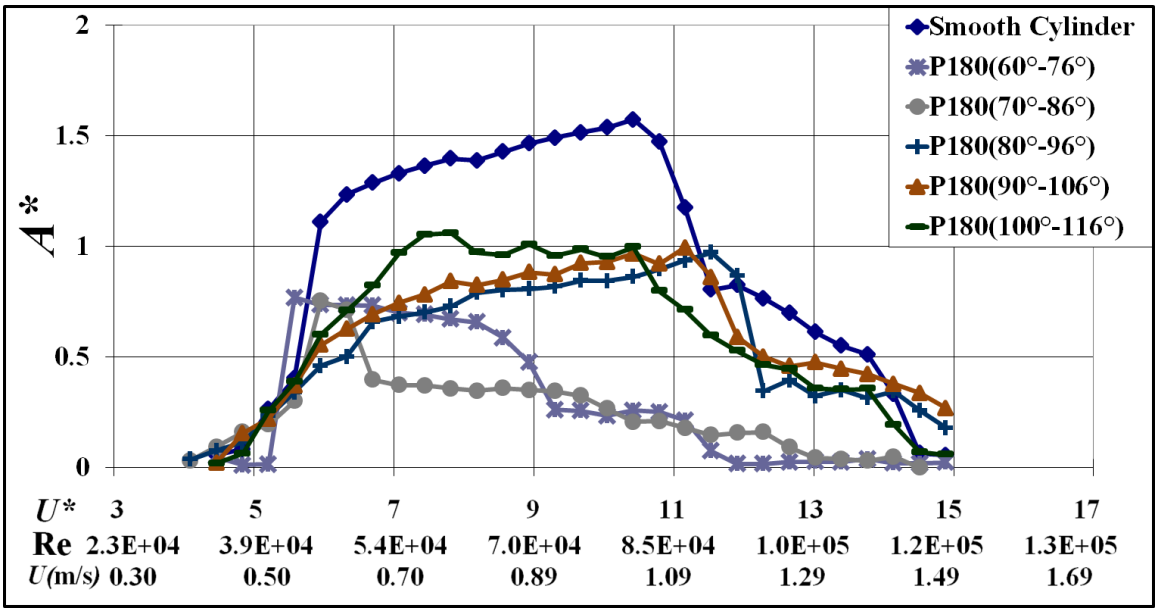

Fig. 5.8. Amplitude response plots for Strong Suppression (SS): P180

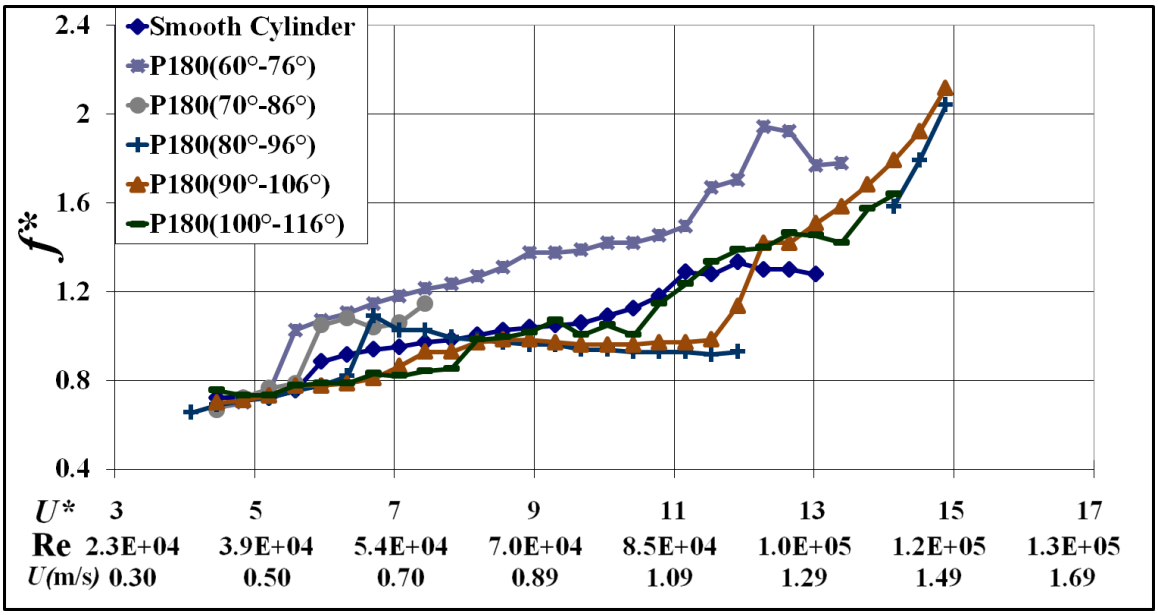

Fig. 5.9. Frequency response plots for Strong Suppression (SS): P180

B. Results for P60 in SS ($62° \leq \alpha_{PTC} \leq 104°$)

Fig. 5.10 shows the amplitude response for a few P60 configurations where strong oscillatory suppression is observed. The following observations can be made: (i) For P60:62°-78°, amplitude drops to negligible levels at $U^*\cong 8.0$ and is nearly fully suppressed for $U^*\geq 11.0$. This is similar to the smoother configuration P180:60°-76°, where small amplitudes persist past $U^*\cong 9.0$ and the cylinder motion is nearly fully suppressed for $U^*\geq 13.0$. For these cases, desynchronization is reached at much lower U^* values than those of the smooth cylinder. (ii) For P60, as the roughness strip moves downstream, there is a gradual transition from very strong suppression with P60:62°-78° to a split upper branch with P60:70°-86° to a broader upper branch with the largest strip placement angles P60:80°-96°, P60:90°-106°, and P60:100°-116°. There is more gradual transition from the upper branch to the lower branch ($10.0<U^*<12.0$) for larger strip angles. For all cases in this strip angle range ($80°\leq\alpha_{PTC}\leq 100°$), lower branch persists up to $U^*\cong 15.0$ with smaller but notable amplitudes even at $U^*=14.0$ with the smaller strip angle location inducing higher amplitudes of oscillation.

Frequency response of strong suppression for P60 is shown in Fig. 5.11. The following observations can be made: (i) For P60:62°-78° and P60:64°-80°, similarly to P180:70°-86°, a single dominant frequency is observed only in the narrow region $5.5\leq U^*\leq 7.8$ (see also Fig. 5.12). This U^* region is closely related to the natural frequency of the system in still water. (ii) For P60:70°-86°, the frequency ratio follows an increasing-decreasing trend in the range $5.5\leq U^*\leq 8.5$, where it is higher than the smooth cylinder oscillation frequency, followed by a step increase to a plateau where frequency remains nearly invariant with U^*. (iii) Same as with P180, at the end of the lower branch the frequency response for the larger strip location angles ($80°\leq\alpha_{PTC}\leq 100°$) is high while

at lower angles and for the smooth cylinder there are no oscillations. The larger the strip placement angle, the higher the frequency of oscillation for U^*>8.5. Particularly for U^*>10.0 frequency ratio keeps increasing and beyond U^*>13.0 cylinder exhibits much higher oscillation frequency compared to the smooth cylinder and even higher than that of P180. Especially oscillation frequency of P60:100°-116° is significantly higher than that of smooth cylinder for U^*>11.0 reaching up to f^*≅2.65. (iv) For P60 and P180, at the onset of the upper branch, there is a frequency jump only for the smooth cylinder and α_{PTC}<80°. For the higher angles in the SS zone (80°≤α_{PTC}≤100°), frequency change is gradual.

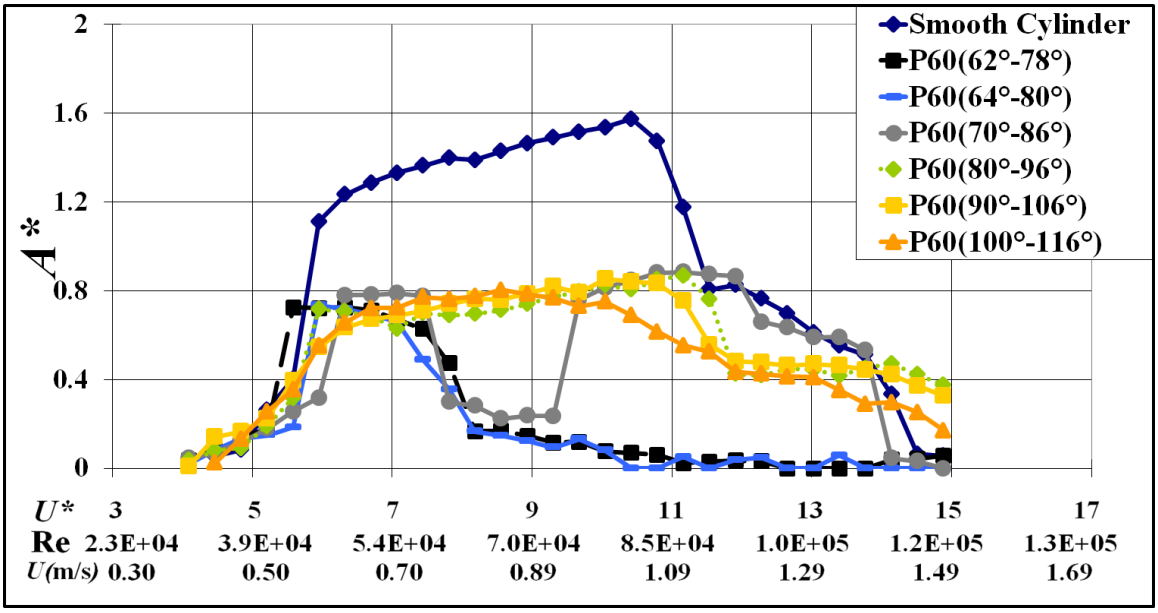

Fig. 5.10. Amplitude response plots for Strong Suppression (SS): P60

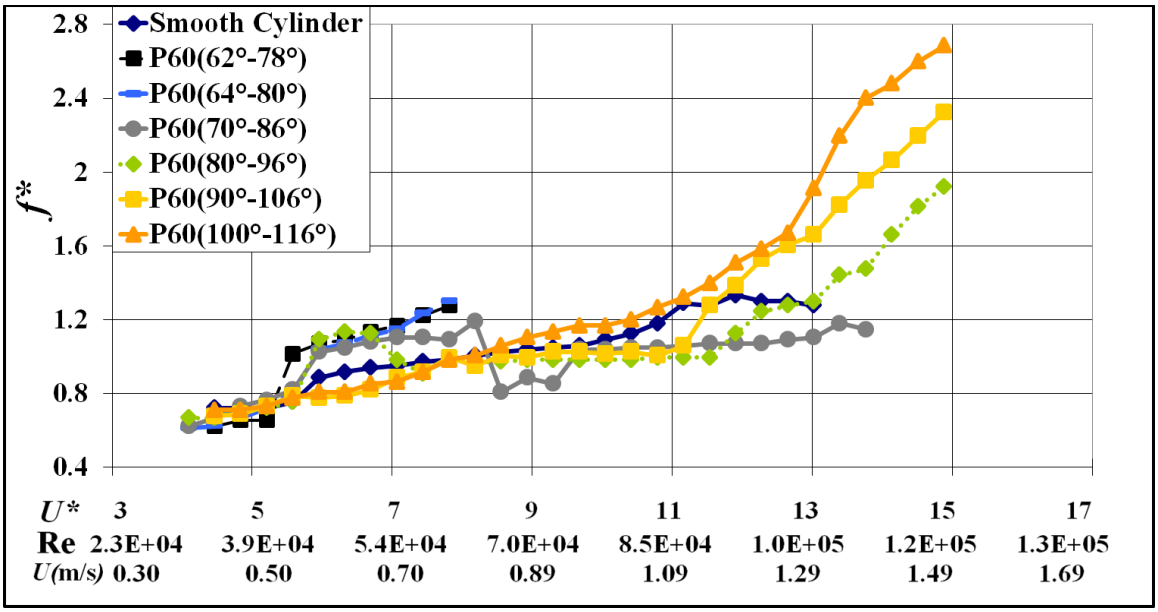

Fig. 5.11. Frequency response plots for Strong Suppression (SS): P60

5.2.2.2. Displacement and power spectrum (P60: 64°-80° and 90°-106°)

Displacement time histories and spectra for three qualitatively different cases are presented in this section.

(i) Strong suppression with narrow synchronization range was observed in three cases: P180:60°-76°, P180:70°-86°, P60:62°-78°, and P60:64°-80°. The latter is selected as example for illustration and results are presented in Figs. 5.12(a)-(e). Figs. 5.12(a)-(b) show the response in the initial branch at U^*=4.84 and U^*=5.6. Corresponding spectra show a dominant frequency spike indicating the oscillation frequency. Fig. 5.12(c) shows the response in the upper branch for U^*=6.32 with A^*=0.73, which extends to U^*=7.2 with A^*=0.68. At higher reduced velocities, oscillations become irregular and insignificant as shown in Figs. 5.12(d)-(e) and corresponding spectra become nearly uniform with no predominant spikes. At even higher reduced velocities, the

characteristics of displacement time histories and spectra are nearly the same and are not presented here.

(ii) Split upper branch is shown for P60:70°-86° in Figs. 5.12(f)-(g). The response in the first peak and in the trough is similar to P60:64°-80° discussed in (i) so it is not presented here. In the second upper branch region at U^*=10.42, the roughness cylinder regains periodic motion and a dominant peak is clearly observed in Fig. 5.12(f). As reduced velocity approaches desynchronization at U^*=14.14, the cylinder displacement becomes negligible and the dominant frequency disappears in Fig. 5.12(g).

(iii) Reduced amplitude along the whole range of reduced velocities with high oscillation frequency at the end of the range occurs for P60 and P180 for $80° \leq \alpha_{PTC} \leq 100°$. Displacement time histories and spectra for P60:90°-106° are shown in Figs. 5.13(a)-(f). For the P60:90°-106° configuration, cylinder oscillation is more regular than the strong suppression case P60:64°-80° and a dominant frequency spike is distinct at U^*=4.84 in Fig. 5.13(a) and at U^*=6.32 in Fig. 5.13(b). As reduced velocity increases, cylinder oscillation becomes less uniform in Figs. 5.13(c)-(d). At U^*=11.53, cylinder motion becomes irregular with less sharp frequency spike in Fig. 5.13(e). At even higher U^*=12.65 in Fig. 5.13(f) and U^*=14.51 in Fig. 5.13(g), however, oscillatory motion regains more regularity with high frequency cylinder motion. Compared to Fig. 5.13(b), Fig. 5.13(g) has smaller amplitude with more modulation. This implies the motion in Fig. 5.13(g) is not synchronized.

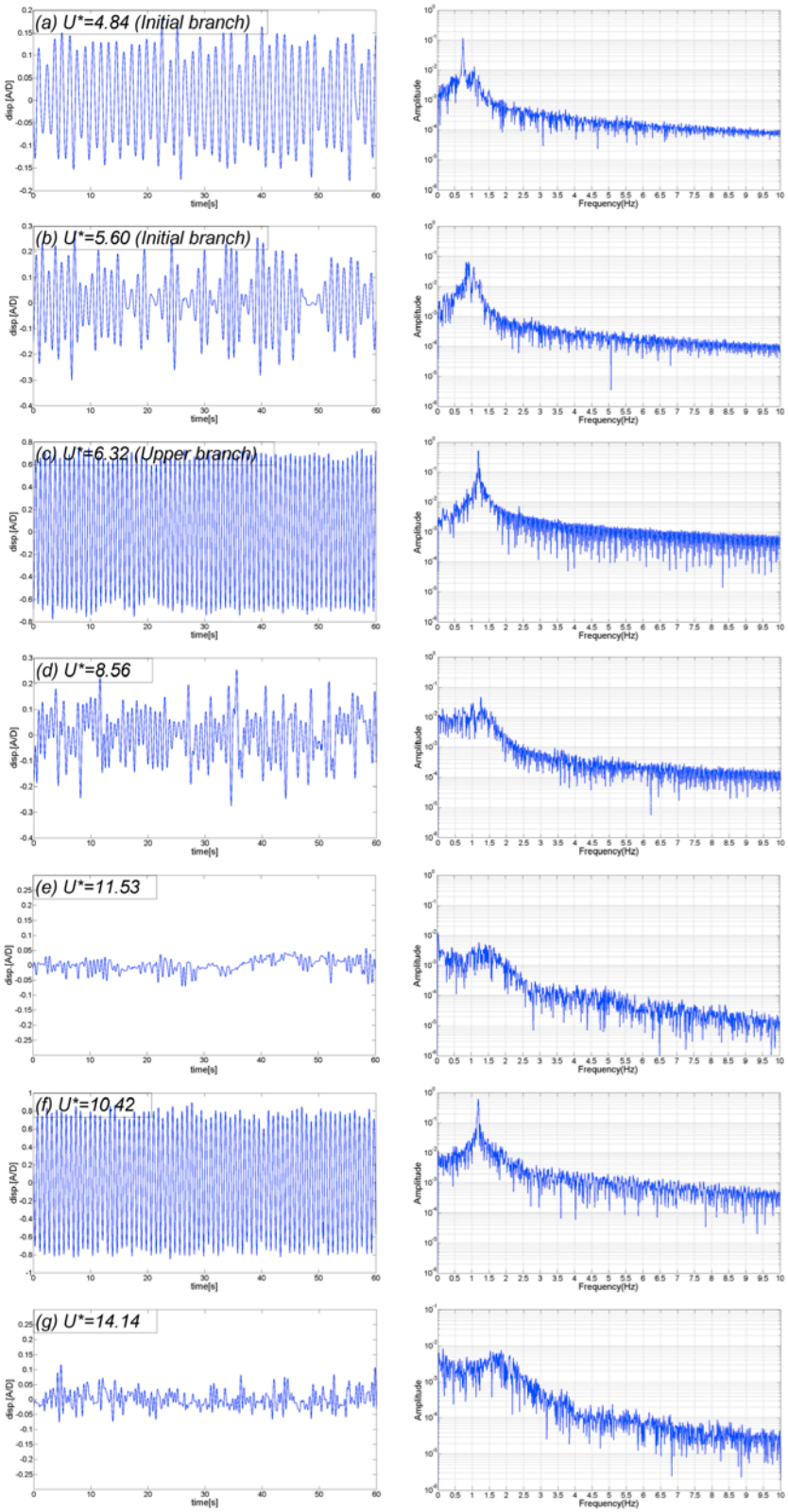

Fig. 5.12. Displacement time series and power spectra for SS (P60:64°-80°)

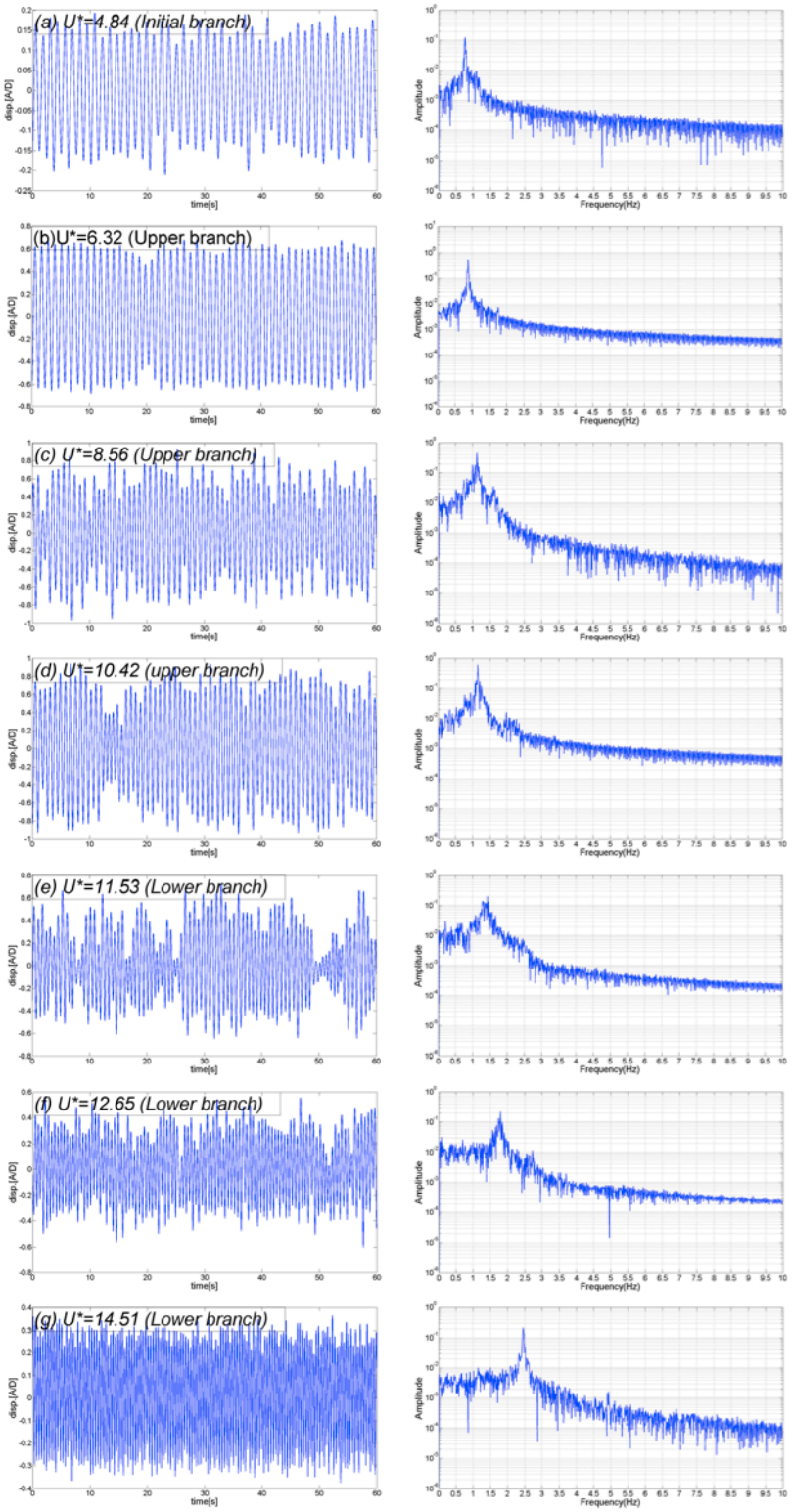

Fig. 5.13. Displacement time series and spectra for SS (P180:90°-106°) (a-g), and (P60:90°-106°) (h)

5.2.3. Calculation of lift coefficient and phase angle for WS zones

C_{total}, ϕ_{total}, C_{vortex}, and ϕ_{vortex} are computed using the inverse dynamics that was carried out for the smooth cylinder in Chapter 3. As shown in Figs. 5.15-5.18, the general trend of C_{total}, ϕ_{total}, C_{vortex}, and ϕ_{vortex} for P180 is similar to that of the smooth cylinder (Figs. 3.15-3.18). The maximum value of C_{total} is found at the beginning of the upper branch (Fig. 5.14) and a major ϕ_{total} jump is observed between upper and lower branches (Fig. 5.15). C_{total} of PTC location at $110° \leq \alpha_{PTC} \leq 130°$ has less sharp peak than all the other PTC locations. Also, for $U^*>11.0$ (after the phase jump), ϕ_{total} has less fluctuation compared to the smooth cylinder. Similarly to the smooth cylinder in the present study, 1st and 2nd maximum peak s of C_{vortex} are found at the upper branch and lower branch respectively. The major ϕ_{vortex} jump is observed between initial and upper branches. For PTC location at $110° \leq \alpha_{PTC} \leq 130°$, ϕ_{vortex} jump starts at higher U^* than other WS cases.

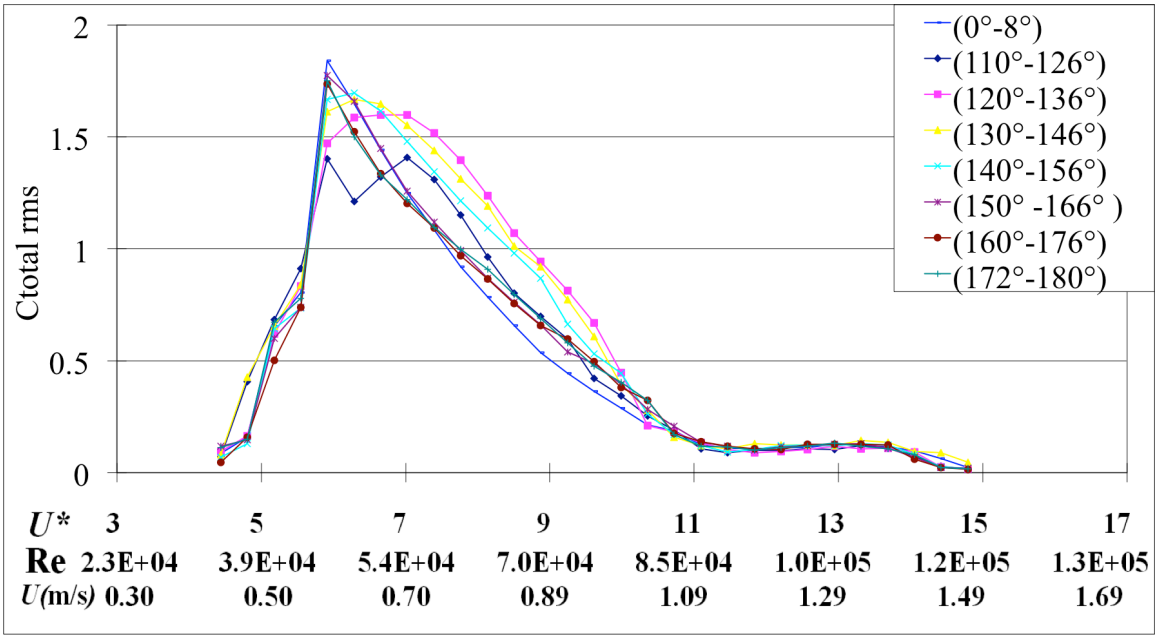

Fig. 5.14. Total transverse coefficient $C_{total\ rms}$ for WS1 and WS2 zones of P180

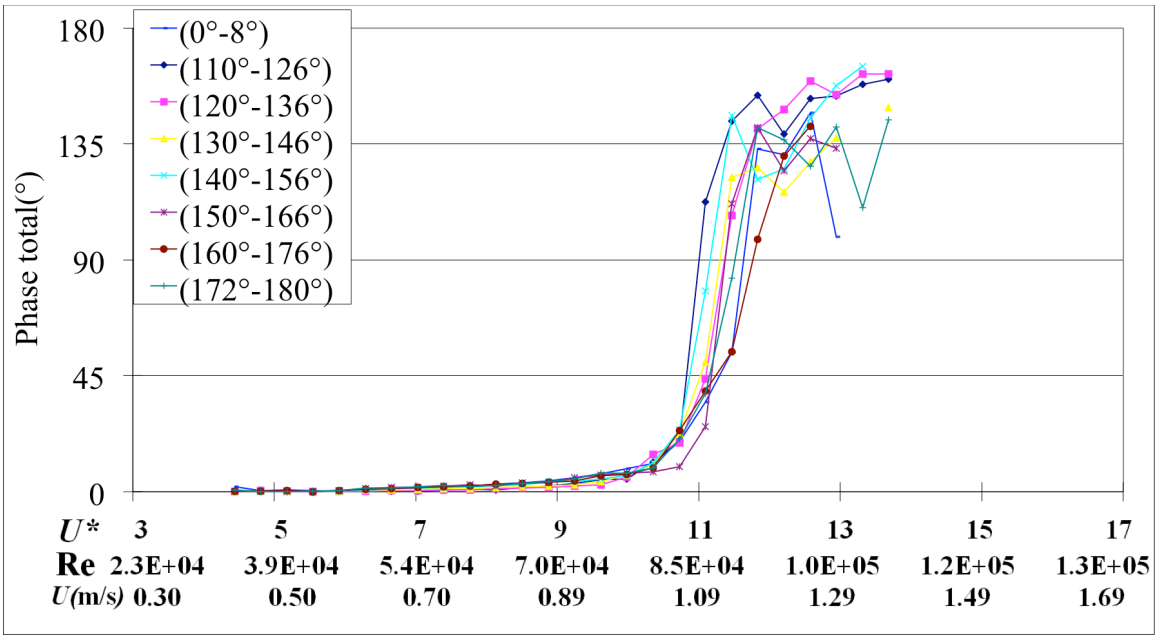

Fig. 5.15. Total phase lag ϕ_{total} for WS1 and WS2 zones of P180

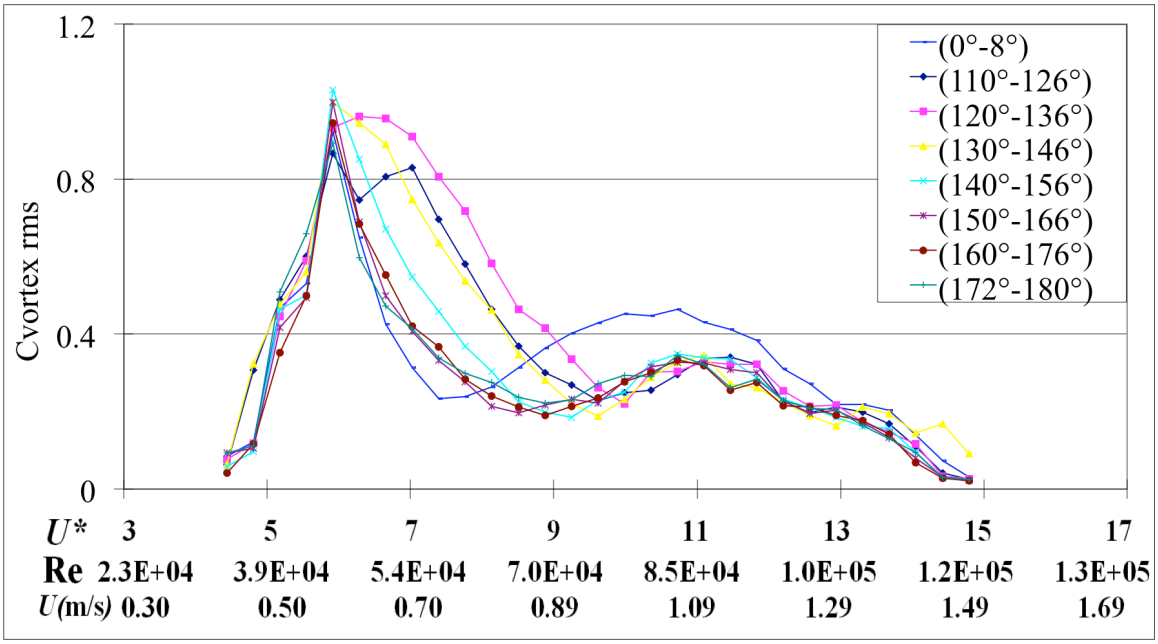

Fig. 5.16. Vortex transverse coefficient $C_{vortex\ rms}$ for WS1 and WS2 zones of P180

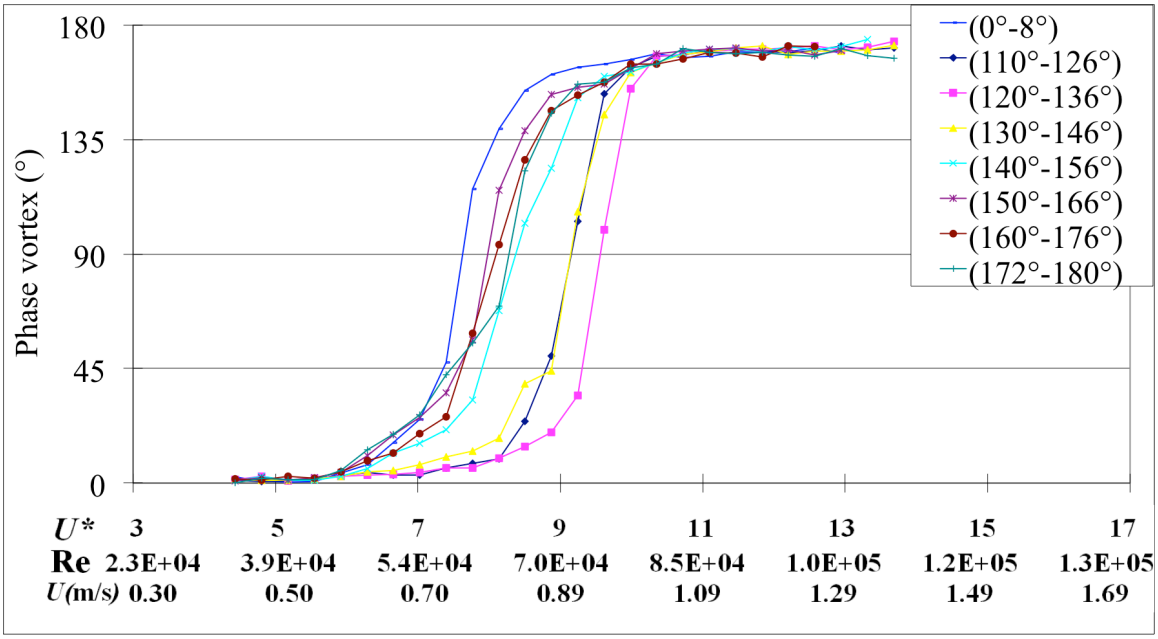

Fig. 5.17. Vortex phase lag ϕ_{vortex} for WS1 and WS2 zones of P180

Similarly to the smooth cylinder and WS cases of P180, C_{total}, ϕ_{total}, C_{vortex}, and ϕ_{vortex} of P60 have similar trends. As shown in Figs. 5.18 and 5.19, C_{total} has maximum peak at the upper branch and the ϕ_{total} jump is found between the upper and lower branches. But at U^*>11.0 ϕ_{total} of P60 has more variation than those of P180. This variation is due to high Reynolds number effect in the present study where the upper branch overtakes most of the lower branch. The latter is short and exhibits desynchronization features. The lower branch in the current study also has desynchronization properties. For C_{vortex}, and ϕ_{vortex}, the maximum peak of C_{vortex} is found at the upper branch and the ϕ_{vortex} jump is observed also between the initial and upper branches. Same as in the case of the smooth cylinder, the jump of ϕ_{total} and ϕ_{vortex} is related to f_{osc} passing through f_N and $f_{N,w,}$ respectively. Since WS1 has higher f^* than that of the smooth cylinder, ϕ_{vortex} of WS1 passes through $f_{N,w}$ at earlier U^* than in the WS2 cases. While WS2 has lower f^* than that

of the smooth cylinder, the ϕ_{vortex} jump of WS2 is delayed compared to that of the smooth cylinder and has variation depending on the PTC location. For ϕ_{total}, the onset of jump has less variation than that of ϕ_{vortex}. This is due to the fact that f^* of the WS1 and WS2 zones increases slowly at high U^* and becomes almost constant.

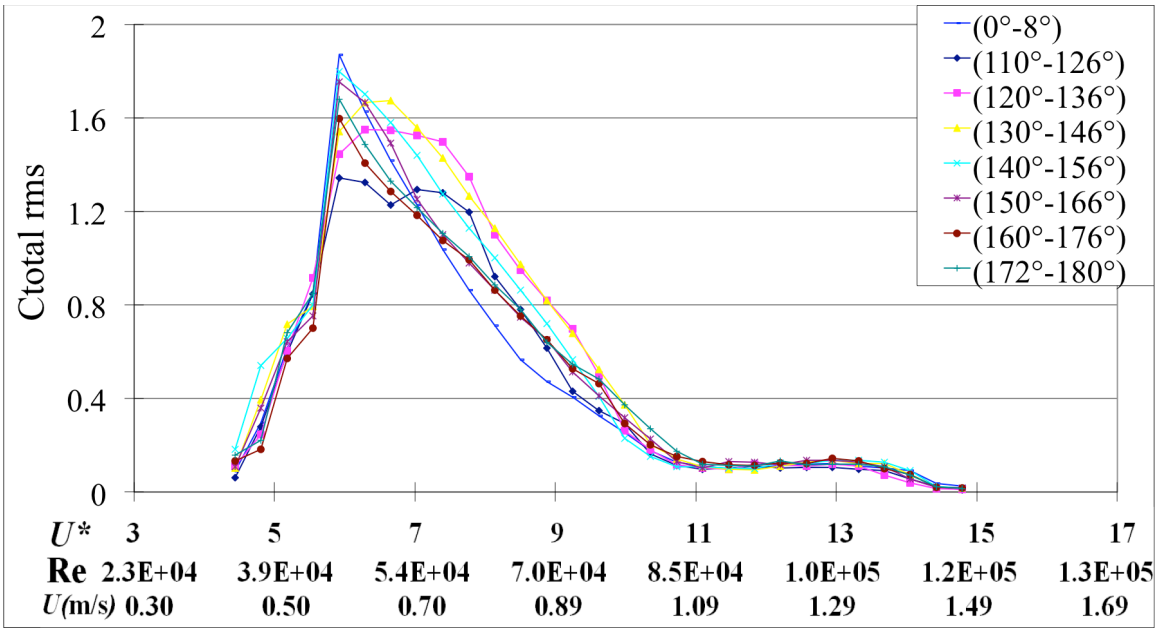

Fig. 5.18. Total transverse coefficient $C_{total\ rms}$ for WS1 and WS2 zones of P60

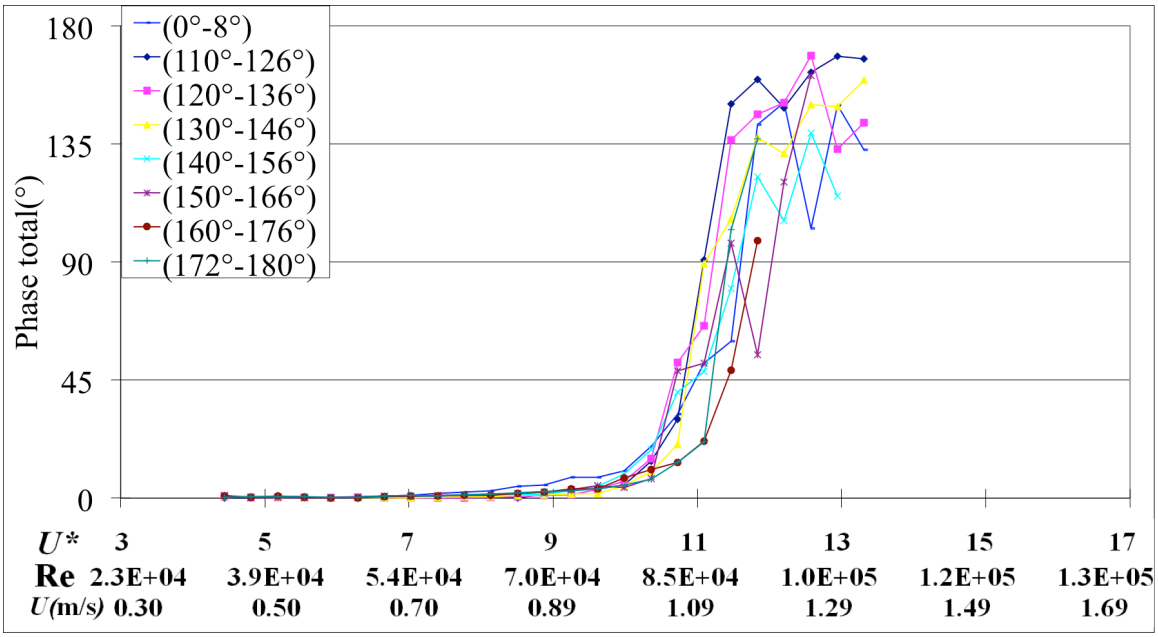

Fig. 5.19. Total phase lag ϕ_{total} for WS1 and WS2 zones of P60

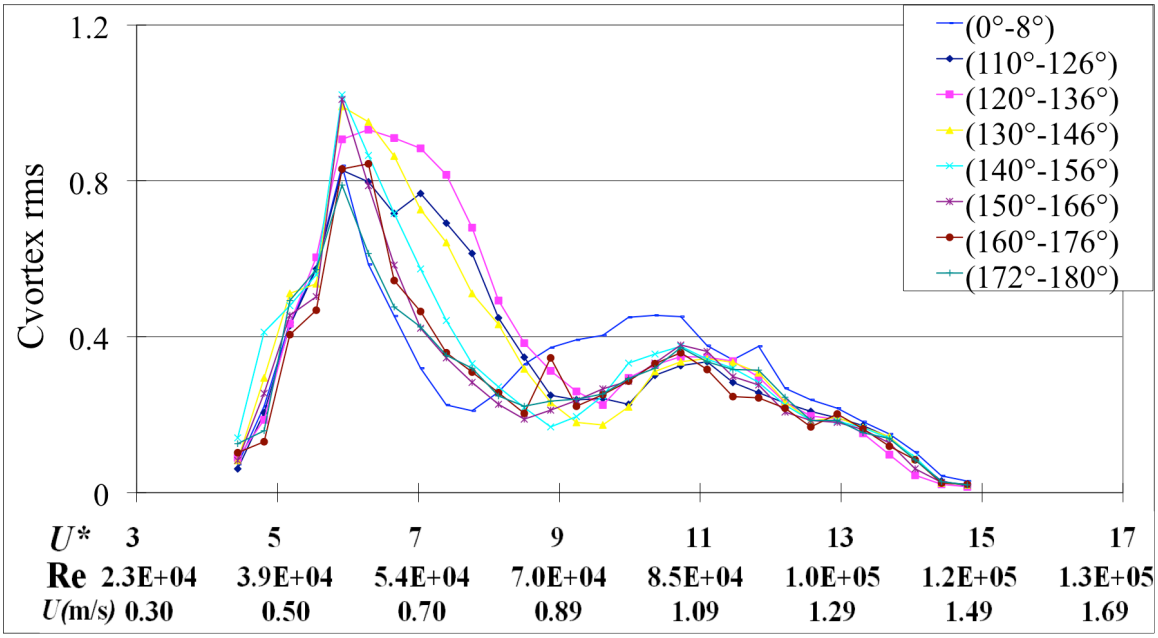

Fig. 5.20. Vortex transverse coefficient $C_{vortex\ rms}$ for WS1 and WS2 zones of P60

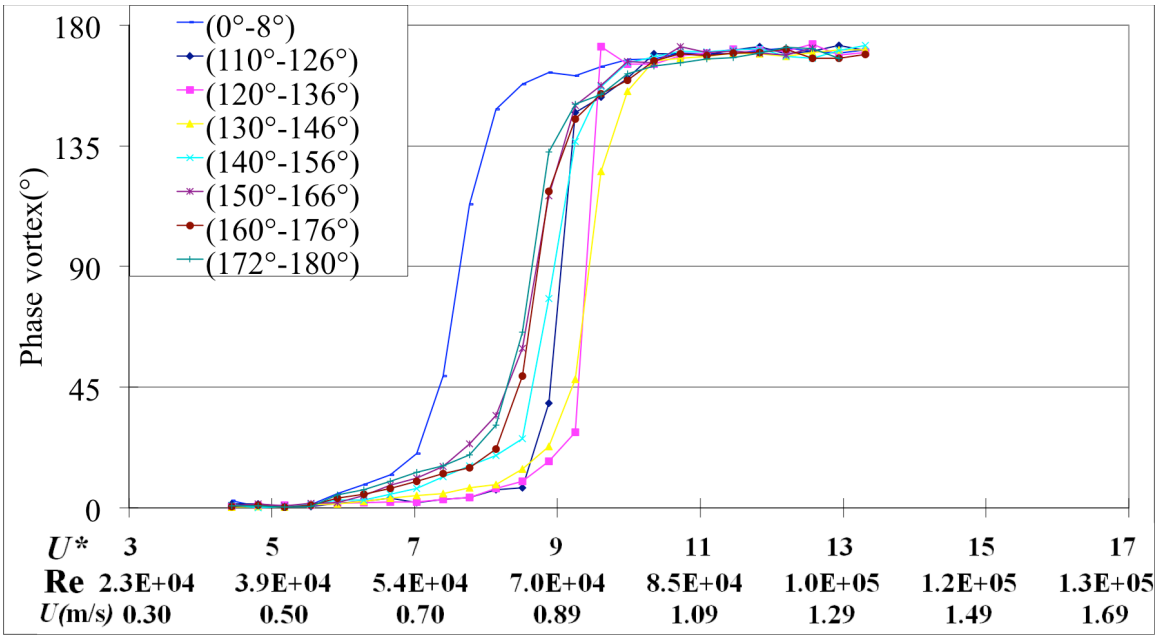

Fig. 5.21. Vortex phase lag ϕ_{vortex} for WS1 and WS2 zones of P60

5.2.4. Hysteresis between initial and upper branches at the SS zone

For the PTC cylinders in the SS zone, hysteresis is observed in amplitude and frequency response between the initial branch and the upper branch. Figs. 5.22 and 5.23 show hysteresis in amplitude and frequency for P180:60°-76°. The rough cylinder response is measured in two ways by changing water speed in forward or backward direction that is by slowly increasing or slowly decreasing the flow speed. As seen in Fig. 5.22, when the flow speed is increased, the oscillation amplitude jump to the upper branch occurs at $U^*\cong5.4$ and the upper branch starts at that point. When the flow speed is decreased from $U^*\cong5.7$, the upper branch extends and persists until $U^*\cong4.9$. Similarly, way in the frequency response (Fig. 5.23), for forward speed increases, the frequency

ratio gradually increases and jumps at $U^* \cong 4.9$. For backward speed decrease, the frequency ratio slowly decreases from 1.2 and drops to 0.8 at $U^* \cong 4.9$.

For hysteresis from the initial branch to the upper branch, forward flow-speed increase shows a 2S mode and backward flow-speed decrease shows 2P mode (vortex mode will be discussed in Section 5.2.5.2). Zdravkovich (1982) first showed, by observing flow visualization that the vortex mode jump was connected to a switch in the timing of vortex shedding. This switch in timing is caused by a competition between two different mechanisms of vortices. The jump mechanism was explained by Williamson and Roshko (1988). This transition from 2S to 2P mode is also associated with a jump in vortex phase as the response frequency passes through the value $f=f_{n,medium}$ (natural frequency in the fluid medium: water). (Williamson & Govardhan 2004).

Force measurement was not possible in this study, that is, the lift force could not be measured. Instead, the lift force was calculated from the time history of the displacement using equation (3.1). Using equations (3.9) and (3.16) the lift force and phase angle hysteresis can also be demonstrated as shown in Figs. 5.24 and 5.25. This jump is attributed to change of the vortex shedding mode. Visualization results in Section 5.2.5.2 also shows that this study also have the same change of vortex shedding mode and thereafter it is inferred that hysteresis in the phase angle is expected.

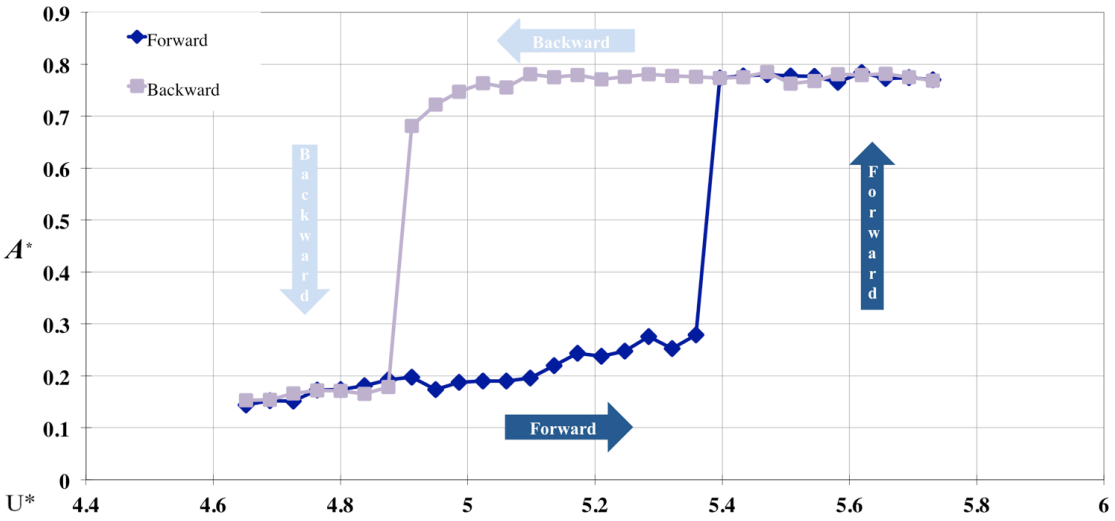

Fig. 5.22. Hysteresis in amplitude response : P180:60°-76°

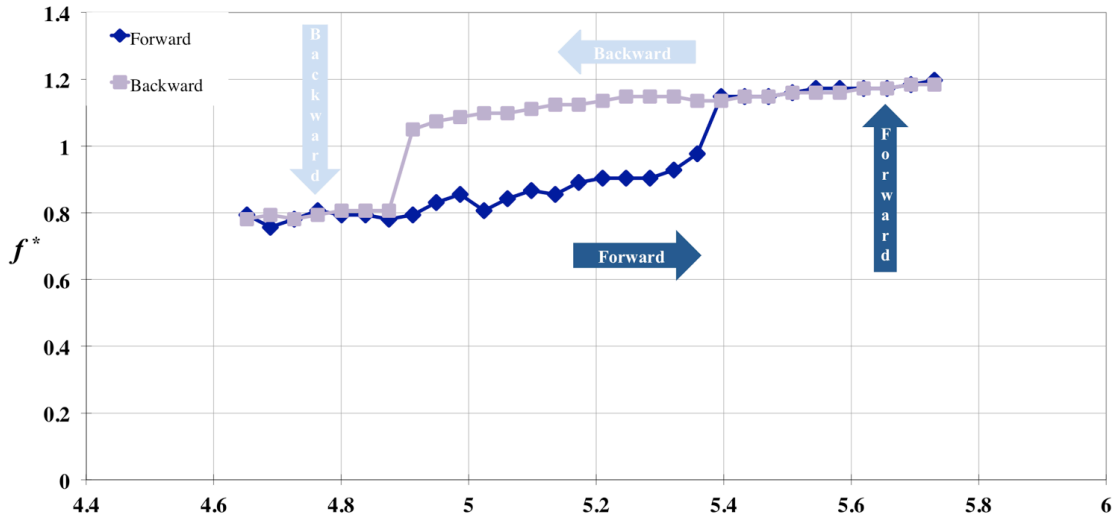

Fig. 5.23. Hysteresis in frequency response : P180:60°-76°

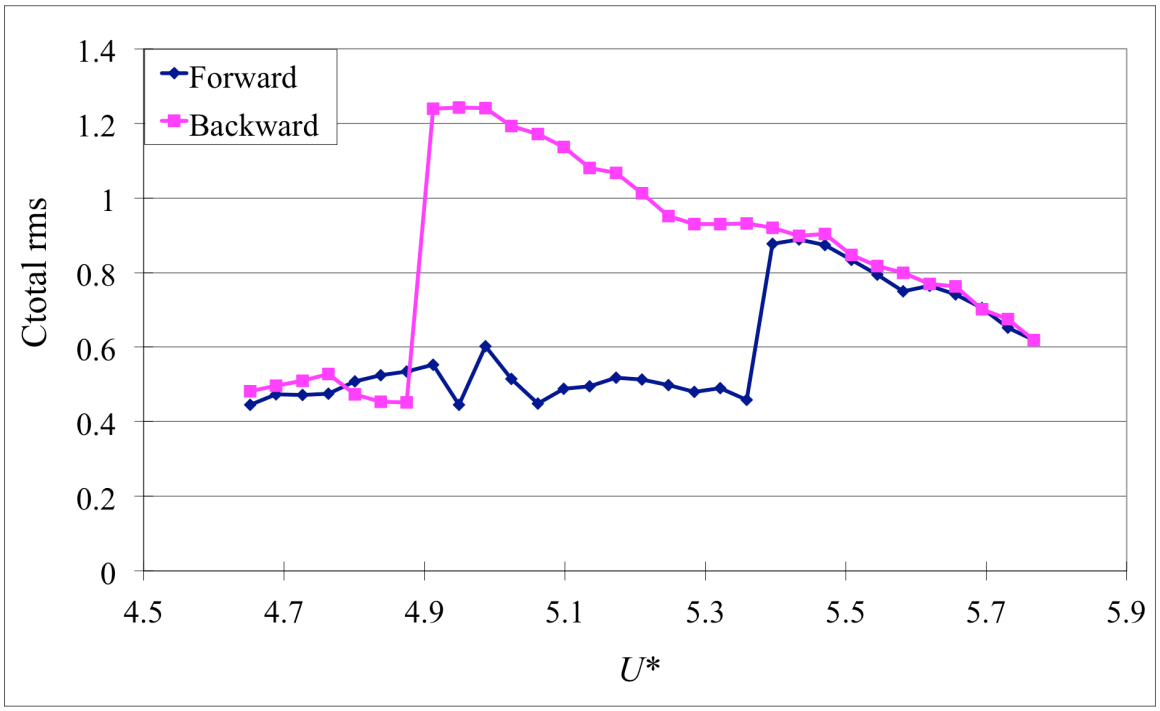

Fig. 5.24. Total transverse coefficient $C_{total\ rms}$: P180:60°-76°

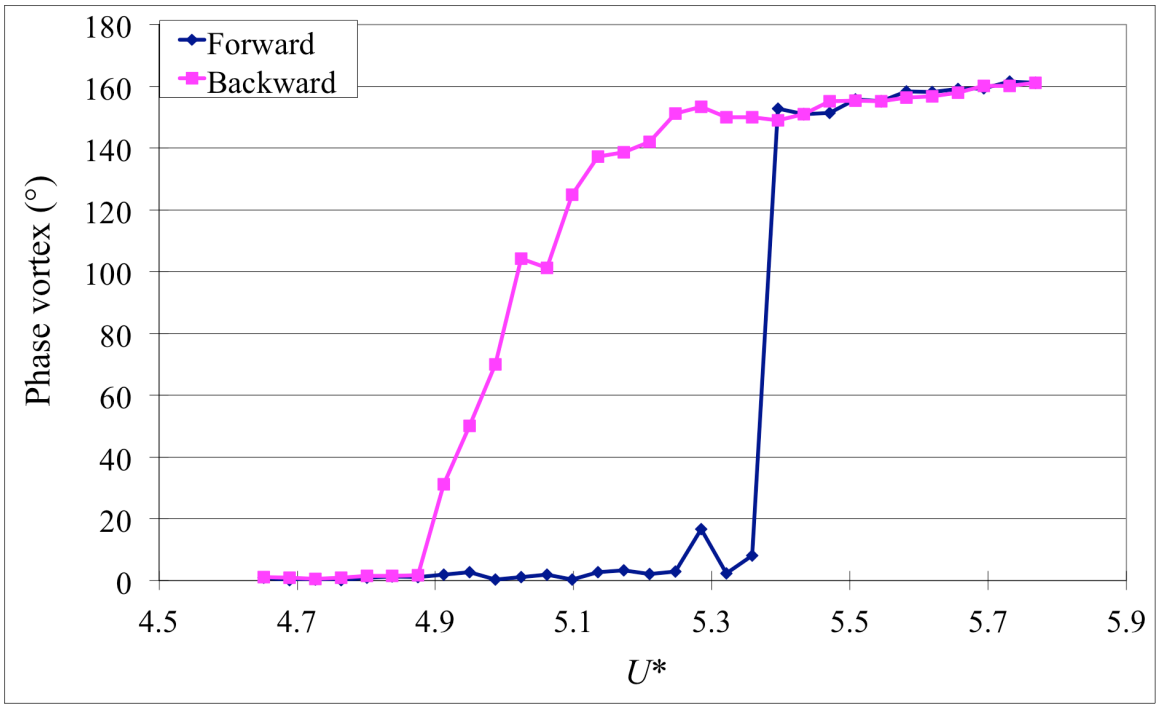

Fig. 5.25. Vortex phase lag ϕ_{vortex} : P180:60°-76°

The hysteresis in Fig. 5.22 is related to a "subcritical Hopf bifurcation" (Strogatz 2001; Chang 2004). For subcritical the Hopf bifurcation shown in Fig. 5.26, when a control parameter $\mu<0$, one stable and one unstable limit cycles exist. When the initial position is inside the boundary of the unstable limit cycle (dashed circle), the trajectory would converge to the stable origin. When the initial position is outside of the boundary of the unstable limit cycle, the trajectory would converge to the stable limit cycle. As the control parameter μ increases, the unstable limit cycle boundary (dashed circle), disappears and all solutions converge to the new stable limit cycle. This phenomenon can be also seen in the SS zone and bifurcation of the present case is shown in Fig. 5.27.

The unstable branch in Fig. 5.27 is found from the average of two thresholds; the lowest value that causes the cylinder jump and the highest value that does not cause cylinder jump. When a threshold amplitude is forced at any point in the range $4.9<U^*<5.3$, the cylinder response jumps to the upper branch. A minimum threshold amplitude is required to cause jump to another stable branch and less than minimum threshold amplitude is not able to induce shift to another equilibrium point. This phenomenon is the same as the hard galloping discussed in Chapter 4.

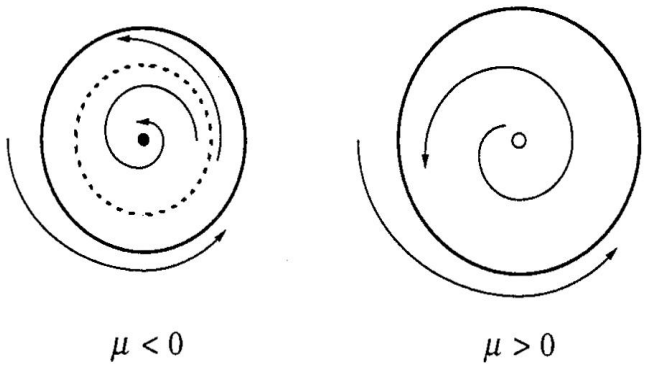

Fig. 5.26. Phase portrait of subcritical hopf bifurcation (Stogatz)

Fig. 5.28 shows the bifurcation of a rotating Coutte-Taylor flow as changing angular velocity of the inner cylinder with imperfection. From similar bifurcation type, we can infer that hard galloping is due to the system imperfection caused by a boundary, a free surface effect, and so on. The bifurcation obtained from the experiments matches very well with Fig. 5.28 except for the bifurcation points. Bifurcation points are very sensitive and small disturbances can change the response. Even though only one control parameter (velocity of water) is changed in the tests, it may change the other factors (height of water, turbulence intensity, velocity gradient) too. Even the flow may not be steady state during the change of the water velocity. This presents a challenge in finding the exact bifurcation point. Hysteresis in a rough cylinder has been rarely reported so far and this may be the first study of hysteresis in a rough cylinder.

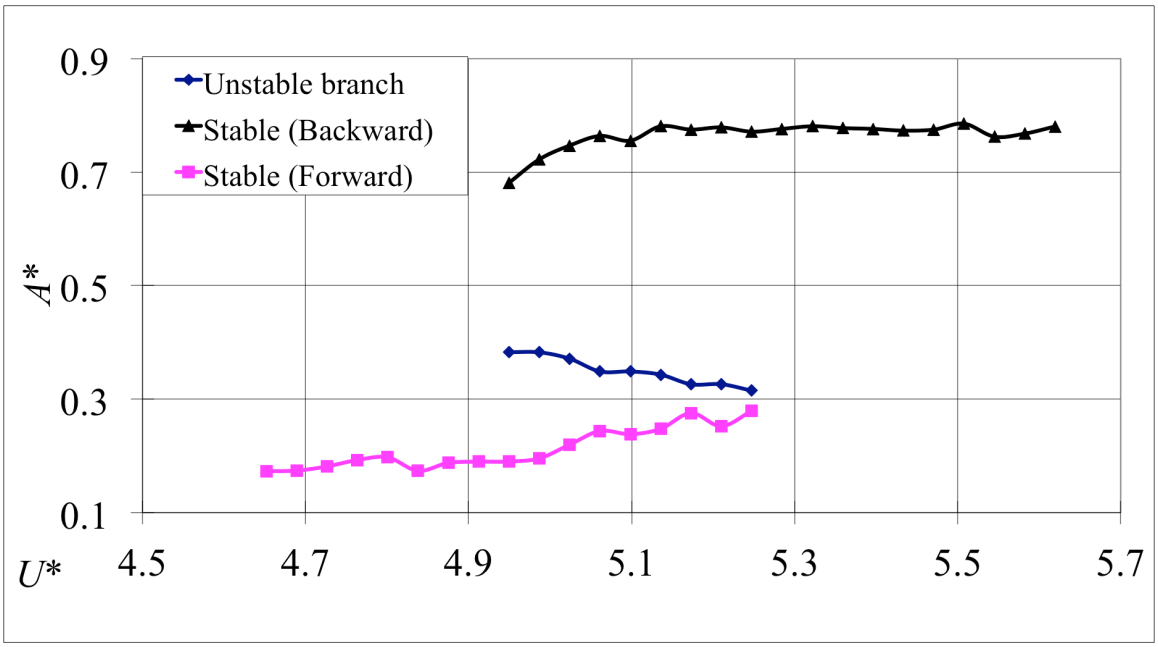

Fig. 5.27. Bifurcation of SS for P180:60°-76°

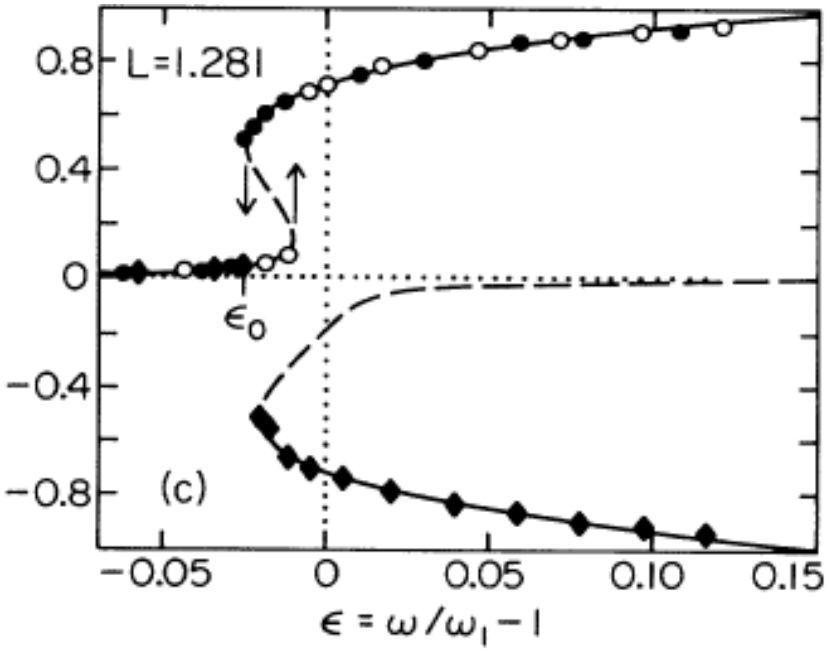

Fig. 5.28. Bifurcation in rotating Couette-Taylor flow (Aitta 1985)

5.2.5. Wake vortex structure

5.2.5.1. Weak suppression

The flow field around the PTC cylinder in the weak suppression zones (both WS1 and WS2) is also studied. It is found that, the wake structures in the initial, upper and lower branches are remarkably similar to those of a smooth cylinder but with weaker (less circulation) and smaller (in core size) vortices. Additionally, the vortex formation length (l_f) is longer in the case of WS compared to that of the smooth cylinder, where l_f is the distance between the vortex center at the moment of shedding and the cylinder center. This has been specifically verified for the WS1 case with configuration P180:0°-8°. For this configuration, at U^*=10.7, where the amplitude difference between the WS1 and

smooth cylinder is maximum, l_f is about 7.5% higher than that of the smooth cylinder at bottom dead center (BDC) location.

For WS2, a typical wake structure of the configuration P180:140°-156° at U^*=10.42 is also examined. Similar characteristics as those in WS1 are observed, i.e., weaker vortices constituting the wake with marginally longer l_f compared to a smooth cylinder at identical reduced velocity values. This agrees with the observation by Lee & Kim (1997) that surface protrusion increases the vortex formation length of a circular cylinder.

5.2.5.2. Strong suppression

Wake vortex structures in strong suppression using configuration P60:64°-80° are discussed in this section. In Fig. 5.10, in the initial branch (U^*≅5.7), the 2S mode of shedding is found but with l_f increased by about 64% compared to the smooth cylinder. At U^*≅6.48 corresponding to the upper branch, the 2P mode of shedding appears in the near-wake with vortex size to diameter ratio being notably smaller than that of the smooth cylinder at the same U^* value. At 8.0<U^*<9.5, which falls in the higher suppression region, no regular shedding is observed. Also, the wake is tapering in the downstream direction with its width substantially reduced. During most of the cycle, the wake is comprised of two weaker (less circulation) attached vortices similar to what is shown in Fig. 3.25(a), (i.e., in a totally different case – that of smooth cylinder desynchronization). At U^*>9.5 where the cylinder motion is negligible, sometimes two weak (less circulation) symmetric vortices are observed (Fig. 3.25(a)) but most of the

generated vorticity from the shear layers diffuses in the wake in the form of irregular, small-scale eddies (Fig. 3.25(b)).

A closer inspection revealed that shear layers fail to achieve proper roll up. According to Gerrad (1966), this possibility of symmetric vortex configuration is possible only at a Reynolds number of the order of 10^3. In the range of Re considered in this paper, this phenomenon is observed both in smooth cylinder desynchronization and in PTC cylinder strong suppression. In these cases, most of the times, the wake is made up of two weak (less circulation) attached vortices and irregular small scale eddies as seen in Fig. 3.25. Gerrad (1966) too pointed out that such symmetric vortex configurations would lead to a drop of lift, which is in agreement with the suppression results in the strong suppression zone.

For the configuration P60:90°-106°, at $U^*\cong5.7$, 6.48 and 8.39, the 2S mode of shedding is observed but with smaller vortex size to cylinder diameter ratio than in the smooth cylinder case. At $U^*\cong10.68$, apart from the 2S mode, irregular symmetric vortex formation is also observed many times. At still higher reduced velocitiy $U^*\cong14.87$, symmetric vortex formation becomes the predominant wake structure with occasional 2S shedding mode. Substantial reduction in the wake width and downstream extent of the wake is observed. Symmetric vortex formation is thought to be due to intermittent, non-uniform re-attachment of the shear layers (Higuchi et al. 1989).

5.3. MAIN FINDINGS

In the WS1 and WS2 zones, amplitude and frequency response similar to those of a smooth cylinder are observed. Combining the results of P180 and P60, we can draw the following conclusions.

(i) The onset of the initial and upper branches in the smooth cylinder and in the PTC cylinder for the WS1 and WS2 zones - for both P180 and P60 - occur at the same U^*. For both P180 and P60, WS1 has higher f^*, and WS2 has lower f^*, than that of the smooth cylinder for $6<U^*<10.7$ (upper branch of WS). In this range for WS2, higher strip angles result in higher frequency ratio.

(ii) For all WS1 cases, since the strip location is close to the front stagnation point, the flow separated at the upstream edge of the strip would reattach and stabilize as the boundary layer develops again on the cylinder surface as typically shown for a surface protrusion by Nebres & Batill (1993). Due to reattachment, the boundary layer is more diffused (thicker) due to interaction with the roughness elements leading to a marginal increase in the vortex formation length as observed in the flow visualization in section 5.2.5.1.

(iii) For WS2, since the attached roughness is inside the base region of the cylinder, the boundary layer is not significantly disturbed. Instead, the roll up of the shear layers is adversely affected leading to the formation of weaker (less circulation) and disorganized vortices, as shown in the visualization study in Section 5.2.5.1. Hence, both these aspects, i.e., diffusion of boundary layer and improper shear layer roll up, lead to similar response characterized by a drop in excitation amplitude.

(iv) For WS1 and WS2, wake vortex structures similar to those of the smooth cylinder are observed with smaller (in core size) vortices and longer vortex formation length than those of the smooth cylinder.

From the results presented in this chapter we can draw the following conclusions on strong suppression:

(v) For strip angle location in the SS zone at $\alpha_{PTC} \leq 70°$, the upper branch region is narrow and the desynchronization region starts at earlier U^* compared to the smooth cylinder. The f^* in the narrow upper branch region is close to one, that is f_{osc} is close to the natural frequency of the system in still water. No dominant f_{osc} peak is observed in the desynchronization region.

(vi) For higher strip angle location ($80° \leq \alpha_{PTC} \leq 100°$) in the SS zone, amplitude increases gradually in the initial branch and the corresponding frequency also increases gradually. The upper branch extends to $U^* \cong 11.3$. In the lower branch, the frequency ratio increases as high as $f^* \cong 2.7$ with $A^* \cong 0.2$ but that is associated with lack of a predominant frequency.

(vii) At $\alpha_{PTC} = 70°$, that is between the two previous cases, for P60:70°-86°, a transition occurs and the A^* graph exhibits two high amplitude regions (Fig. 5.10).

(viii) In strong suppression, 2S and 2P vortex structures with 64% longer vortex formation length and smaller (in core size) vortices compared to the smooth cylinder are observed in the initial and upper branches, respectively. After the

upper branch, similarly to the desynchronizaton of the smooth cylinder, two symmetric vortices or small eddies are observed in the wake vortex structure.

CHAPTER 6

MAP OF PTC-TO-FIM

6.1. MAP OF PTC-TO-FIM

Based on the results obtained in Chapters 4-5, the response of the cylinder is classified with respect to the circumferential location of the PTC. This classification has lead to the construction of the response map of selective roughness-induced FIM, hereafter called ***"PTC-to-FIM Map"***. For two roughness configurations modeled by commercial sand paper P180 and P60 the maps are shown in Figs. 6.1(a)-(b), respectively. For both P180 and P60 strips, the maps are similar with zonal classification of response in the order WS1, HG1, SG, HG2, SS, and WS2 in the clockwise direction starting from the front stagnation point. The numbers in the Map indicate the range of each zone; e.g., SG 40° in Fig. 6.1(a) indicates soft galloping response when the leading edge of the roughness strip (α_{PTC}) is located anywhere in the range $16° \leq \alpha_{PTC} < 56°$. The map is constructed by systematic change of the roughness strip location in 2° intervals. The robustness of the ***PTC-to-FIM Map*** is discussed in Section 6.3.

From the results shown in Fig. 6.1, the motions of the cylinder heavily depend on the location of PTC. The location of PTC has a significant influence on the boundary layer

transition, separation, and reattachment. Nebris & Batill (1993) used small size of perturbation and defined the different flow regimes as a function of the perturbation angular position as shown in Fig. 6.2.

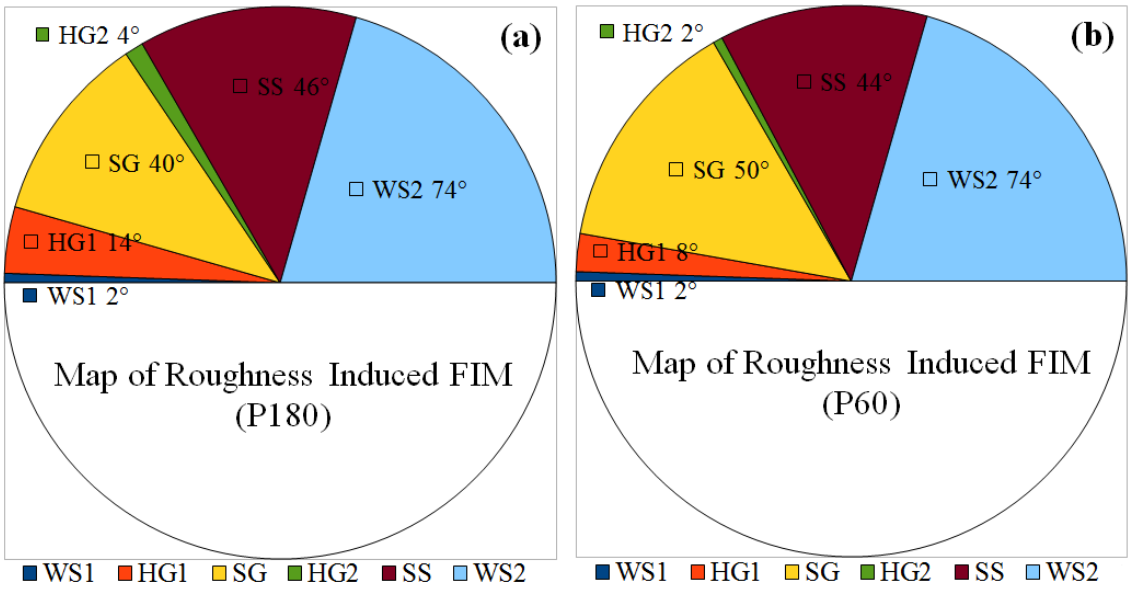

Fig. 6.1. Map of FIM (a) P180 and (b) P60

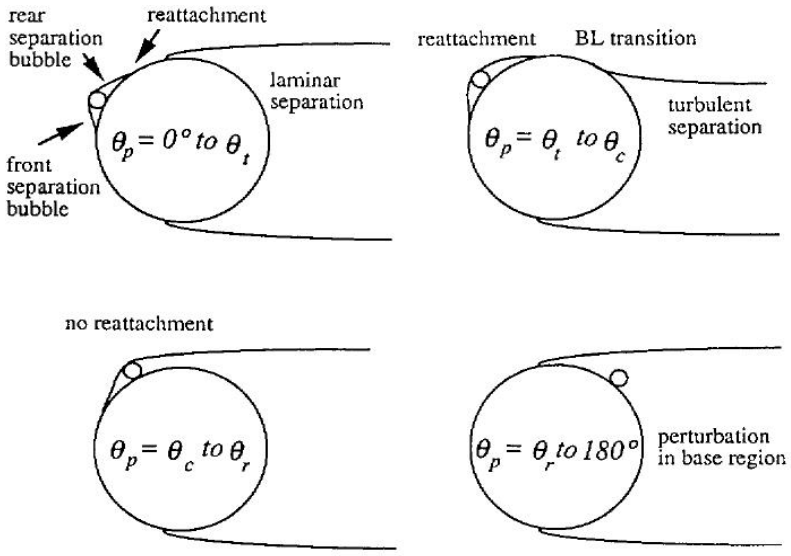

Fig. 6.2. Different flow regimes as function of the perturbation angular position (θ_p): Nebris & Batill (1993)

J.Nebres defines the θ_c (critical angular position where Strouhal number drops steeply) and θ_r (angular position where Strouhal number recovers from drop) based on the change of Strouhal number. Interestingly, angles of θ_c and θ_r are similar to the starting location of the strong suppression and the weak suppression zone, respectively. As shown in Figs. 6.3- 6.4, galloping and suppression can be explained by his measured lift coefficient and drag coefficient data depending on perturbation location.

For galloping, negative hydrodynamic damping caused by big drop of drag coefficient is necessary. Before the angle of θ_c, the drag coefficient is dropping very steeply and the lift coefficient has its highest value than in any other perturbation position. This high lift coefficient can explain the high amplitude motion in galloping. Thus, galloping of a circular cylinder with PTC may be caused by reattachment of flow. Assuming that galloping is mainly attributed to the flow reattachment, a few more things can be explained. For soft and hard galloping, VIV regions have less amplitude compared to that of a smooth cylinder. Higuchi et al. (1989) reported that reattachment of flow decreases the drag coefficient significantly and weakens the vortex shedding. Even asymmetric reattachment can cause substantial lift forces. In the present study, an angle of attack causes unsteady asymmetric reattachment of the cylinder boundary layers.

For angles between θ_c and θ_r, the drag coefficient becomes very high and the lift coefficient becomes very low. This fact reasonably explains the strong suppression zone. Furthermore, as shown in Fig. 6.2, flow characteristic of strong suppression and weak

suppression zones may be attributed to the no-reattachment of flow and perturbation in base region, respectively. In addition, perturbation at the forward stagnation position, which is the same location as WS1, has similar drag and lift coefficient of that of a smooth cylinder.

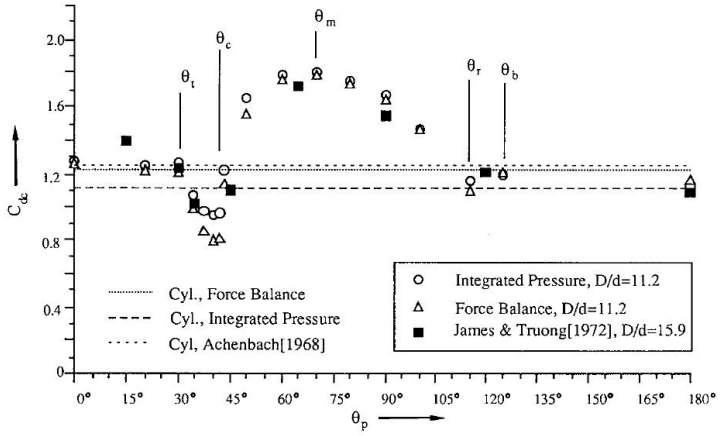

Fig. 6.3. Drag coefficient with perturbation angular position: Nebris & Batill (1993)

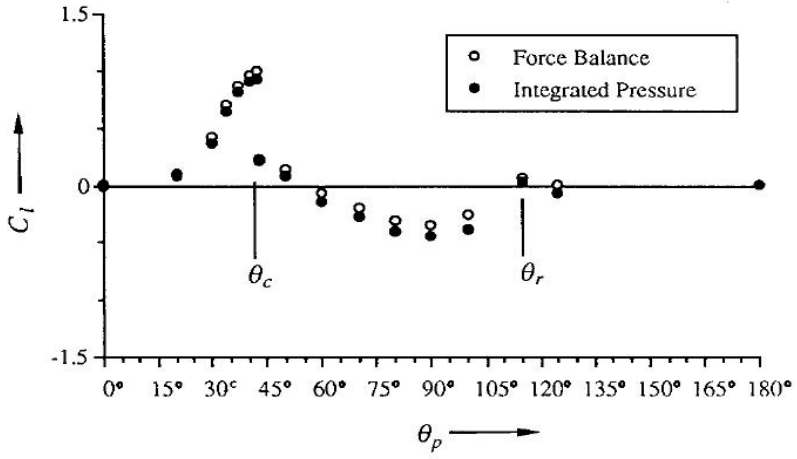

Fig. 6.4. Lift coefficient with perturbation angular position: Nebris & Batill (1993)

6.2. ZONE ROBUSTNESS

In order to confirm the effect of circumferential location of the roughness strips, further experiments are conducted using narrower strips (0.25"=0.635cm covering 8°; Figs. 6.5-6.8), wider strips (1"=2.54cm covering 32°; Figs. 6.9-6.10), staggered configuration (Figs. 6.11-6.12), and two-zone coverage (Figs. 6.13-6.14). The experiments performed in this section are not exhaustive of the ranges of the involved parameters but are selected to place PTC entirely inside a zone or over boundaries between zones to cover more than one zone.

6.2.1. Narrower PTC Strips

6.2.1.1. Results for P180

For the P180 passive turbulence control strip, the narrower strip is placed inside zones WS1, HG1, SG, and SS and the results are shown in Figs. 6.5-6.6.

WS1 zone: In WS1 with the center of the strip at 0° (i.e., at the front stagnation point), the amplitude profile in Fig. 6.5 is observed to follow closely the smooth cylinder but with reduced amplitude of oscillation in the range $8.5 \leq U^* \leq 11.5$ indicating weak suppression, similarly to what was observed with the 16° strip coverage in Fig. 5.2. This further confirms the influence of WS1. Same as P180 and P60 in Fig. 5.3 and 5.5, oscillation frequency values are higher than those for the smooth cylinder in the upper branch ($6.0 \leq U^* \leq 11.3$) of P180: 0°-4°.

HG1 zone: As Fig. 6.5 shows, when the strip is placed inside the HG1 zone (P180:4°-12°), the cylinder goes to hard galloping at $U^*\cong 14.8$ with similar trend and magnitude of oscillation for 16° PTC coverage (Fig. 4.2). The frequency features (Fig. 6.6) are similar to those of P180:2°-18° (Fig. 4.3) with the sharp decline of oscillation frequency at $U^*\cong 14.8$ instead of $U^*\cong 14.5$ (onset of galloping).

SG1 zone: In SG, for P180:30°-38°, the cylinder is in soft galloping for $U^*\geq 13.0$ (Fig. 6.5) which is identical to the case with the strip covering 16° (Fig. 4.8). In both cases, frequency response starts dropping off (Figs, 4.9 and 6.6) prior to the onset of galloping. In galloping, f^* approaches unity.

SS zone: In SS for P180:60°-68°, hard galloping commences at $U^*\cong 14.5$ (Fig. 6.5). This means that the P180:60°-76° configuration, which induced strong suppression in Fig. 5.8, actually covers both the HG2 and SS zones and strong suppression dominated the cylinder motion. As seen in Fig. 6.6, similarly to the 16° PTC coverage in Fig. 4.3, HG2 has higher frequency ratio than HG1. In both HG zones the frequency ratio approaches unity when hard galloping is initiated. To separate the two effects of hard galloping and strong suppression, experiments are conducted with the 8°(0.25")-strip covering separately the 60°-68° and 68°-76° ranges. The former resulted in hard galloping and the latter in suppression. These refining experiments show the level of sensitivity of the zone boundaries in the *PTC-to-FIM Map* in Fig. 6.1(a). For further downstream strip edge location (P180:68°-76°), strong suppression is observed (Fig. 6.5). At $U^*\geq 9.7$, the amplitude of the PTC-cylinder is insignificant.

From these results, we can conclude that the amplitude and frequency response for the 8° coverage strip and the 16° coverage strip are similar if the roughness is located inside a specified zone, that is not covering multiple zones.

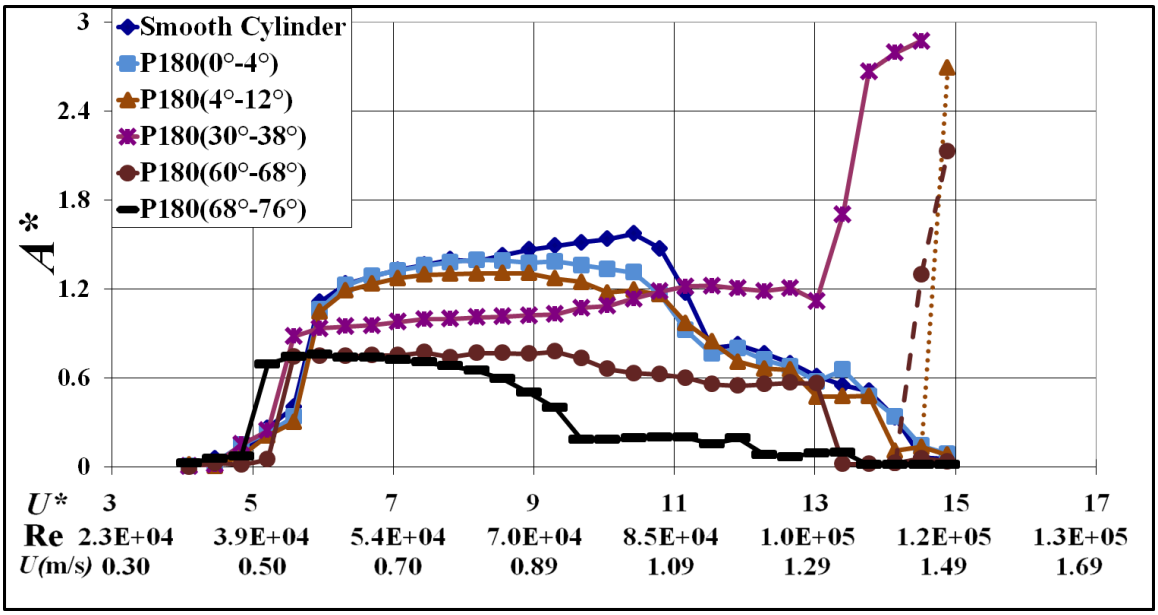

Fig. 6.5. Amplitude response plot for half width with strip P180

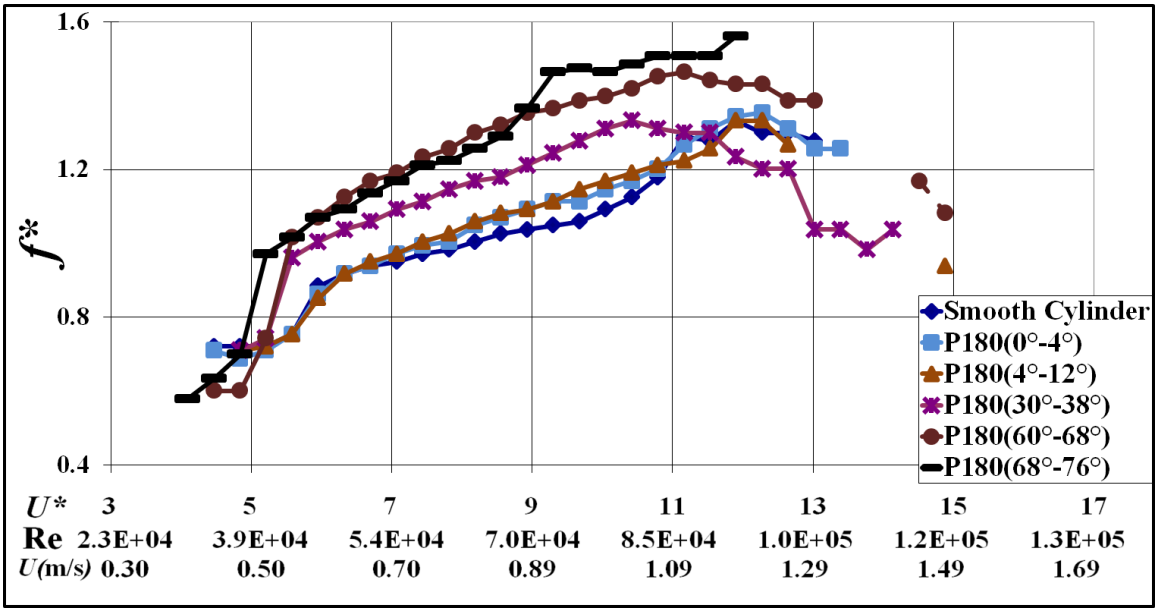

Fig. 6.6. Frequency response plot for half width with strip P180

6.2.1.2. Results for P60

In two cases with P60, namely P60:60°-76° (Section 4.1.1.1, Fig. 4.4) and P60:58°-74° (Section 4.2.2.1, Fig. 4.10), results were different from the general trend and are further investigated here using the smaller coverage strip. Specifically, the former exhibited low amplitude in hard galloping and the latter showed low amplitude and much delayed (higher reduced velocity) onset of soft galloping. Two tests are performed with the narrow strip - covering only the first 8° of each of those two cases - thus reducing the coverage of the SS zone.

For configuration P60:58°-66°, the amplitude response (Fig. 6.7) shows a much more extended upper branch ($5.5 \leq U^* \leq 14.2$) than that of P60:58°-66° and desynchronization follows at $U^* > 14.2$. But, with 'pushing' providing a threshold amplitude of $1 \bullet D$, the cylinder goes into galloping, i.e., hard galloping (HG2), achieving an amplitude ratio of $A^* \cong 2.3$.

For configuration P60:60°-68°, amplitude trend very closely follows that of P60:58°-66° up to $U^* \cong 8.5$ and thereafter exhibits reduced amplitudes compared to the smooth cylinder (Fig. 6.7). In this case, desynchronization occurs at $U^* \cong 12.8$ and with threshold amplitude ($1 \bullet D$), the cylinder experiences hard galloping (HG2) at $U^* \cong 14.8$ with a much steeper rise of amplitude (than that of P60:58°-66°). For both P60 configurations the cylinder recovers galloping amplitude. It increases from $A^* \cong 0.7$ (16° coverage) to $A^* \cong 2.3$ (8° coverage) since the SS zone coverage is reduced.

For both these configurations, in the reduced velocity range $5.0 \leq U^* \leq 13.0$, oscillation frequency is higher than that of the smooth cylinder (Fig. 6.8). Sharp decline of oscillation frequency is observed at $U^* \cong 14.2$ for P60:58°-66° and at $U^* \cong 14.8$ for P60:60°-68°. At those points hard galloping commences (Fig. 6.7).

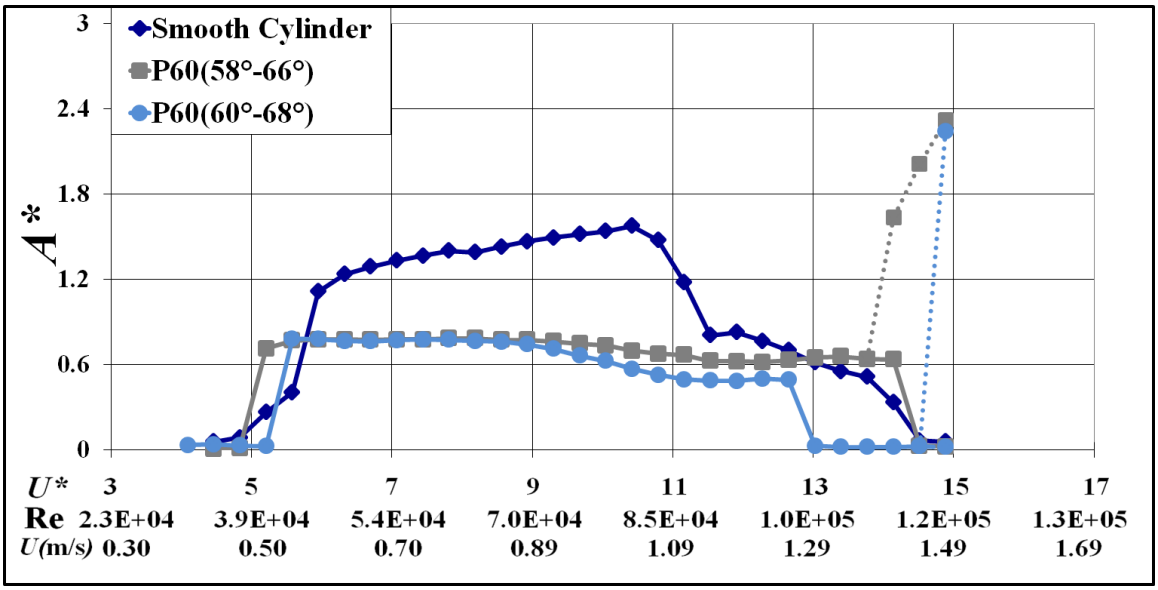

Fig. 6.7. Amplitude response plot for half width with strip P60

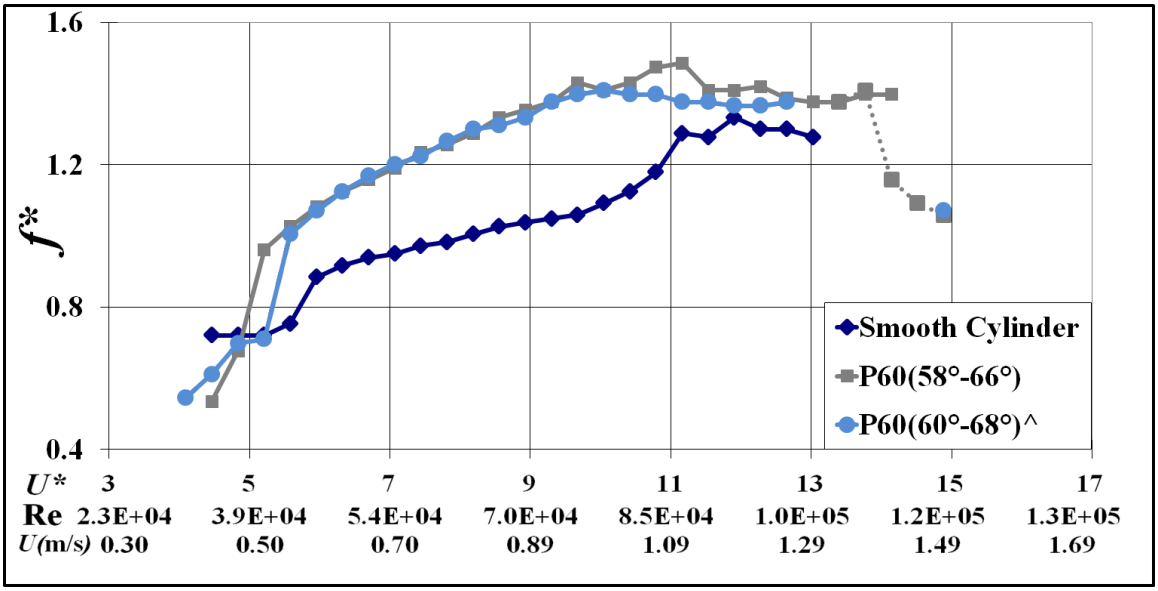

Fig. 6.8. Frequency response plot for half width with strip P60

6.2.2. Wider PTC strips

Two tests with wider strips (1"=2.54cm covering 32°) are performed in this subsection keeping the entire P180 strip inside the SG zone or the SS zone.

Soft galloping was observed for the configuration P180:20°-36° (Fig. 4.2) with steep amplitude increase occurring at $U^*\cong 14.0$. With a wider strip (1"=2.54cm covering 32°) placed at the same strip placement angle (P180:20°-52°), soft galloping starts earlier at $U^*\cong 12.6$ as Fig. 6.9 shows. Correspondingly, the frequency ratio f^* also drops off earlier at $U^*\cong 10.8$ as shown by Fig. 6.10. The maximum amplitude value is nearly the same and the general trend of frequency is very similar in both cases indicating that oscillation frequency is not significantly affected by increased area PTC coverage if the roughness strip is placed in its entirety inside a specified zone.

Strong suppression was identified in Fig. 6.1(a) from $60°\leq\alpha_{PTC}\leq 104°$. Configuration P180:70°-86° induces strong suppression (Fig. 5.8). With increased strip width, a broadened synchronization range with almost the same maximum amplitude is achieved (Fig. 6.9). Frequency registers a continuous increase for $U^*>9.0$ and reaches a value of about 2.3 at $U^*\cong 15.0$ (Fig. 6.10) where oscillations are not steady.

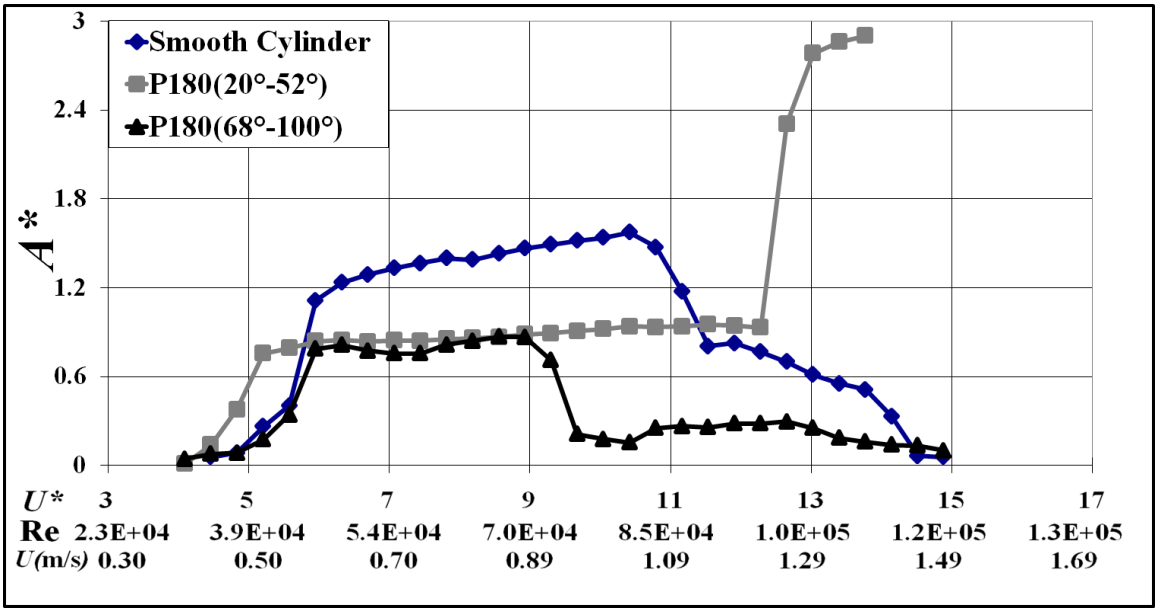

Fig. 6.9. Amplitude response plot for double width with strip P180

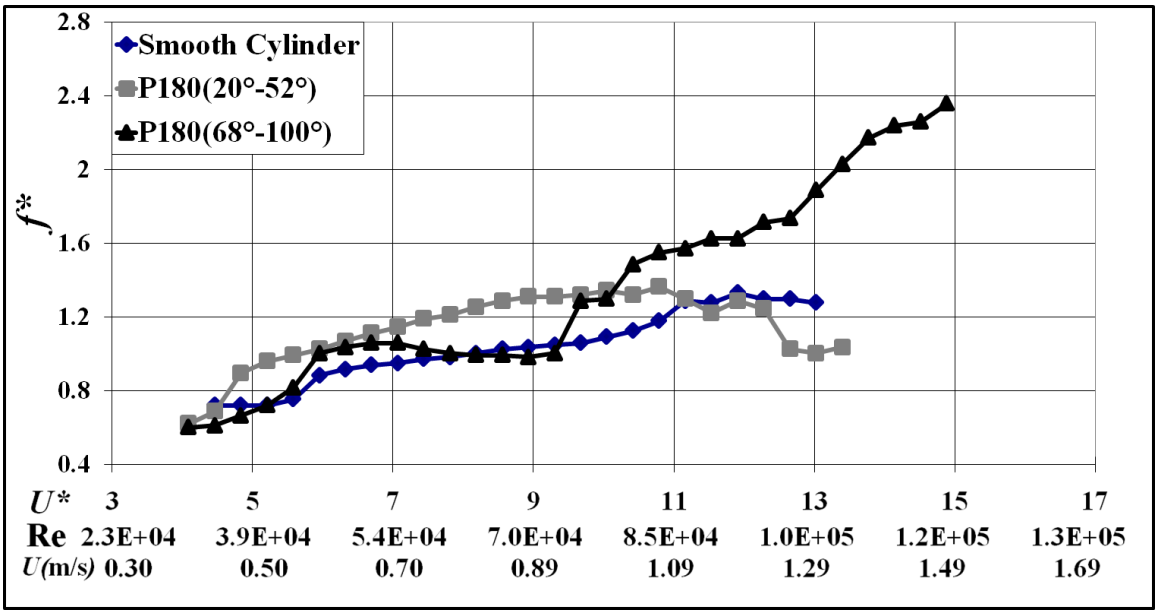

Fig. 6.10. Frequency response plot for double width with strip P180

6.2.3. Staggered PTC Configuration

All tests presented so far were conducted applying straight roughness strips running along the entire span of the cylinder. A 'staggered' roughness configuration is introduced (Fig. 6.11) in the SG zone with P60 strips distributed within the zone range of 10°-56° shown in Fig. 6.1(b). This type of configuration breaks the cylinder surface uniformity and may affect the correlation length along the cylinder span. The cylinder goes into galloping at $U^*\cong 12.3$ (Fig. 6.11); earlier when compared to the case P60:10°-26° (Fig. 4.10) but with the peak amplitude nearly the same. Fig. 6.11 further shows that the correlation length is not a significant factor in deciding the onset and development of soft galloping. Sharp decline of oscillation frequency is observed in Fig. 6.12 at $U^*\cong 12.3$. Similarly to the previous galloping cases, cylinder oscillations are faster in the VIV synchronization range ($5.0\leq U^*\leq 10.8$) compared to smooth cylinder but become slower thereafter.

A similar staggered roughness configuration was exercised with the P60 strip in the range 70°-116° (SS). Substantially reduced amplitude of oscillation is observed as Fig. 6.11 shows. The second amplitude crest noticed with P60:70°-86° (Fig. 5.10) is absent here. The peak response of maximum amplitude ($A^*\cong 0.65$) is limited only to a reduced velocity range $6.0\leq U^*\leq 7.0$. In this case as seen in Fig. 35, oscillation frequency f^* continuously increases with reduced velocity reaching a high value of about 2.2 at $U^*\cong 15$. These results with staggered configuration indicate that the response is predominantly zone-dependent.

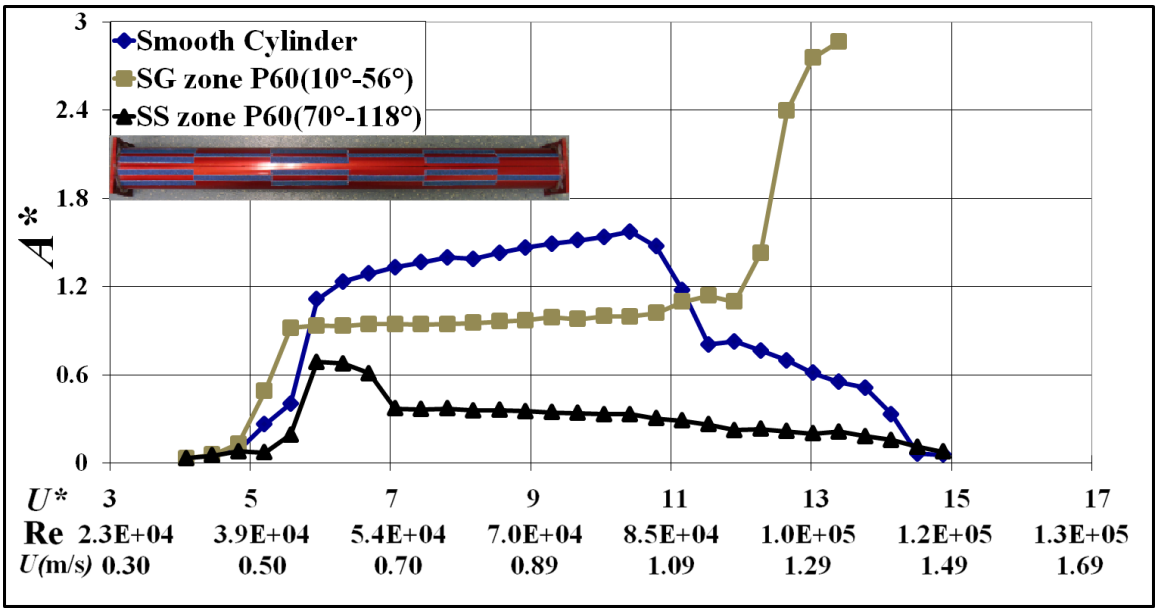

Fig. 6.11. Amplitude response plot for zigzag pattern with strip P180

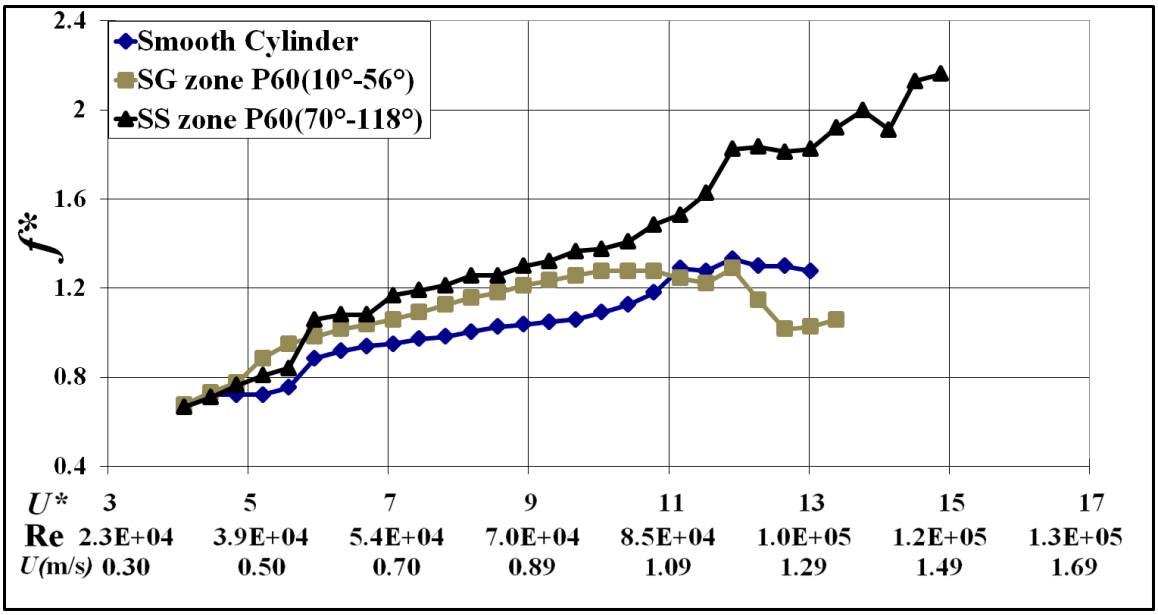

Fig. 6.12. Frequency response plot for zigzag pattern with strip P180

6.2.4. Covering WS1 and HG1

Finally an additional experiment was conducted with straight roughness strips covering two zones. Fig. 6.13 shows the results for P180:0°-12°, where the roughness strip covers both the WS1 zone ($0° \leq \alpha_{PTC} < 2°$) as well as the HG1 zone ($2° \leq \alpha_{PTC} \leq 14°$). The amplitude response trend is similar to that for WS1 (Fig. 5.2) up to a reduced velocity of 14.1 and exhibits hard galloping at $U^* \cong 14.5$. Hence, a combined response is observed in this case. However, in the case of P180:0°-8° in Fig. 4, for $U^* > 11.25$, some times amplitude exceeds that of the smooth cylinder whereas in the case P180:0°-12° only negligible deviations with respect to the smooth cylinder are observed for the oscillatory amplitudes for $U^* > 11.25$. As noted in previous galloping cases, the oscillation frequency has big drop at $U^* \cong 14.5$ (Fig. 6.14).

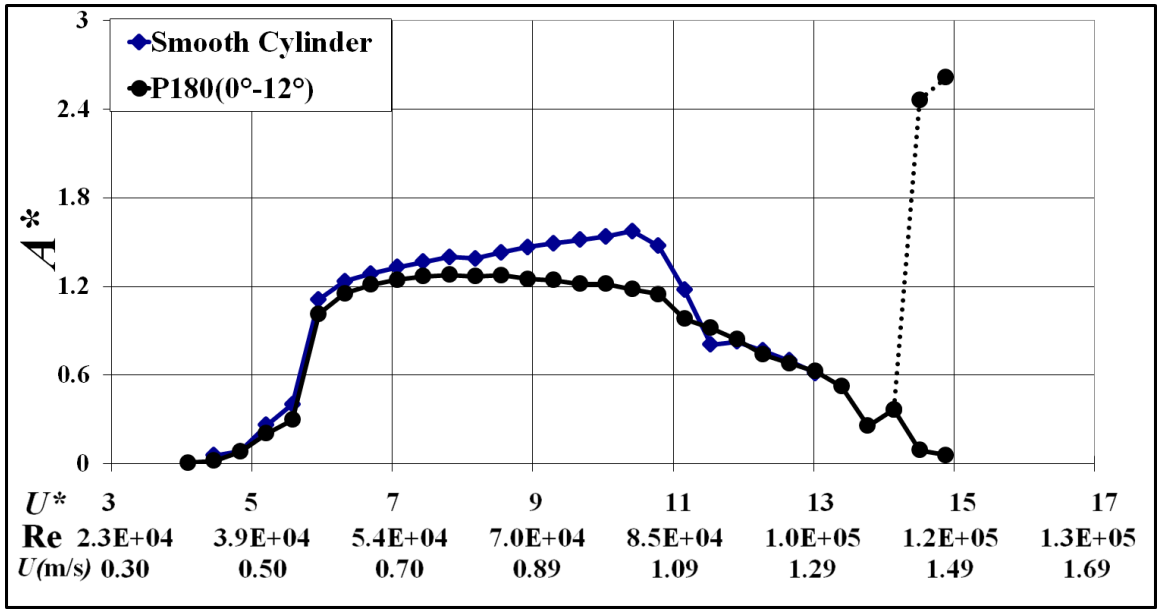

Fig. 6.13. Amplitude response plot for covering two zones (WS1 and HG1)

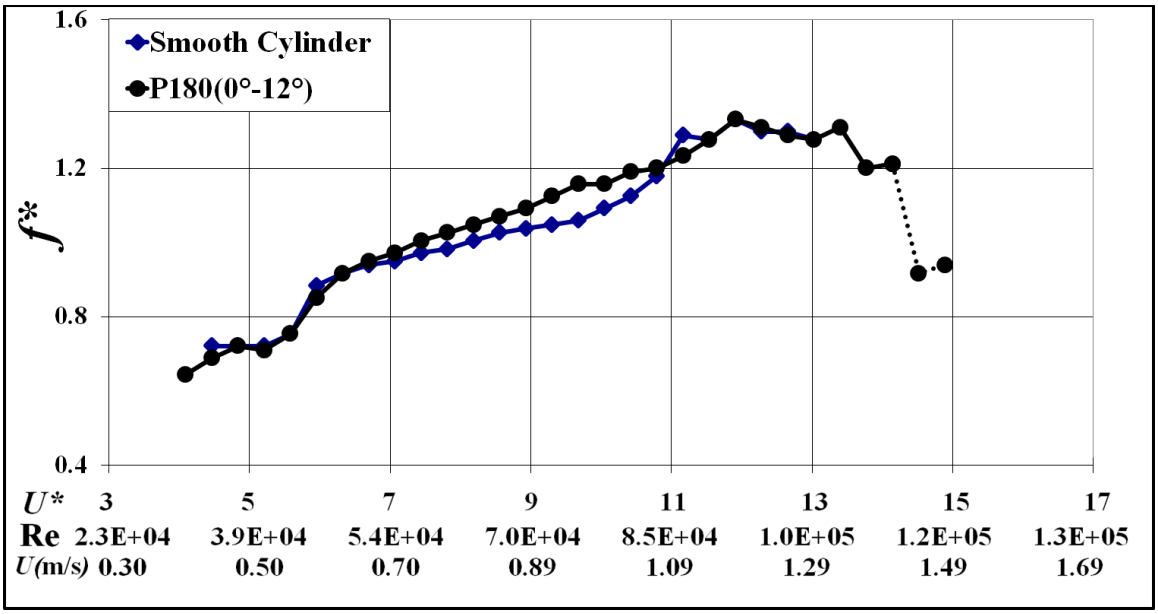

Fig. 6.14. Frequency response plot for covering two zones (WS1 and HG1)

6.3. MAIN FINDINGS

From the results presented in Chapter 6 we can draw the following conclusions:

(i) Even though the overall response classification in the Map is similar for P180 and P60 roughness strips, the surface roughness *k/D* has a small effect on the zonal ranges of HG1, SG, HG2, and SS but does not change the order of zone appearing in the *PTC-to-FIM Map*.

(ii) The SG, SS, and WS2 zones of the *PTC-to-FIM Map* are in agreement with the observations by Nebres & Batill (1993) regarding the location of perturbation (θ_p) used in their study on stationary cylinders. Specifically: (a) For $30°<\theta_p<45°$, the lift force on the cylinder is maximum which agrees with the SG zone of the Map. (b) For $60°<\theta_p<105°$, lift is negative corroborating the SS zone of the Map. (c) For $105°<\theta_p<120°$, lift is slightly positive which agrees with the WS zone of the Map.

(iii) As the *PTC-to-FIM Map* shows, straight roughness strips can act as an FIM amplifier or an FIM suppressor satisfying the intended goals of the present research. Roughness strip acts as an FIM amplifier in the HG1, SG, HG2 zones for a circumferential coverage area of about 58° for P180 and 60° for P60 at U^*>13.0 and as an FIM suppressor in the case of SS for a coverage area of about 46° for P180 and 44° for P60 over a broad range of U^*.

(iv) In light of the data available on the performance of other suppression devices (Kumar et al. 2008; Zdravkovich 1981), roughness strips have the following advantages as a suppression means: (a) are very light in weight, (b) are easy to apply and handle, (c) induce less drag owing to minimal surface protrusion. On the other hand, effectiveness of straight roughness strips is limited by the direction of the incident flow. This issue was studied by Park et al. (2011).

(v) From narrower (8° coverage), wider (32° coverage), and staggered strip tests, if PTC is located inside a specific zone, the amplitude and frequency response is similar to 16° coverage and same FIM is observed as specified in the PTC-to-FIM map in Fig. 6.1. The zones are robust (insensitive) to width and configuration of PTC.

(vi) The PTC influence on FIM changes when multiple zones are covered. When the SS zone is included in multi-zone coverage the strong suppression effect is dominant and the amplitude is reduced by 70% in hard galloping or soft galloping. Thus, if PTC is needed near a zone boundary, it is recommended that further tests be conducted with reduced PTC coverage.

CHAPTER 7

PTC SYSTEM DESIGN FOR SUPPRESSION OF SINGLE CYLINDER FIM

7.1. INTRODUCTION

In this thesis, the developed "***Map of PTC-to-FIM***" is used to guide development of FIM suppression devices that hardly affect cylinder geometry. The map is dependent on flow direction. Thus, the challenge in this work is to design PTC to achieve the desired objective of flow suppression regardless of flow direction. In this quest to design a cheaper, light-weight, yet efficient suppression device, we have put to test commercially available straight roughness strips with certain width and configuration in the present investigation.

From Chapter 6, the "***Map of PTC-to-FIM***" is introduced and a staggered configuration is tested to investigate whether a different configuration can affect or break the relation between any FIM zone and roughness location. The effort with staggered configuration inspires ideas of what is the effect of inclined configuration on the map of PTC-to-FIM, and how to design suppression devices using selective roughness.

The problem to be solved in this chapter is defined as follows:

(1) What is the effect of inclined roughness? Three-dimensional flow hinders vortex shedding and weakens VIV. Thus, inducing three-dimensionality to the flow is a good method to suppress VIV. If inclined roughness was attached in a galloping zone, can the inclined roughness create enough three-dimensionality of the flow over the whole length of the cylinder to break the "rules" set by the "***Map of PTC-to-FIM***"?

(2) Develop a PTC design to suppress or considerably diminish the amplitude of oscillation and range of synchronization of a cylinder in FIM by introducing surface roughness selectively in the boundary layer.

(3) Can roughness be used as an omni-directional suppression device? The results of the roughness model (T6) which uses roughness wrapped helically around a cylinder are presented in Section 7.2.

To answer those questions, Several PTC designs are tested to understand the effect of PTC roughness, location, coverage, and configuration. The PTC-to-FIM map developed in Chapter 6 is used as guidance and surface roughness is placed mainly in the SS zone.

7.2. RESULTS, OBSERVATIONS, AND DISCUSSION

The results of T7 (inclined roughness) are discussed in Section 7.2.1. The effects of roughness, location, and strip orientation in the SS zone are studied in Sections 7.2.2, 7.2.3, and 7.2.4, respectively. In here, the strip angle location is marked differently from previous Chapters. For example, as shown in Fig. 7.1, for the P180:80°-96° configuration T7, at one end of the strip, the strip center is placed at 80° from the forward stagnation point and the center of the other end of the strip is placed at 96°.

7.2.1. Revisit of the *Map of FIM-to-PTC*

In the introduction of the map of PTC-to-FIM in Chapter 6, straight roughness strips with a half-inch width and same length of the cylinder span are used in a symmetric pattern. It is found that the various FIM are dependent on roughness locations, which can be classified as zones. In here, six roughness strips of P180 with half-inch width and 12″ length are attached on the cylinder surface in a symmetric pattern. The roughness covers only 16° of the cylinder surface.

As shown in Fig. 7.1, the results of T7 (inclined staggered roughness) show similar trend to the map of PTC-to-FIM. Even though strip configuration is changed, HG1, SG, HG2, SS, and near WS zones are observed and the strip locations of the zones are almost identical to the map of PTC-to-FIM. Inclined roughness configuration is not able to produce enough three-dimensional flow to alter the map of PTC-to-FIM. Therefore, roughness location is a more effective factor than roughness configuration and determines the FIM type. This Chapter 7 emphasizes suppression methods using roughness. Hard galloping and soft galloping were studied in Chapter 4, thus, galloping caused by T7 is not dealt in this chapter. More information about hard galloping and soft galloping was already discussed in Chapters 4 and 5.

For T7:2°-34° and T7:48°-80° configurations, amplitude response exhibits HG1 and HG2 behavior, respectively. As discussed in Chapter 4, both HG1 and HG2 have distinctive characteristics. Between $6<U^*<12$, HG1 has higher amplitude than HG2. Even though the two configurations need threshold amplitude of about $1 \bullet D$ to initiate

galloping, T7:2°-34° configuration keeps small oscillation amplitude and T7:48°-80° configuration is almost stationary before galloping. After galloping is initiated, the HG1 amplitude line is steeper than that of HG2. When a center of leading edge of the roughness is placed between 20°-50°, the roughness cylinders have soft galloping response and soft galloping doesn't need the threshold amplitude to trigger galloping as opposed to hard galloping. The amplitude is almost constant in the VIV region ($6<U^*<11$) and increases slowly in the VIV-galloping transition region ($11<U^*<13$). After $U^*>13$, amplitude increases very steeply and the cylinder motion becomes fully galloping with $A^* \cong 2.6$ at $U^* \cong 14.5$.

When the center of the leading edge of the roughness is placed between 60°-90°, the roughness cylinder response is suppressed. Depending on the roughness location, the maximum amplitude of the roughness cylinder is reduced up to 56% compared that of the smooth cylinder. For the T7:62°-94° configuration, a short region of bump with $A^* \cong 0.7$ is observed near $U^* \cong 6$. As reduced velocity increases, this bump disappears and an extended flat branch with small oscillation amplitude appears. In the present study, this bump followed by a flat branch are considered as upper branch and lower branch, respectively. The wake vortex structures for these two branches were 2S and 2P as discussed in Section 5.2.5. For all suppression types in Fig. 7.1, commencement of VIV shifts to higher reduced velocity than that of the smooth cylinder. This result is consistent with Kiu et al. (2011) who used roughness rapping around the whole cylinder. It should be noted that for some configurations, mostly in the SS zone, hysteresis is also observed from the initial branch to upper branch and the synchronization region starts earlier if threshold amplitude is given in the initial branch. From this fact, Kiu et al. (2011) may

have hysteresis if they tested with backward speed. The hysteresis result of T7 is almost identical to straight roughness cases in Chapter 5 and is not dealt furthermore.

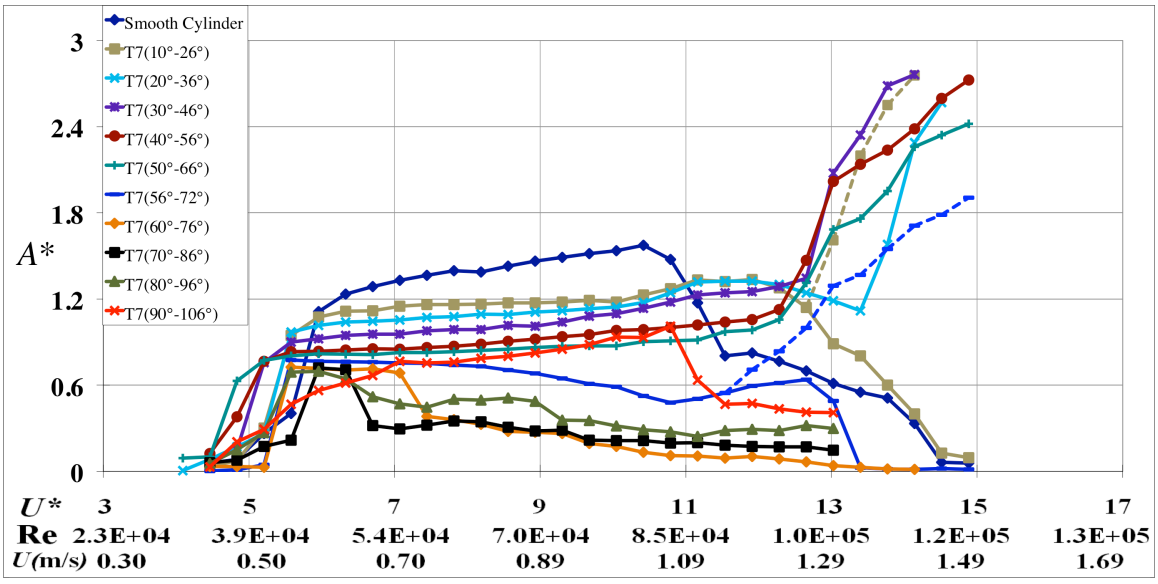

Fig. 7.1. Amplitude response depending on roughness location for T7 configurations

Fig. 7.2 shows the frequency response of the T7 rough cylinders. All the rough cylinders except for the T7:82°-114° configuration have generally higher frequency ratio than that of the smooth cylinder in the whole region of reduced velocity. For the T7:2°-34° and the T7:48°-80° configurations, the frequency ratio is higher than that of the smooth cylinder and keeps increasing until a dominant frequency disappears. At $U^* \cong 13$, where the cylinder exhibits minute amplitude or is stationary, dominant frequencies are not found. When a one-diameter threshold amplitude is given, the dominant frequency reappears and the frequency ratio approaches unity. When the center of the leading edge of the roughness is located between 20°-50°, the frequency response is almost similar to that of HG with threshold amplitude. In the VIV region ($4<U^*<11$), the frequency ratio is

higher than that of the smooth cylinder and keeps increasing and this feature is more distinctive for higher strip angle locations. The frequency ratio starts decreasing in the VIV-galloping transition region and reaches unity at galloping.

When roughness is placed at T7:52°-104°, the frequency response is higher compared to that of the smooth cylinder in the whole synchronization region. After U^*>11, the roughness cylinder oscillation is either very small or negligible so that the corresponding frequency ratio disappears. Only the T7:82°-114° configuration has roughly lower frequency ratio than that of the smooth cylinder. As already shown in Fig. 7.1, the T7:82°-114° configuration has broad synchronization like the smooth cylinder and it is considered as not being in the SS zone.

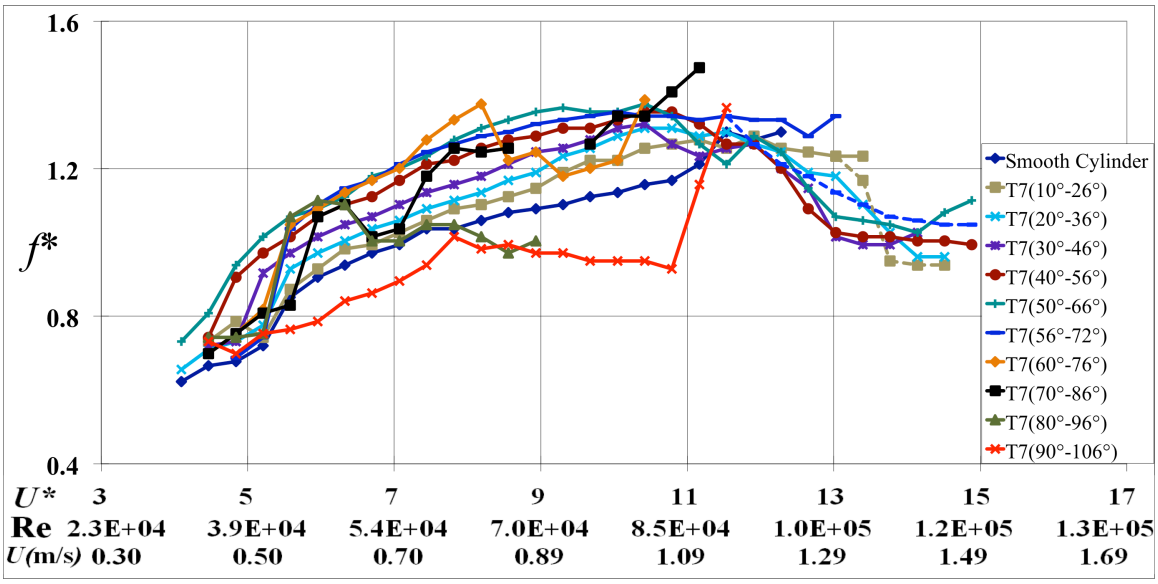

Fig. 7.2. Frequency ratio depending on roughness location for T7 configurations

From the T7 configurations tests, the zones defined in the ***map of PTC-to-FIM*** is very robust and changing roughness configurations doesn't affect in general much the

properties of the ***map of PTC-to-FIM***. Therefore, the map of PTC-to-FIM would give clues to cylinder suppression studies and the application would be very robust.

7.2.2. Effect of roughness

Fig. 7.3 shows the results for PTC configuration T7 with strips of half-width in all cases studied. All cases shown in Fig. 7.3 are for strip location T7:60°-76°. In all the cases of PTC tested, oscillation amplitudes have been significantly reduced with a maximum peak A^* value of about 0.8, which is about 50% of that of the smooth cylinder. It should be noted that in our line of experiments, A^* reaches values of 1.6 for smooth cylinders and exceeds 3 for PTC cylinders for two reasons (Raghavan & Bernitsas, 2010, Chang et al. 2010): (a) the flow regime where our tests are conducted is the TrSL3 high-lift regime (Zdravkovich 1997) and (b) with PTC in the galloping zone of the PTC-to-FIM map, galloping is induced (Park et al. 2012).

Though all the PTC configurations are found to be successful in partially suppressing cylinder FIM, it is observed that the rougher the strip the higher is the maximum amplitude response but with slightly shorter synchronization range (Fig. 7.3). This is the general trend for lower reduced velocities, ($U^*<7.5$).

For higher U^* values ($U^*>7.5$), this trend is reversed with higher oscillations occurring for smoother strips. Further, for $U^*>11.0$, roughness significantly suppresses the oscillations to negligible values irrespective of the roughness value. The test with smooth strips ($k=0,\ (k+H)\neq 0$) yielded results somewhat similar to that of the smooth cylinder but with early desynchronization and lower maximum amplitude (Fig. 7.3).